Fall 2009

Real-time and portable microwave imaging system

Mohammad Tayeb Ahmad Ghasr
Missouri University of Science and Technology, mtg7w6@mst.edu

Department: Electrical and Computer Engineering

Recommended Citation

Ghasr, Mohammad Tayeb Ahmad, "Real-time and portable microwave imaging system" (2009). *Doctoral Dissertations*. 2247.
https://scholarsmine.mst.edu/doctoral_dissertations/2247

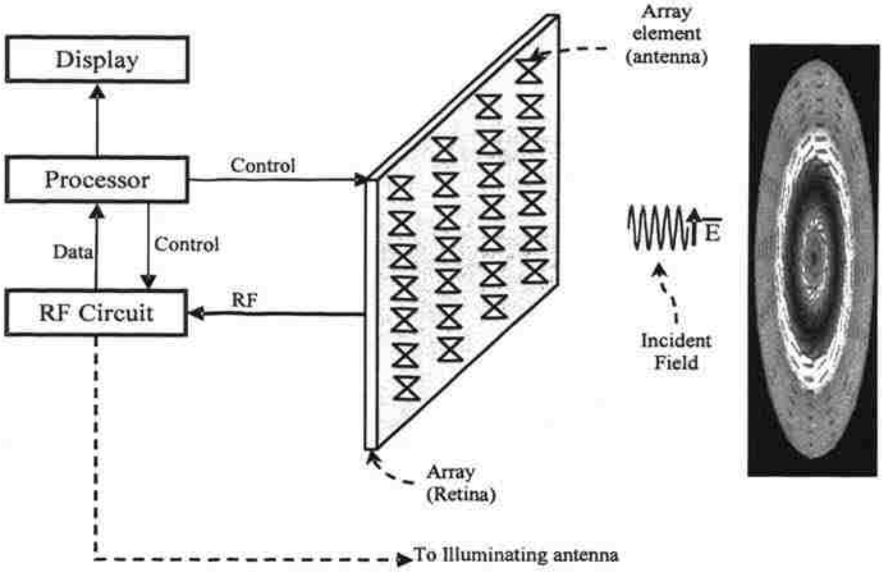

Figure 2.1. General schematic of a 2D electric field mapping device (microwave camera).

The retina samples the scattered electric field distribution at the location of each antenna element. Thus, the spacing between individual antennas must be properly chosen so that the measured discrete electric field distribution is a close representative of the continuous electric field distribution on the retina. Consequently, Nyquist Sampling Theorem [39] dictates that the array element center-to-center interspacing not be larger than $\lambda/2$ (λ is the operating wavelength). Any larger interspacing results in errors associated with the reconstructed scattered electric field distribution. This interspacing requirement also affects the type (i.e., size) of antenna that may be used to construct the retina, as will be discussed later.

Finally, the imaging system must be capable of distinguishing electric field information for each antenna. One approach to accomplish this is to spatially "tag" or "multiplex" the scattered electric field. One attractive approach for doing so is based on modulated scatterer technique (MST). MST has been developed and used mainly for antenna pattern mapping applications. Direct measurement of the electric field requires connecting a small probing antenna through transmission lines (e.g. coaxial line) to the

one-to-one correlation between reduction in modulation efficiency of the scatterer and the degradation of the overall system performance in estimating the amplitude and phase of the signal. For example using a λ/2 dipole with a modulation depth of approximately 15%, reduces the useful dynamic range of the system by as much as 20 dB. Furthermore, when used in a 2D array, the λ/2 dipole does not fit the center-to-center spacing of λ/2, and the λ/4 dipoles which are commonly used in a 2D array presents a much smaller modulation efficiency, which further reduces the useful dynamic range of the system. The small dynamic range may be acceptable in some applications, such as antenna pattern measurement, where the user can compensate for lower dynamic range by increasing the radiated power. However, in imaging applications the scattered field most likely will present a relatively large variation in power over the retina domain [42]. Furthermore, targets of interest are usually weak scatterers (i.e., small, embedded in a dielectric host, etc.) and their associated power scattered power level will be near the noise floor of the system.

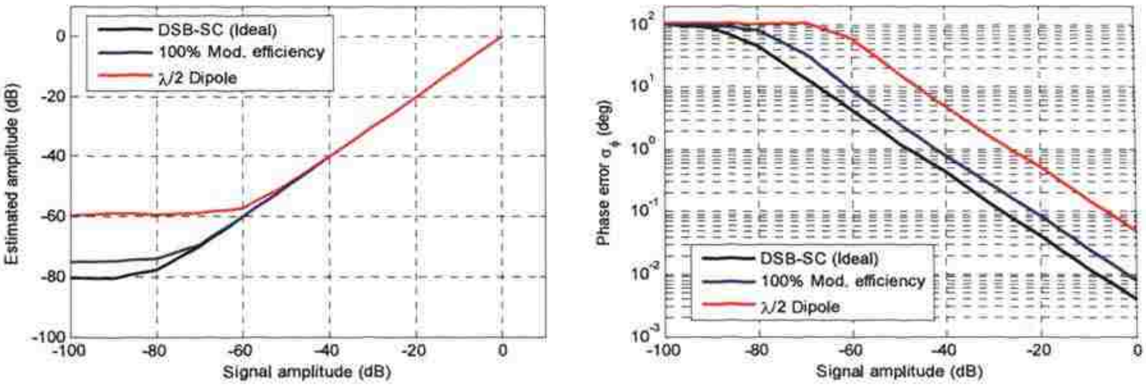

(a) (b)

Figure 2.4. Simulated system performance for various modulation efficiencies: (a) dynamic range, and (b) phase error.

Overall, the modulation depth of the scattering probe will greatly influence the performance of systems whose designs are founded on utilizing MST for measuring

shown in Figure 2.5. This is an elliptically-shaped resonant slot loaded with a circular patch. Due to the elliptical shape, the slot becomes linearly polarized with the electric field being concentrated between the circular load and the surrounding conductor on top and bottom [38]. By shifting the circular load from the center of the elliptical slot to near its lower edge, the concentration of the electric field increases in that gap between the circular load and the elliptical slot, which becomes an ideal location for placing a switching PIN diode. When the PIN diode is turned OFF (reverse biased), the slot is open and passes the signal through it efficiently. Conversely, when the PIN diode is turned ON (forward biased), the slot is closed and almost no signal passes through it. These properties allow the slot to provide near 100% modulation depth when used in a transmission-through configuration. It has also been shown that the mutual coupling between two such slots is low compared to dipoles used for the same purpose [43]. Moreover, the presence of a ground plane allows for reducing the effect of the dielectric substrate and bias structure by properly shielding them from interacting with the electromagnetic field.

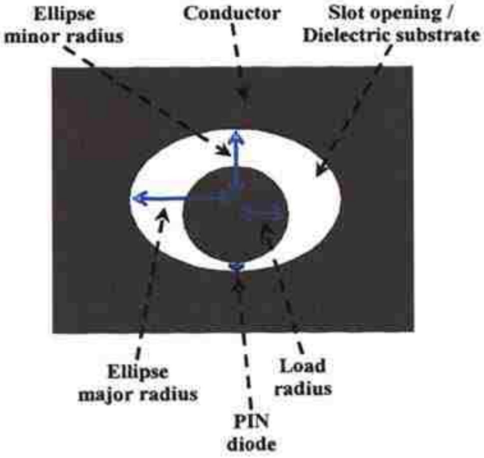

Figure 2.5. Schematic of the PIN diode loaded resonant elliptical slot.

There is one major difference between the slot antenna and the dipole in the way they are used, which limits the utility of the slot for general MST use. The slot is typically used in through transmission (i.e., the signal is passes through it) while the dipole is used in scattering mode. Furthermore, the slot is surrounded by a conducting sheet, which makes reflective when it is closed. These two properties of the slot, makes it unsuitable for mapping of near-field distributions for example mapping of antenna aperture electric field distribution.

This slot behaves as a resonant antenna and hence possesses a resonant frequency response. The resonant frequency, which is intended to coincide with the operating frequency of the imaging system, is dictated by the dimensions of the slot, the electrical properties of the dielectric substrate, and the capacitance of the PIN diode in the OFF state. The resonant frequency is determined through a 3D electromagnetic simulation of the overall slot structure. Figure 2.6 shows the simulated (using CST-MWS [44]) return-loss, looking into the elliptical resonant slot mounted on the aperture of a K-band (18-26.5 GHz) waveguide. In the simulation tool, the slot was built on a 0.5 mm thick Rogers4350 [45] dielectric substrate. The ellipse had a major radius of 2 mm and an axial

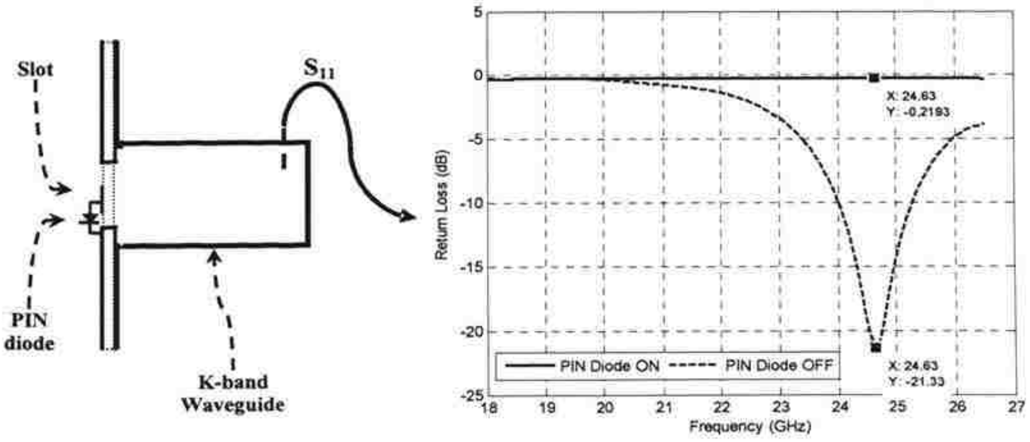

Figure 2.6. Simulated return-loss of the elliptical resonant slot.

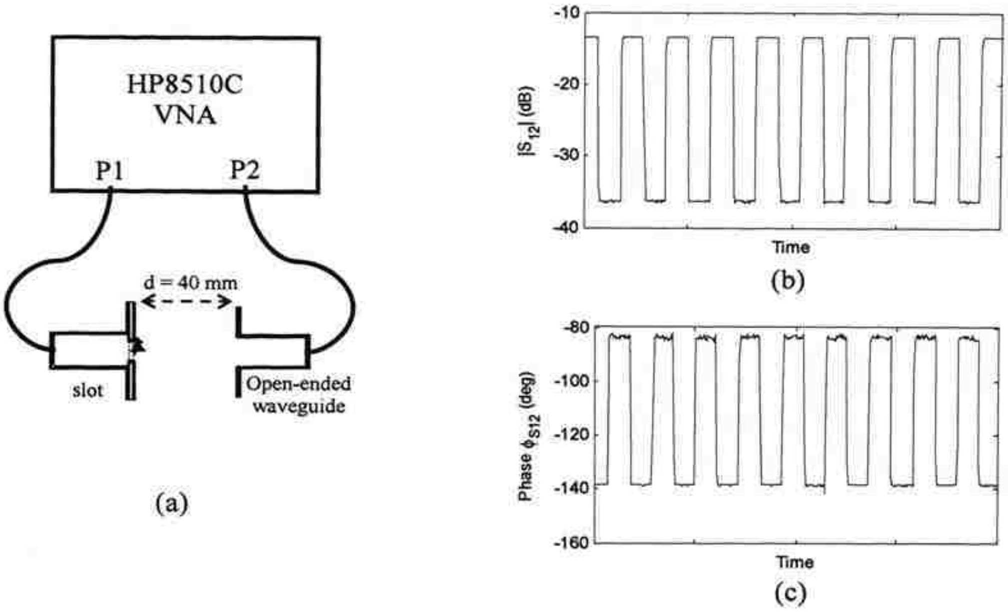

(a)

(b)

(c)

Figure 2.7. Modulated transmission-through (S_{12}) response of a resonant elliptical slot at 24 GHz; (a) measurement setup, (b) Magnitude, and (c) phase

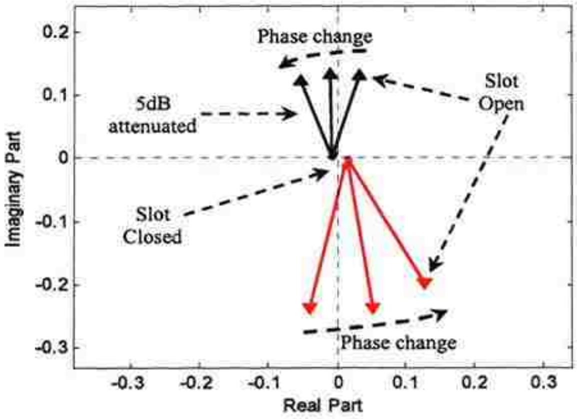

Figure 2.8. Vector space representation of the modulated signal.

Figure 2.9 shows a comparison between the modulation depth of a resonant $\lambda/2$ dipole and the resonant elliptical slot both designed to operate at 24 GHz. Both antennas were used in a through transmission mode. For these measurements the slot was placed on the aperture of a K-band waveguide. The dipole was placed on the aperture of a small horn antenna connected to a K-band waveguide. Dipoles are not typically used directly on a horn or waveguide aperture. However, by placing the dipole on the horn aperture it is given similar advantage that the slot possesses, consequently larger modulation depth is obtained by collecting a larger portion of the scattered field.

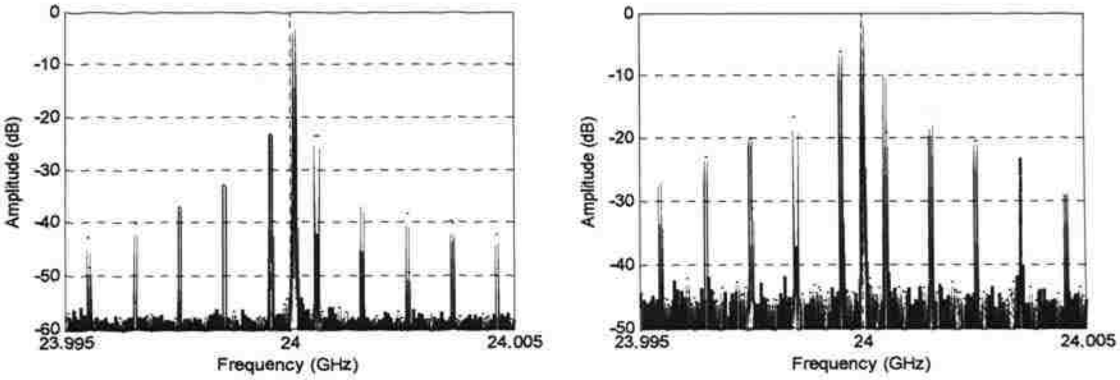

(a) (b)

Figure 2.9. Measured Modulated spectrum (f_m = 500 KHz): (a) $\lambda/2$ dipole, and (b) resonant elliptical slot.

The spectra show the carrier at 24 GHz and a double side band square wave amplitude modulation with a fundamental frequency of 500 KHz. The $\lambda/2$ dipole (Figure 2.9a), generated a modulated signal of 23 dB below carrier, which corresponds to approximately 12% modulation efficiency. On the other hand the resonant elliptical slot (Figure 2.9b) generated a modulated signal of 7 dB below carrier corresponding to approximately 77% modulation depth.

2.4. ANTENNA PATTERN MAPPING

The following experiment demonstrates the capability of the resonant elliptical slot for electric field distribution measurement. In this experiment, a probing antenna is used to measure the radiated electric field magnitude and phase of an antenna under test (AUT) as a function of distance from that antenna. This experiment demonstrates the advantages of a matched probing antenna as well as the effect of modulating it. The experimental setup is shown in Figure 2.10 where each of three probing antennas is scanned perpendicular to the aperture of the AUT with a step size of λ/4. The AUT was a K-band open-ended rectangular waveguide operating at 24 GHz.

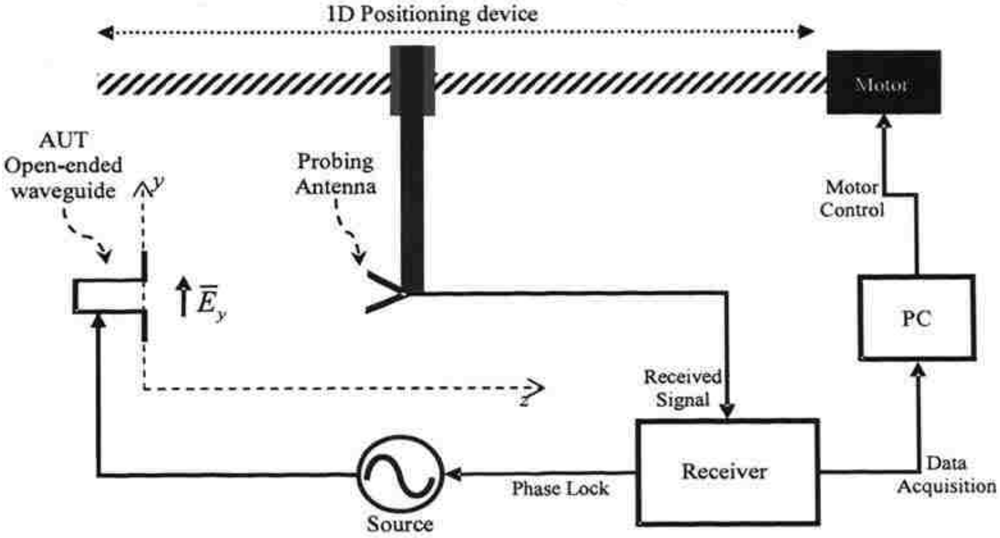

Figure 2.10. Setup for measuring 1D electric field magnitude and phase variation vs. distance.

The probing antennas were a non-modulated open-ended rectangular waveguide (OEWG), a modulated λ/2 dipole mounted on a small horn, and a modulated resonant elliptical slot mounted on the aperture of a K-band waveguide. All antennas were

advantage of modulating the probe is apparent. The modulated slot and even the modulated dipole antennas follow the theoretical curve closely. Even though the modulation depth associated with the dipole is not very high, given the large measurement system (i.e., receiver) dynamic range (>80 dB) the effect of this low modulation depth is not sensed. Conversely, the non-modulated OEWG probe measurement shows ripples due to the interaction of the received probe signal with signals coupled directly to the receiver from the source. This issue may be corrected by shielding the receiver, estimating the interference and subtracting it, or by modulating the probe as illustrated in this measurement. The non smooth amplitude ripples and the apparent phase error are due to the large step size associated with these measurements. The magnitude and phase errors compared to theoretical values are better presented in Figure 2.11 (b). The magnitude error in the far field is on the order of 0.001 and the phase error does not exceed 20 degrees everywhere. These errors may as well be due to alignment or positioning errors in the scanner. It must be noted that these measurements are performed at 24 GHz, where 20 degrees of phase error corresponds to less than 0.7 mm of position error.

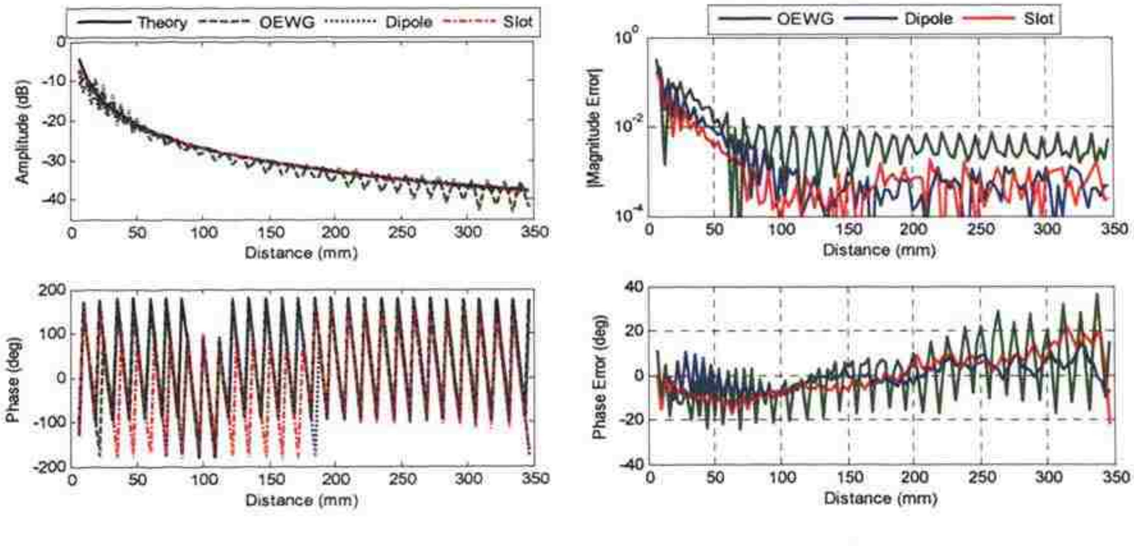

(a) (b)

Figure 2.11. Measured radiated electric field from an open-ended waveguide antenna. (a) Measured amplitude and phase vs. theory, (b) error compared to theoretical values.

2.5. INITIAL 2D IMAGING PROTOTYPE

To investigate the potential of using array of resonant elliptical slots in electric field mapping and imaging applications, a small scale prototype, operating at 24 GHz, was designed and built [37],[47] to demonstrate the proof-of-concept for designing such an imaging system. The design requirements and objectives were as follows:

- Adequate spatial resolution: The design should allow for sampling the electric field at steps of λ/2 or smaller for high resolution imaging.
- High overall system sensitivity and large dynamic range: The overall system dynamic range must be sufficient for capturing large variations in the electric field, yet the system noise floor must be low enough for the system to register signals from weakly scattering objects.
- Real-time operation: The electric field over the retina must be sampled rapidly, approaching video refresh rate.

2.5.1. Design.

The schematic of this prototype is shown in Figure 2.12. Beside

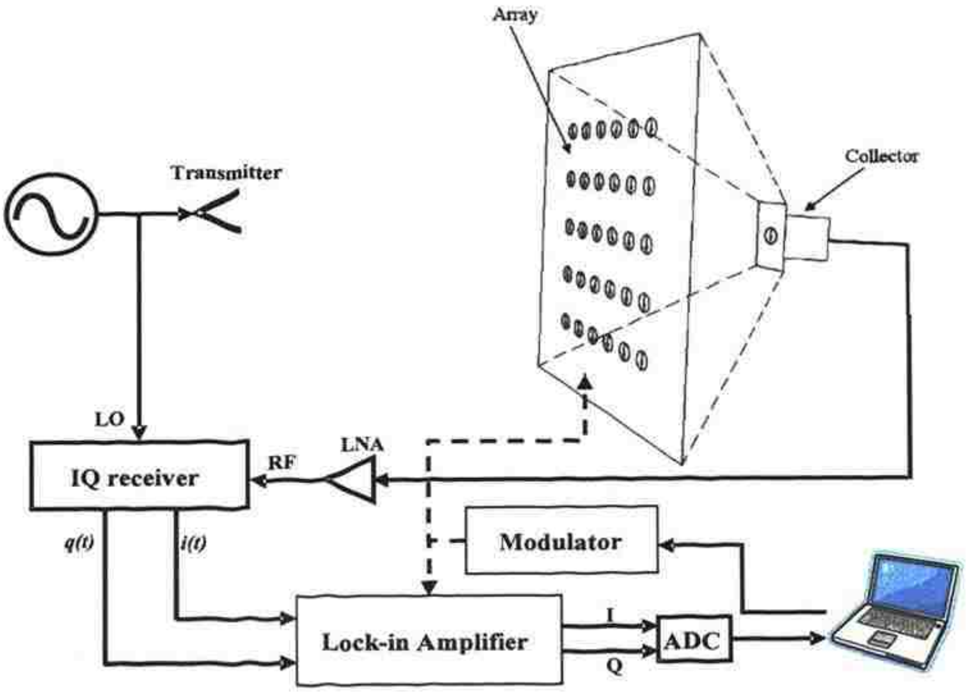

Figure 2.12. Schematic of the initial prototype.

the array elements (slots), many of this design's attributes were similar to traditional MST arrays [34]. The RF receiver was a homodyne direct IQ down-conversion receiver followed by a lock-in amplifier, as explained earlier in Figure 2.3. The signal collection was based on a single antenna spatial collection scheme. A detailed description of the design of this prototype will be explained later.

This system is designed to operate mainly in the transmission mode as illustrated in Figure 2.12 where the retina acts only as a receiver, mapping the electric field incident on its aperture. It is also possible to operate this system in the mono-static reflection mode where the retina transmits the incident field and receives the transmitted/scattered field. In both modes mapping of the electric field is performed sequentially. When each slot in the retina is tagged, it is modulated by opening and closing the slot at a rate of 455 KHz. The detailed design attributes of this prototype may be found in [37],[47], the following subsection will provide a brief description of the components in this prototype.

2.5.1.1 Retina. The retina consisted of a 30-element array (6 rows by 5 columns), as shown in Figure 2.13. This array was manufactured using standard photolithographic techniques on a Rogers4350 [45] substrate. The largest dimension of the elliptical resonant slot was comparable to $\lambda/3$ which allows the array to be implemented with slot center-to-center interspacing of $\lambda/2$ (6.25 mm at 24 GHz). In this design, the DC bias lines, used for modulating the PIN diodes, were RF-coupled to ground at the edge of the

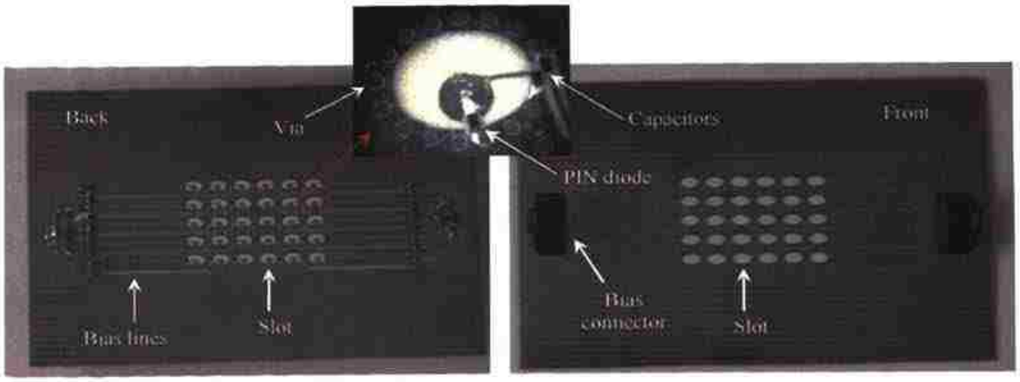

Figure 2.13. Pictures of the front and back of the retina.

dynamic range of approximately 60 dB, as shown in Figure 2.14. The IQ receiver used here was the state of the art in commercial technologies. However, it had a quadratic unbalance of 8° which furthermore affected the linearity in its response. This unbalance understandably has a larger effect on the phase accuracy.

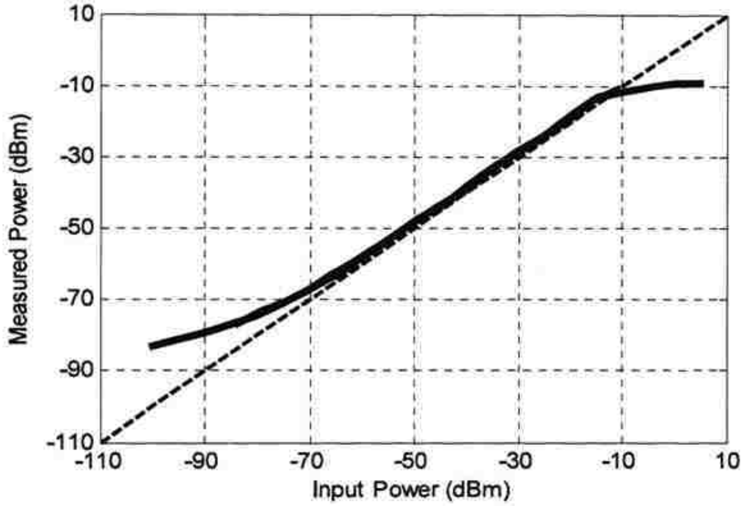

Figure 2.14. Dynamic range of the homodyne receiver.

2.5.2. Results

2.5.2.1 Transmission-through mode. Several experiments were performed to verify the capabilities of this design in mapping electric field distribution. The setup for one of the experiments is shown in Figure 2.15. A small metallic sphere with a diameter of 4 mm was placed at a distance of 12 mm away from the retina. An open-ended K-band rectangular waveguide was used to illuminate the target and retina combination from a distance of 80 mm (far-field of the transmitter). The electric-field distribution without the presence of the target (i.e. metallic sphere) was measured and used as a reference. This setup was also simulated using CST-MWS [44].

Figure 2.16 shows the measured and simulated results for this experiment. Due to the limited number of measurement points on the retina, the measured results were up-sampled by a factor of 6.25 and spatially interpolated resulting in a smoother image with an effective one pixel per millimeter resolution. The images in Figure 2.16 show good agreement between the measured and simulated data both in the shape of the electric field distribution and its associated magnitude and phase values. The distortion shown in the field map is due to the limited resolution of retina. Moreover, a simple linear interpolator was used to resample the images, which may not be optimum.

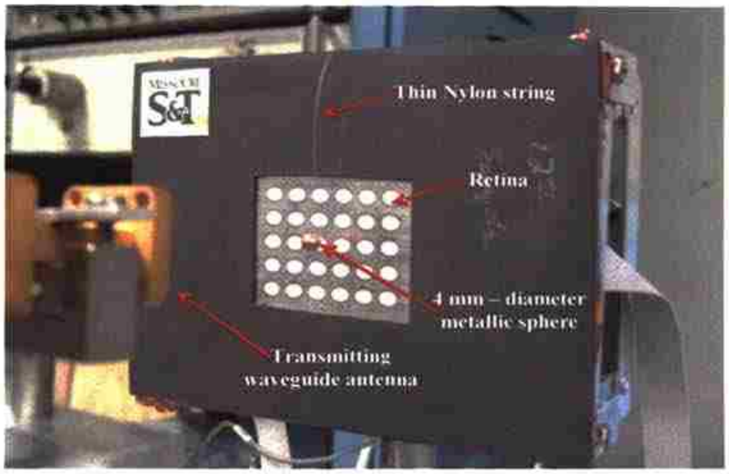

Figure 2.15. Initial prototype transmission through experiment.

2.5.2.2 Reflection mode. In another experiment the system was used in a mono-static reflection mode, where the retina both transmits and receives the signal. In this setup the source signal is fed to the collector of the retina through a directional coupler. The slots in the retina are sequentially tagged to illuminate the target. The reflected signal is then collected and routed to the receiver using the directional coupler. Figure 2.17(a)-(b) shows magnitude and phase of the back-scattered wave when imaging a 10 mm diameter metallic sphere from a distance of 10 mm using the imaging system (i.e., the camera) in its reflection mode. As a comparison, a single slot was used to raster scan the same 10 mm diameter metallic ball using HP8510C vector network analyzer (VNA)

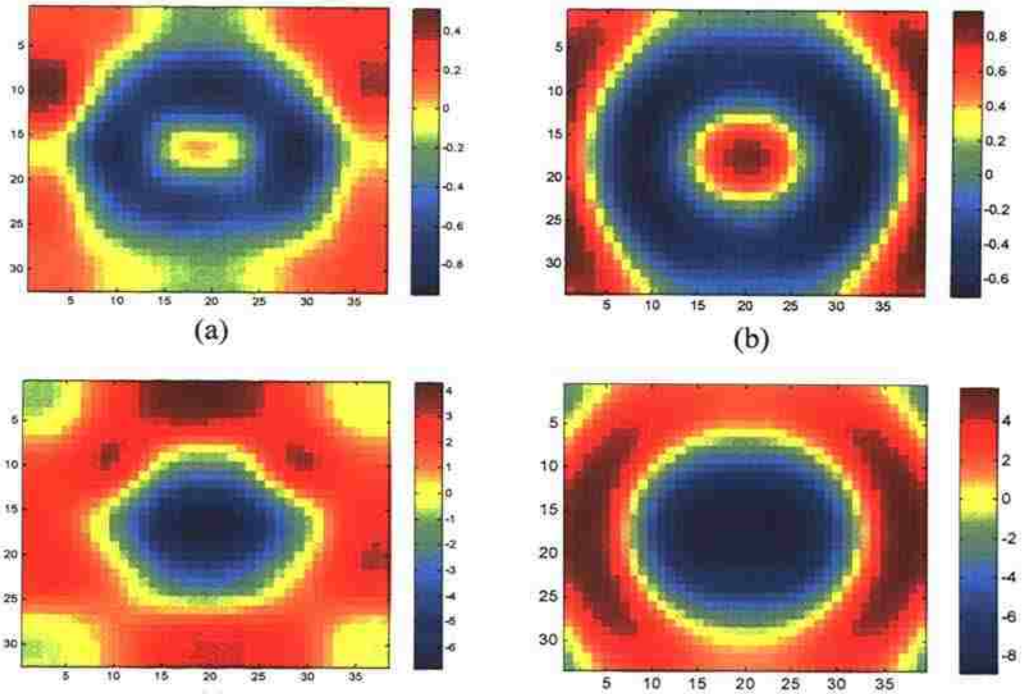

(a) (b)

(c) (d)

Figure 2.16. Measured and simulated field distribution due to the 4 mm diameter metallic sphere placed 12 mm away from the retina; (a) measured magnitude, (b) simulated magnitude, (c) measured phase, and (d) simulated phase.

as a transmitter/receiver, the results of which are shown in Figure 2.17(c)-(d). The images in Figure 2.17 show good agreement between the scanned and camera images both in magnitude and phase. Differences between the camera and scanned results may be seen in the background value of the images. The background in the camera images approximately has a magnitude of 0.9 with an angle of 54°, while the scanned image show a value of 0.85 with an angle of 25°. This difference may be attributed to referencing error in the camera. All of these images were obtained on a grid of $\lambda/2$ spacing and interpolated 6.25 times as explained before. It must be noted that this camera produced images at a video frame rate of 30 images per second, far surpassing any mechanically scanned systems.

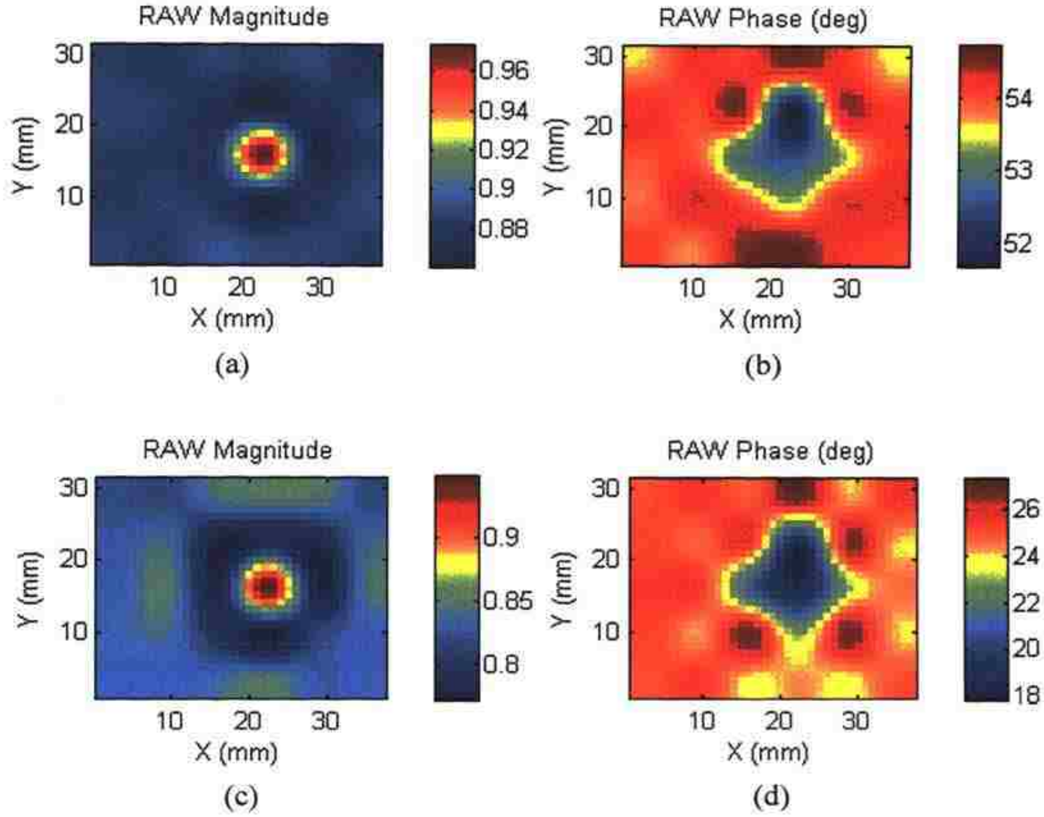

(a) (b) (c) (d)

Figure 2.17. Comparison between imaging using microwave camera and raster scanning for a 10 mm diameter metallic sphere at 10 mm distance; (a) camera magnitude, (b) camera phase, (c) scanned magnitude, and (d) scanned phase.

2.5.3. Limitations and Improvement Considerations. This small scale proof-of-concept camera prototype showed that utilizing the efficient elliptical resonant slot it is possible to measure the coherent electric field distribution. However, this design is not easily expandable to a large scale due to many limitations especially at high microwave frequencies. Improvements must be considered in many aspects of the design to produce a viable imaging system. The sub-systems that must be improved are: the RF transmitter/receiver section, the collection scheme, and the image acquisition rate.

on the front-side of the frame and secured using a rim. On the back-side, the various RF, IF and control circuit boards are mounted.

The design of this imaging system has a compact form factor. Integrating the high frequency transceiver components into the frame of the retina – beside its appealing compactness, eliminates errors caused by long and flexible coaxial transmission lines otherwise required. In basic operation the slots will be closed and sequentially tagged (modulated) to spatially multiplex the incident electric field. The signal picked up at each slot location will split in two halves traveling to each end of the collecting waveguide behind it. The collector waveguides are terminated at each side into combiners which transfer the signal into output ports that are connected to the receivers. Several aspects of this design were optimized through extensive simulations, experimentation, or a combination of simulation and experimentation. The design features and properties of each component of this imaging system are described in details in the following subsections.

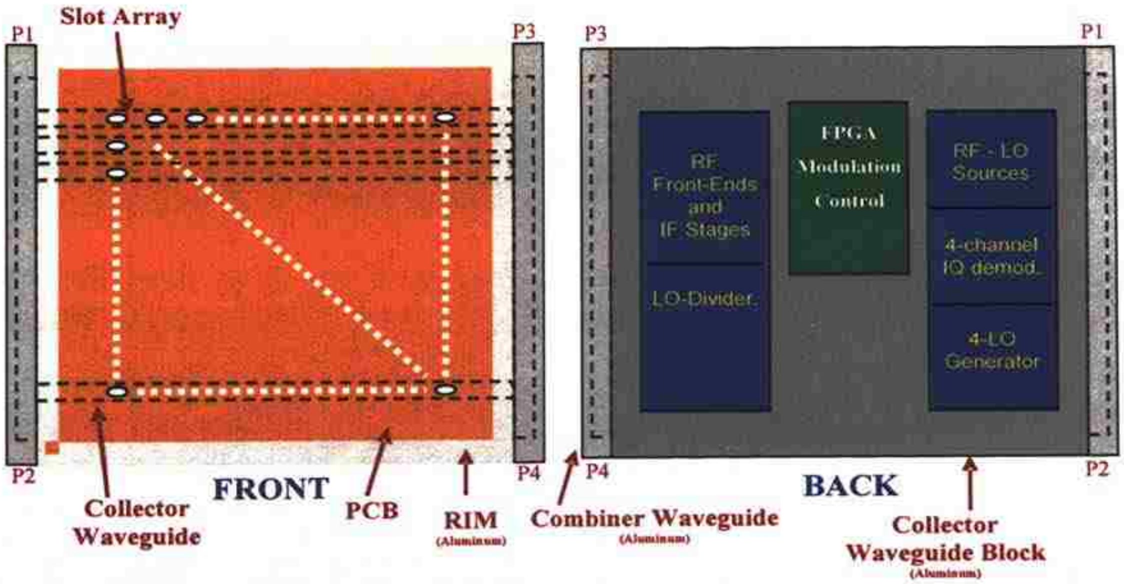

Figure 3.1. Overall imaging system schematic.

3.2. SIGNAL COLLECTION SCHEME

As mentioned earlier, waveguides are preferable to transmission lines at microwave frequencies. Compared to coaxial or printed (e.g. microstrip, CPW) transmission lines, waveguides are virtually lossless. Furthermore, slot antennas may be easily integrated on waveguide walls with the possibility of optimizing the location for a given application. A schematic of rectangular waveguide is shown in Figure 3.2. The waveguide is a hollow metallic tube which has a rectangular aperture with dimensions *a* and *b* ($a > b$) and the dominant mode electric-field is polarized parallel to *b* [48].

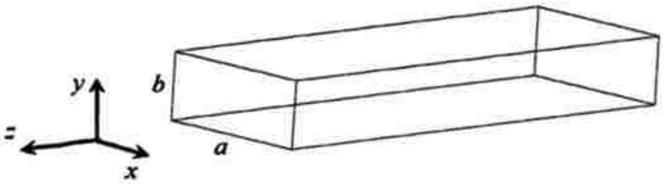

Figure 3.2. Schematic of a rectangular waveguide.

When designing a waveguide based slot array, slots are placed along the side-walls of the waveguide by matching the polarization of the slot antenna to the direction of surface current flow on the waveguide walls. As shown in Figure 3.3, on the broad side-wall currents are along the *z*-direction in the middle of the wall and they curve towards the *x*-direction as they near the edge. On the narrow side-wall the currents are primarily in the *y*-direction [48]. Therefore, a linearly polarized slot antenna (like the one used here) may be placed on any side of the waveguide by matching its polarization to the direction of current flow.

The retina size of ~6″ × 6″ corresponds to an array of 24 rows by 24 columns with an interspacing of 6.25 mm corresponding to $\lambda/2$ at 24 GHz (λ is the free-space wavelength). It was decided that each row of the array will be placed on a separate waveguide, as illustrated in Figure 2.1, since the loss in the waveguide is proportional to

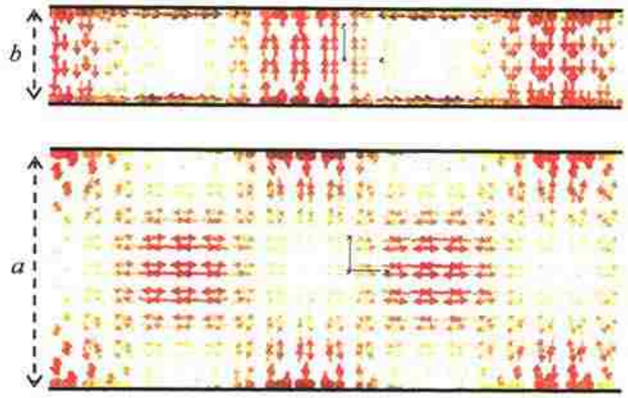

Figure 3.3. Dominant mode (TE_{10}) current distribution on waveguide walls.

the number of slots on its wall. Each PIN diode-loaded slot when closed contributes a small amount of unwanted leakage/radiation loss (0.28 dB per slot) which can add up to a high loss in the waveguide. Another issue to be considered when placing the slots on the waveguide walls has to do with space management given the array elements interspacing requirements ($\lambda/2$) and the variety of options for slot placement on waveguide walls. The broad dimension of the waveguide must be larger than $\lambda/2$ or else the waves will not propagate inside it [48]. Therefore, it is physically impossible to place two waveguides side-by-side with their broad side-walls in one plane and a center-to-center spacing of $\lambda/2$. For these reasons, it was decided that the slots will be placed on the narrow side wall of the waveguide. A standard K-band waveguide has a narrow dimension of 4.3 mm which leaves an adequate 1.95 mm of wall thickness between each two waveguides when placed at 6.25 mm distance from each other. This size is also slightly larger than the height of the slot.

Figure 3.4 shows the aluminum base of the retina including the 24 signal collection waveguides. The waveguides are machined in a single aluminum block. The retina slot array makes the fourth wall of the waveguides. Figure 3.4 also shows a picture of the assembled retina showing the slot array PCB mounted using an aluminum rim on top of the waveguide network. The PCB was connected to the waveguide array using conductive epoxy thus ensuring no signal leakage or coupling between adjacent waveguides. The design of the slot array PCB will be discussed in the upcoming subsections. The rim on top of the PCB serves two purposes. First, it provides for a secure mounting of the slot array PCB onto the base. The second purpose of the rim is to complete the flange on the side of the retina for terminating these waveguides into signal combiners. The design of the combiners will be discussed at later stages of this section. Next subsection will discuss the design of the slot array.

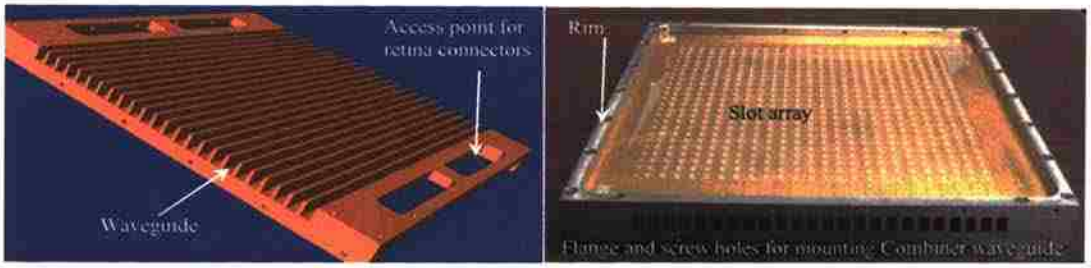

Figure 3.4. Aluminum base of the camera (left), and the assembled retina (right): 24 parallel waveguides serve as a collection network.

3.3. SLOT ARRAY DESIGN

3.3.1. Resonant Slot. As described in detail in the section 2, the resonant PIN diode-loaded elliptical slot of the initial prototype was found to be optimum for this application. This slot provides for very small signal leakage when "closed", and high radiation efficiency when "opened". These attributes make the slot a good candidate for a waveguide-fed, sequentially tagged imaging array. Furthermore, the slot can be easily integrated into a rectangular waveguide wall while maintaining efficient signal coupling. Independent of the location of the slot on a rectangular waveguide, an important issue that must be considered is the structure of the bias lines that feed the modulating PIN diode with which the slot is loaded. The initial design included a thin bias line reaching the inner circular portion of the slot, where the PIN diode anode is connected (See Figure

2.14, in section 2), on the same plane as the slot. This thin line broke the ground plane of the elliptical slot which required two small (0201) surface-mount capacitors to be mounted at that location between the bias line and the ground on both sides. A large array leads to an even larger number of capacitors resulting in additional complexity, cost, and potential for malfunction. The design used here, utilizes the second plane of the PCB to bring the bias line to the circular load through a via as shown in Figure 3.5. The via acts as a high impedance inductive load blocking the RF signal from propagating along the bias line. Furthermore, the bias line does not break the ground in the plane of the slot resulting in minimal change in the resonant characteristics of the slot. The slot is designed by simulating its response when placed on the aperture of a waveguide as explained in the previous section. Table 3.1 shows the final dimensions of this slot structure, which were optimized through extensive simulation and later tuned through experimentations. This final tuning was required due to the slight changes in the dimensions, dielectric substrate material property discrepancy from nominal values, and inaccuracies in placing the via-ring around the slot perimeter. This via-ring is essential in confining the waves within the slot structure. Extensive simulations showed that without the via-ring, wave propagate inside the dielectric substrate which affect the properties of the slot especially when the slot is closed (i.e., leakage increases). The optimum solution would be a solid ring around the slot, albeit not practical with commercial PCB manufacturing technologies. Simulations showed that a dense via-ring with spacing of $\lambda/20$ or smaller is sufficient to confine the wave in the slot and reduce leakage into the dielectric substrate.

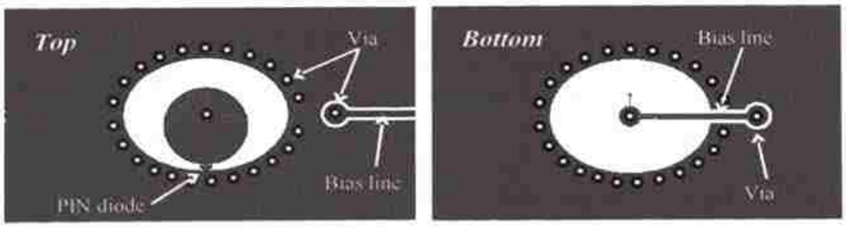

Figure 3.5. Resonant slot with the bias structure.

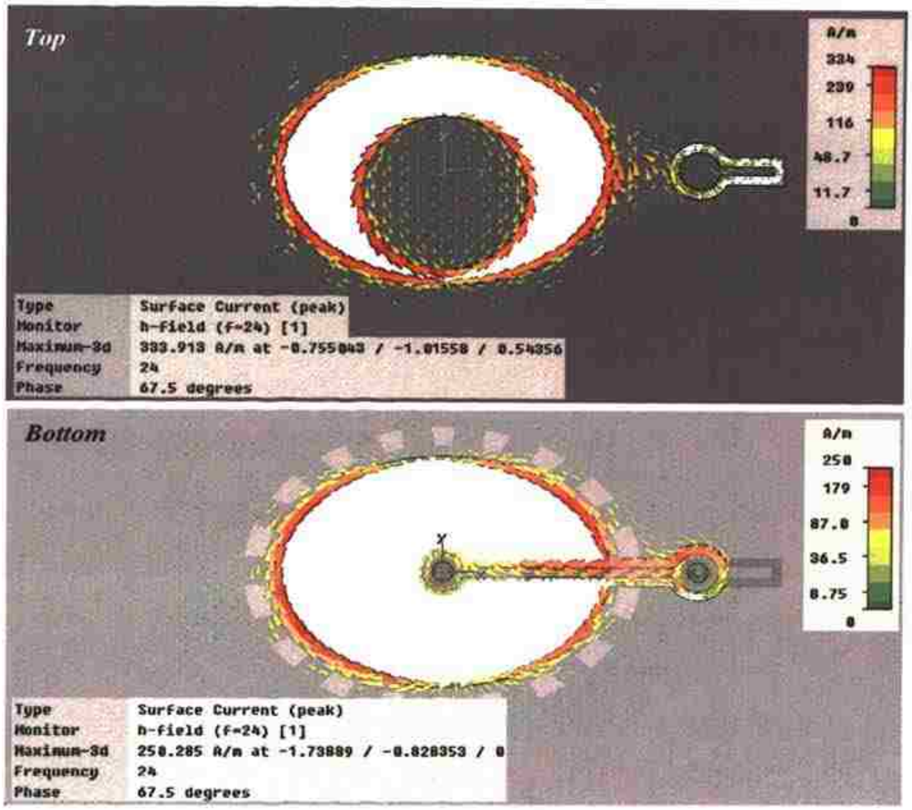

Figure 3.6. Current distribution on the top and bottom sides of the slot structure.

is OFF), the presence of the bias line has negligible effect on the resonant frequency of the slot. The reflection coefficient (return loss) shows a change of 5 dB at the resonant frequency which is also negligible (the scale on the graph is a non-linear logarithmic, and the signal level along with the change must be considered). The change from –25 dB to –20 dB in reflection coefficient corresponds to a very small change in the power transmitted through the slot. This observation is consistent with the intensity of the current distribution on the slot vs. the intensity of the current on the bias line structure. Moreover, when the slot is closed (i.e., the PIN diode is ON), a high (–0.2 dB) reflection coefficient was noticed as it can be seen by the dashed lines. The presence of the bias structure did not affect this reflection and therefore the leakage through the slot. The measured slot response shows a shift in the resonance frequency with an increase in reflection coefficient when the slot is open. As explained earlier, the shift in the resonance frequency is due to slight variations in dimensions and material properties in the manufacturing processes. The increase in the reflection coefficient and the increased leakage (dashed black line) when the slot is open may also be attributed to the non-perfect contact between the slot PCB and the waveguide wall/flange. This issue was verified experimentally by increasing or reducing the pressure on the slot PCB.

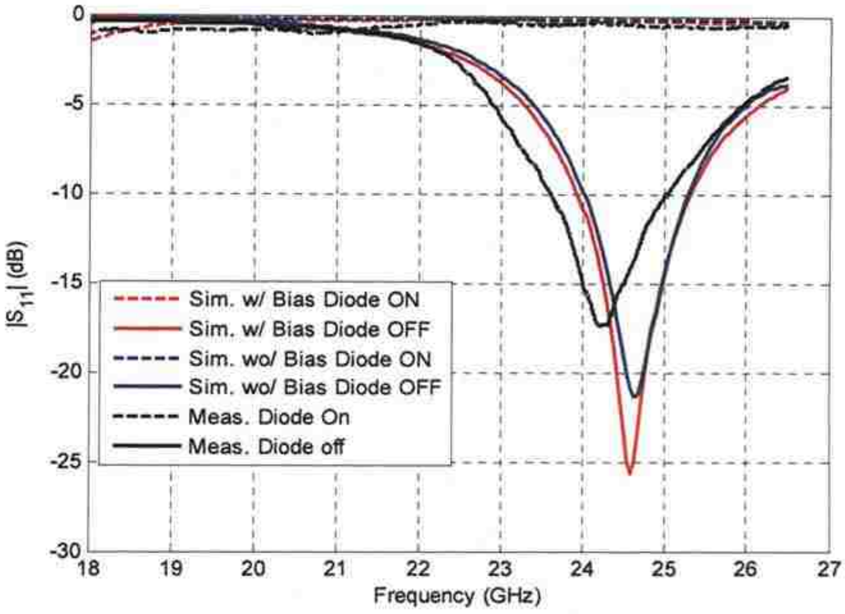

Figure 3.7. Measured and simulated response of the resonant elliptical slot.

Mounting the slot on the aperture of the waveguide is a good method during the design phase for optimizing the slot in simulation or measurements. However, to make the retina array, the slots must be placed on a narrow side-wall of a rectangular waveguide, as mentioned earlier. Subsequent to establishing the slot dimensions as explained above, the signal coupling and radiation properties of the slot, when placed on the narrow side-wall of a waveguide was simulated using CST-MWS. The structure simulated is shown in Figure 3.8 with the waveguide outlines in white. The waveguide has three solid metallic walls and the fourth wall was created by the two-layer PCB containing the slot. The bias structure was not taken into account in this simulation as it was decided that it does not adversely affect the properties of the slot. This structure may be considered as a three-port network, however since the radiation properties of the slot were desired, no port was placed on the slot, and only two ports on both sides of the waveguides were considered. Furthermore, due to the symmetry of the structure, only port 1 was considered active.

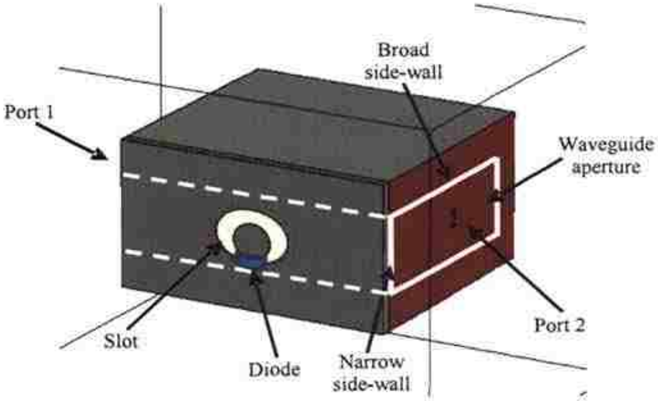

Figure 3.8. Simulated slot on the narrow side-wall of a waveguide.

First, simulations were performed with a slot placed on a standard K-band rectangular waveguide (a = 10.7 mm and b = 4.3 mm), results of which are shown in Figure 3.9a. As seen in this figure, the slot presents minimum perturbation to the waveguide when it is closed (i.e., when the PIN diode is ON, solid lines) which are represented by the total signal transfer between ports 1 and 2 ($S_{21} \approx 0$ dB) and very small reflection back to port 1 ($S_{11} < -30$ dB). On the other hand, when the slot is opened, some power is lost through radiation which can be noticed by the slight dip in S_{21} at 24 GHz. Furthermore, the reflection at port 1 also increased. However, this radiated power is not optimum and must be maximized. In the optimum case, S_{11} and S_{21} will both become –6 dB. In other words, half of the power reaching the slot from port 1 will be radiated, and the other half will be split equally, quarter going to port 2 (S_{21}= –6 dB) and the other quarter going back to port 1 (S_{11}= –6 dB). This phenomenon is better described by plotting the lost/radiated power ($1-|S_{11}|^2-|S_{21}|^2$) as shown in Figure 3.9c. This figure shows that for a standard waveguide, the radiated power when the slot is open (i.e., when the diode is OFF) is less than –6 dB, and when the slot is closed (i.e., when the diode is ON) the radiated power (leakage) is less than –20 dB. Reducing the broad dimension of the waveguide effectively addresses the issue of low radiated power when using a standard waveguide. The reasoning behind this effect will be discussed later. The frequency of operation (24 GHz) is at the high end of K-band, therefore, the waveguide broad dimension may be reduced to 6.25 mm before reaching the cutoff frequency of the waveguide [48]. The waveguide broad dimension was reduced from the standard 10.7 mm to 7.7 mm which brings the cutoff frequency to ~19.5 GHz, well below the frequency of operation. It is desirable to operate at a frequency which is approximately 25% greater than the cutoff frequency such that the propagation constant in the waveguide does not show strong dispersion properties [48]. The slot response on this modified waveguide is simulated and the results are shown in Figure 3.9b. For this modified waveguide, when the slot is closed (i.e., the PIN diode is ON), the waveguide is not disturbed (i.e., $S_{11} < -20$ dB and $S_{21} \approx 0$ dB). Furthermore, when the slot is open (i.e., the PIN diode is OFF) a more prominent dip (compared to the standard waveguide case) is seen in S_{21} which corresponds to more radiated power. Looking at this structure from the radiated power point of view (Figure 3.9c), in the modified waveguide case the leakage when the slot is closed increases slightly, as it can be shown in Figure 3.9c. On the other hand, the radiated power when the slot is open reaches –3.1 dB which is twice as much (3 dB more) as in the standard waveguide case. In other words, approximately half of the power reaching the slot from port 1 is radiated. Again keep in mind that the results are shown in logarithmic scale where variations in the upper end correspond to more change than variations in the lower end. A –3 dB radiated power (50% total efficiency) is considered optimum in the sense that if the slot is used in the receiving mode (as it will be used in the retina), half of the power reaching the slot will travel to each side of the waveguide and no power will be reflected back from the slot.

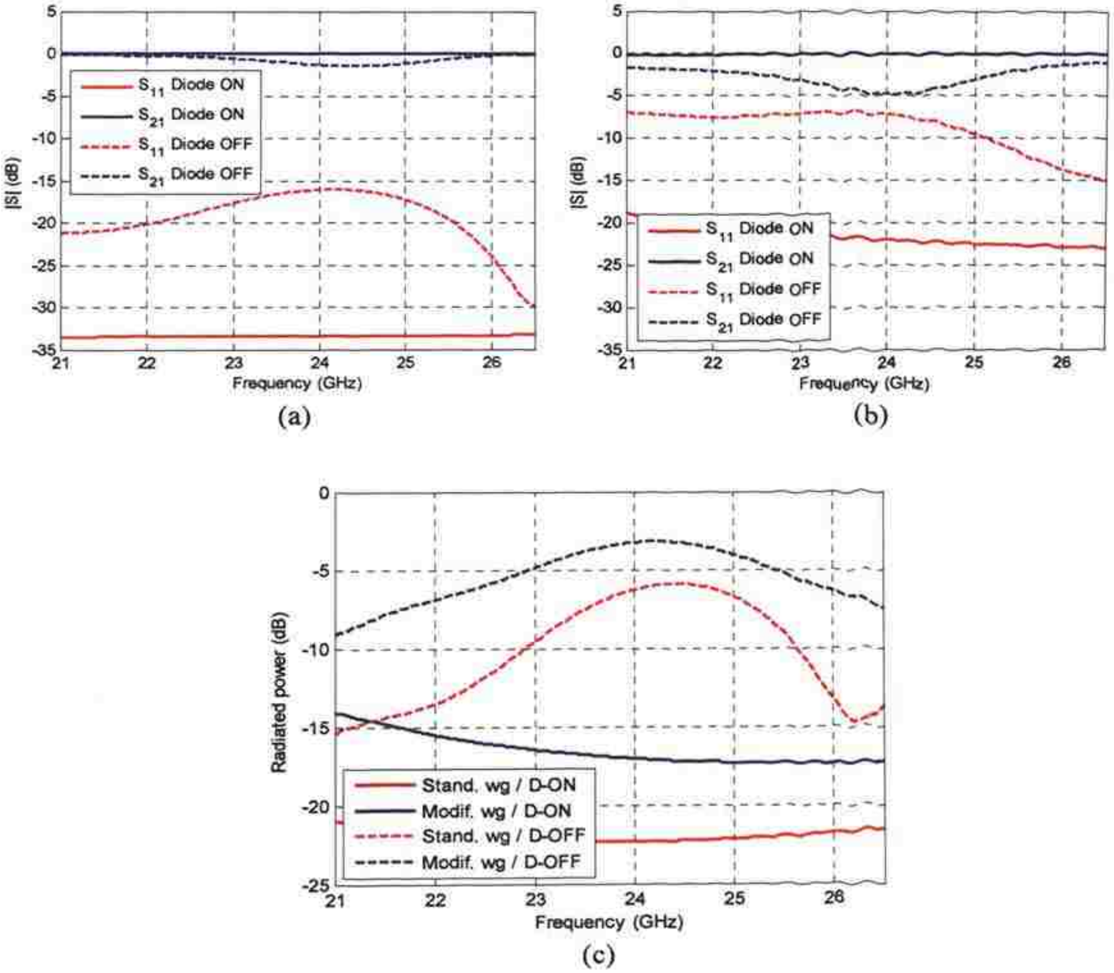

(a)

(b)

(c)

Figure 3.9. Simulated response of the resonant slot on waveguide narrow wall, (a) standard K-band waveguide, (b) modified waveguide, and (c) radiated power.

The increase in the waveguide-slot coupling when the broad dimension of the waveguide is reduced can be explained by looking at the current distribution on the waveguide walls. Figure 3.10 shows a time snapshot of TE_{10} current distribution on a standard K-band waveguide at 18 GHz, which is a frequency nearest to cutoff at the beginning of the band and at 24 GHz, the frequency of interest in this investigation which is at the end of the band. These current distributions were simulated using CST-MWS. The simulations at these frequencies and many other frequencies in between showed that,

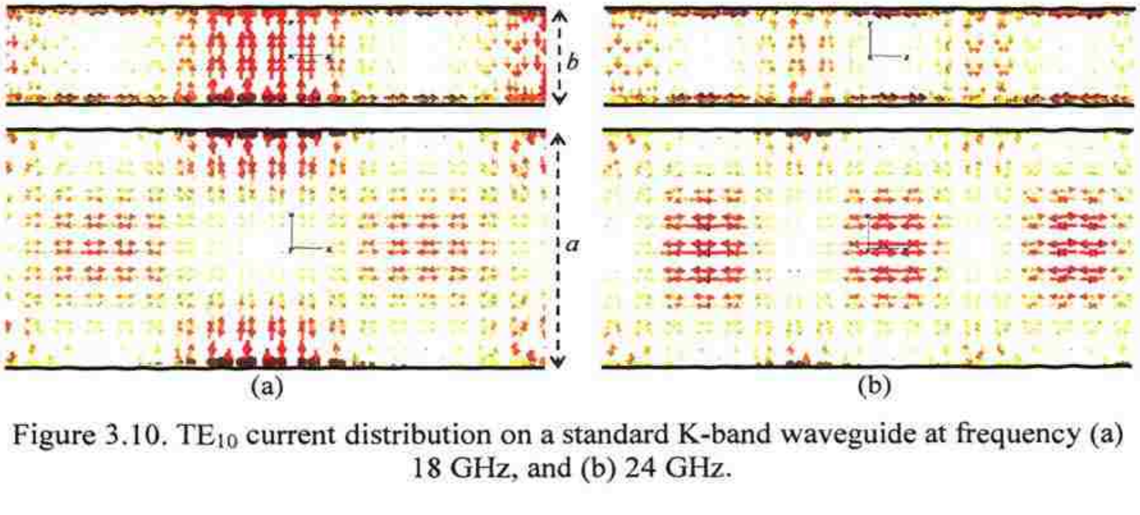

Figure 3.10. TE_{10} current distribution on a standard K-band waveguide at frequency (a) 18 GHz, and (b) 24 GHz.

the peak currents has more intensity at the narrow side-wall of the waveguide at the lower frequencies, and as the frequency increases, the peak intensity on the narrow side-wall decreases while the peak intensity on the broad side-wall increases. This phenomenon explains the week coupling to the slots encountered at 24 GHz when placing the slots on the narrow side-wall of a standard waveguide. By reducing the broad dimension of the waveguide, the frequency of interest becomes near the cutoff frequency which intensifies the currents on the narrow side-walls, as shown in Figure 3.11.

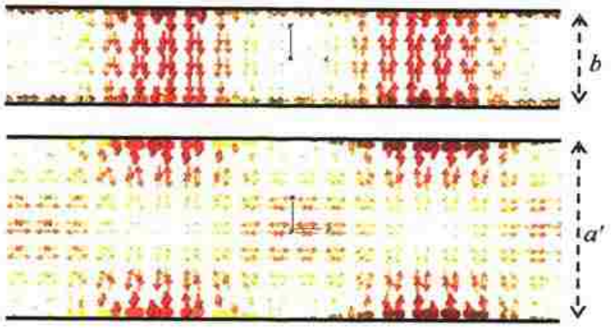

Figure 3.11. TE$_{10}$ current distribution on the modified ($a' = 7.7$ mm) K-band waveguide at 24 GHz.

3.3.2. Retina Addressing Scheme. Electronically scanning the retina will require that each individual slot be tagged while the other slots are idle (i.e., sequentially scanned retina). This method of operation results in a time-multiplexed signals of the spatial electric field distribution over the retina space. Addressing each individual slot separately through a bias line (i.e., direct addressing) allows for such operation but it requires 24 × 24 = 576 bias lines and connectors to bring 576 bias lines to the retina and a control circuitry that can drive 576 simultaneous outputs. This solution is not feasible, in addition to the fact that there is not enough space on the retina to route this many bias lines. A solution to such problems is the matrix addressing scheme commonly used in electronic displays. Matrix addressing scheme is illustrated in Figure 3.12. In a matrix addressing scheme for an M×N array, only M+N addresses (or bias lines) are needed. In this scheme to address a slot at the intersection of a row and a column, its corresponding rows and columns are addressed. To perform the electronic scan of the retina, first a row is enabled by properly biasing the line, and then the various elements in that row are scanned by sequentially addressing the columns which may also carry the modulating signal. Subsequently by going through all rows, the 2D electronic scan is performed.

A major disadvantage of using the waveguide-fed elliptical slot is that the slots have to be closed in normal operation (i.e. when idle and not tagged), and then sequentially opened (or modulated) to receive the signal. Closing the slots requires forward biasing the PIN diode. Considering that each PIN diode nominally requires 5 mA to be turned ON or forward biased, the 576 PIN diodes of the retina will cumulatively require more than 2.8 Amperes of current. Furthermore, this current can go as high as 10 mA per diode when saturated as a result of a slight increase in the bias voltage. Moreover, when modulating a line, each row or column of the bias line should be able to switch currents higher than 120 mA (for 24 slots) at modulation frequencies of up to a couple of MHz. The design of the modulation and switching circuitry will be explained towards the end of this section.

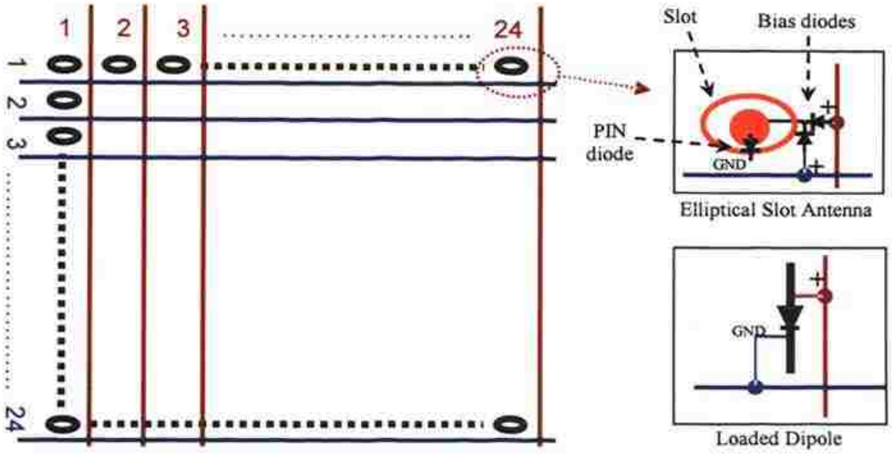

Figure 3.12. Matrix addressing scheme.

In a matrix addressing scheme such as those of displays, one of the address dimensions (e.g. columns) is connected to a voltage supply (positive) and the second dimension (rows) is connected to the ground. By pulling the column line high and row line low for a particular element in the array, that element is activated as illustrated with the loaded dipole in Figure 3.12. This is possible since both the cathode and the anode are floating. In the case of this particular elliptical slot antenna, the cathode of the slot PIN diode is always connected to ground. Furthermore, the slot must be idly closed (i.e., its PIN diode is ON). These two requirements of addressing the slots individually and

The row address lines were etched as 0.005″ wide horizontal lines onto the top layer at midpoint between the rows. On the other hand, thin (0.005″-diameter) insulated wires were used for the column address lines and were soldered at each slot location to its corresponding red LED. The LEDs and the bias lines are expected to have a slight effect on the radiation properties of the slots. However, the low cost and ease of fabrication overruled any slight effect these components might produce. This retina was placed on top of the waveguide collector array and secured using the top rim. Conductive epoxy ensured direct electric connection between the waveguide walls and retina PCB.

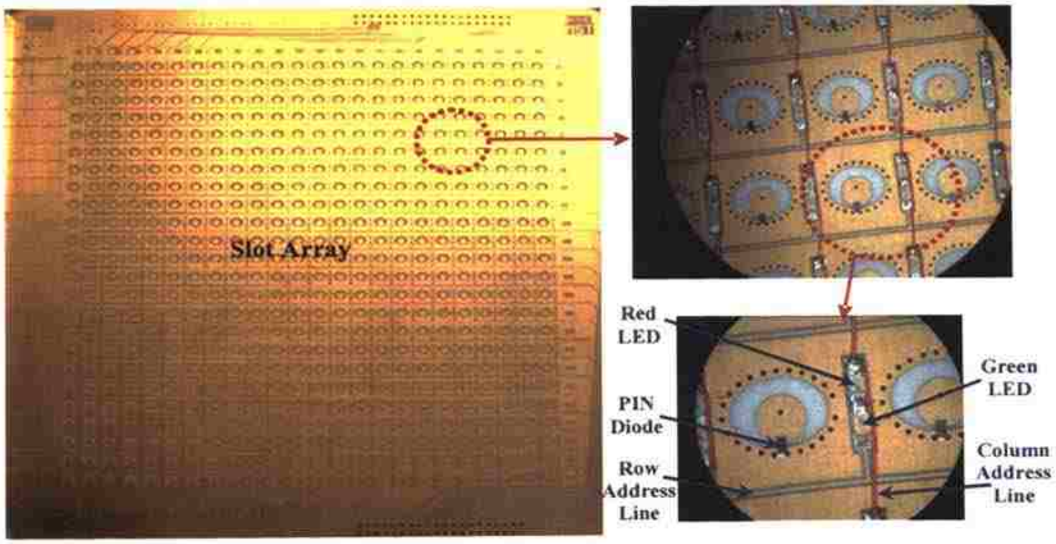

Figure 3.13. Retina PCB showing the bias lines, the bias LEDs, and the slots,

3.4. COMBINER WAVEGUIDE

Several methods were investigated to combine the 24 rows of the signal collecting waveguide network into access ports. The first option considered was using waveguide bends to connect all rows together making one long waveguide, as illustrated in Figure 3.14a. This solution was investigated in [47] and it proved attractive for a small retina for its simplicity and ease of manufacturing. However, given that each waveguide with 24 slots is anticipated to have as much as 7 dB of signal loss due to leakage from the slots (0.28 dB per slot), the signal received from the slots in the middle rows would experience more than 75 dB of attenuation before it reaches the nearest port, rendering this solution impractical.

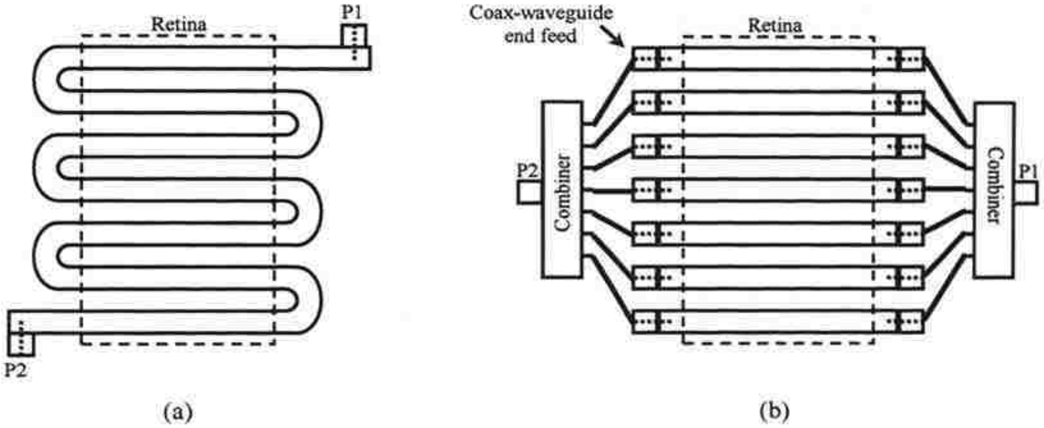

Figure 3.14. Schematic of investigated combiner solutions: (a) one waveguide solution, and (b) external combiner solution.

The second solution investigated (Figure 3.14b), involved access ports on both sides of each row. This option has many advantages. The output of each collector waveguide may be amplified before entering the combiner. The combiner may include a switching functionality to route the signal to a single line or selected group of lines. A switching functionality enables the isolation of certain row of the array which can be used to transmit a signal in the case of reflection-mode operation. The most attractive advantage of this combining option is the ability to perform parallel modulation on one column of the retina, which can save significant amount of time in image acquisition when using large arrays. Since slots on each column do not share waveguides, by modulating all of them at the same time, they would not significantly interfere with each other. Therefore, one can modulate sets of slots (one column at a time) with well-established techniques such as orthogonal coding. With parallel modulation it is possible to reduce acquisition time by a factor of $log_2(N)$ where N is the number of slots being orthogonally modulated at the same time.

Since the waveguide collection network of Figure 3.4 share the broad walls of the waveguides, a simple coaxial side-feed was not feasible and an end-feed scheme was required. The option investigated was to utilize a finline structure to transfer the signal from a printed coplanar waveguide (CPW) to a rectangular waveguide [49]. As shown in Figure 3.15, the finline investigated utilizes cosine taper of length λ/2 due to its lowest return loss [50]. A Balun provides matching between the CPW and the finline transition [49]. This feed structure was optimized through extensive simulations in CST-MWS.

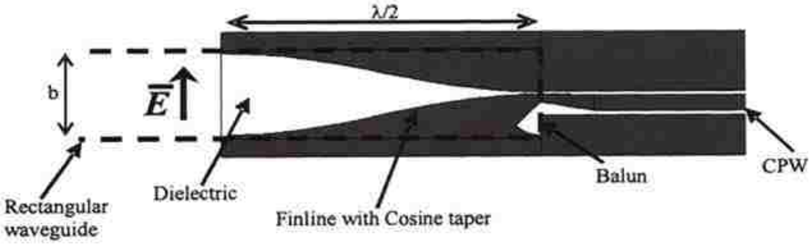

Figure 3.15. Finline waveguide feed.

Subsequent to optimizing the finline design, a test fixture as shown in Figure 3.16, was built and tested. This test fixture contained a 2″ section of waveguide terminated at both sides with a CPW-Finline transition. The waveguide indicated by the dashed lines was machined into two aluminum blocks. The waveguide was mainly in the bottom block while the top block serving as a cover only, except for the finline location since the finline must be placed in the middle of the broad wall of the waveguide. The finline was made on a PCB with a Rogers4350 substrate. The CPW side of the finline transition was terminated into an SMA connector which was rated to 26.5 GHz.

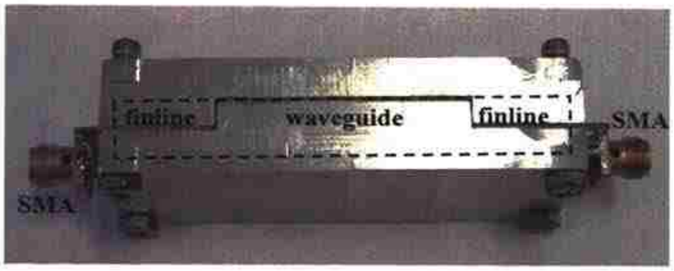

Figure 3.16. CPW-finline-waveguide transition test fixture.

Figure 3.17 shows measured and simulated response of the test fixture in Figure 3.16. While the simulated results show a desirable return-loss of 20 dB and a small insertion loss of 0.5 dB, the measured results are far from desirable. For this structure the measurements show a loss of up to 2 dB and increased reflection at the ports. Further investigation and measurement of the loss on a 1″-CPW line of similar properties and terminated in similar SMA connectors showed that the majority of the loss is encountered in the PCB portion of the finline transition. Furthermore, the imperfect contacts and gaps on the joints between different waveguide blocks and the finline PCB are believed to contribute to the higher reflections and loss, as well.

Overall, efficient coupling to a waveguide using an end-feed was not trivial and proved to be costly. Furthermore, the SMA connectors on a thin PCB are not mechanically robust. Other than the difficulties in building an efficient end-feed, the scheme of Figure 3.14b has few other drawbacks. For example a 24-to-1 low-cost combiner such as those utilizing Wilkinson design, will introduce a minimum signal loss of 12 dB not including the dielectric and radiation losses at these high frequencies. Due to the above reasons, this design – although desirable from the functionality point of view, was abandoned.

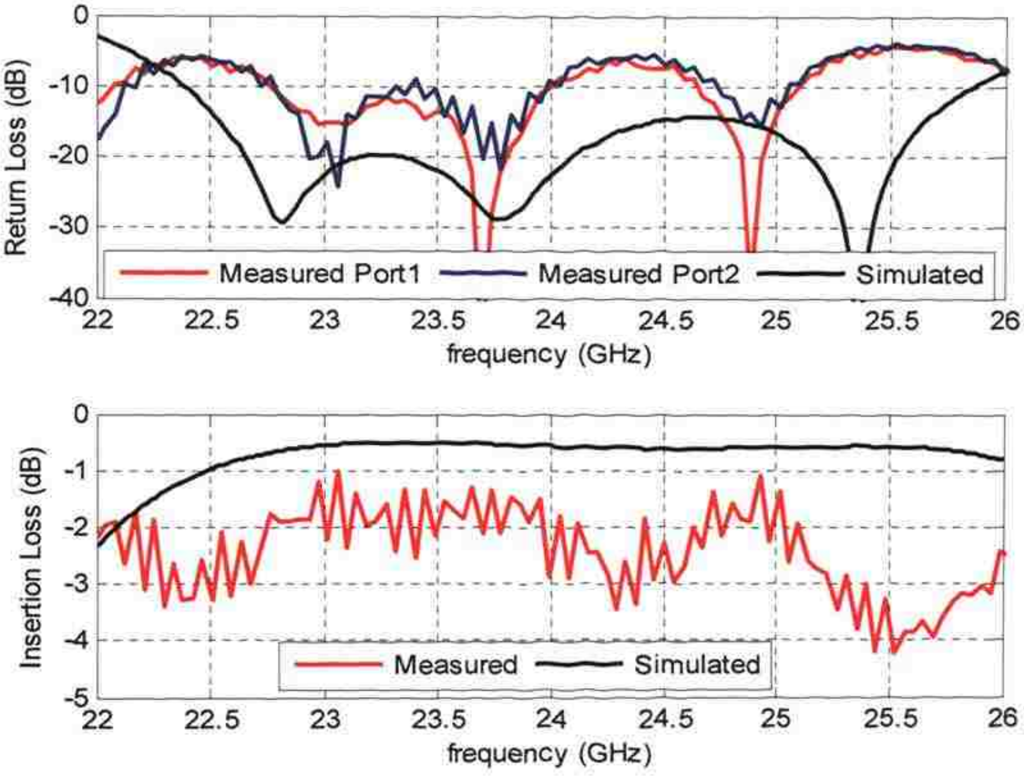

Figure 3.17. CPW-finline-waveguide-finline-CPW simulation vs. measurement.

The combining method, which was finally used, is shown in Figure 3.18. This method utilizes a switchable iris at each end of each collector waveguide. The iris of choice was the resonant PIN diode-loaded elliptical slot placed in the wall between the waveguides. Using this method, the signal received from each slot is routed to four output ports – two ports on each combiner on each side of the camera, by properly switching the desired iris. Using this method, the maximum attenuation experienced by a signal before reaching the nearest port is less than 12 dB. This attenuation is mainly due to the leakage in the slots and the combiner irises.

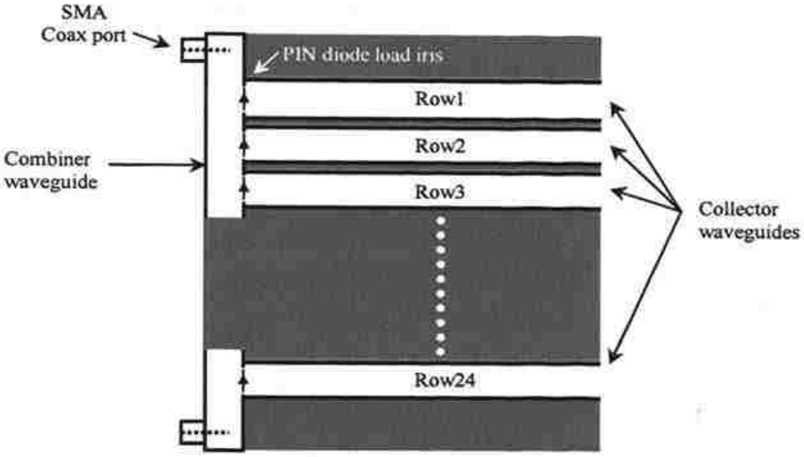

Figure 3.18. Switched waveguide combiner.

To ensure maximum signal transfer from the retina to the output ports, only one of the combiner irises should be open at each time. In ideal situations when the irises have zero leakage, the connection between each collector waveguide and a combiner waveguide is considered as an E-plane Tee with a switchable iris. Figure 3.19 shows the Tee configuration simulated in CST-MWS. The switchable iris is the PIN diode-controlled resonant elliptical slot designed to work at 24 GHz, as described earlier. In this configuration, port 1 represents the collector waveguide side and ports 2 and 3 represent the combiner waveguide side. Ideally, it is required that the signal reaching the junction from port 1 be divided equally into ports 2 and 3 when the switch is open. On the other hand, when the switch is closed any signal in the collector waveguide (port 1) should not enter the combiner waveguide (i.e., there should be high isolation between port1 and ports 2 and 3). Yet any signal in the collector waveguide should travel from one side to the other without experiencing any attenuation or distortion.

Figure 3.20a shows the simulation results for the case when the switch is open. It is established that a reciprocal and lossless three-port device cannot be simultaneously matched at all of its ports [48]. Furthermore, only the network properties (S- parameters)

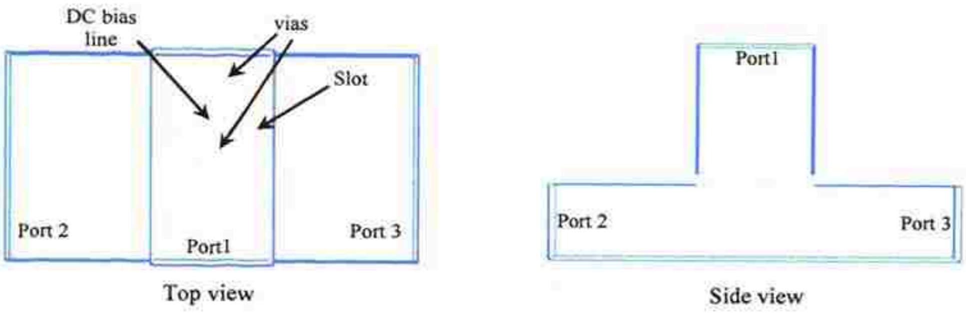

Top view

Side view

Figure 3.19. Configuration of the simulated switched waveguide Tee.

at the resonant frequency of 24 GHz are of interest. The values of these S-parameters at 24 GHz are shown in the legend/marker. Figure 3.20 shows the response vs. frequency to confirm the resonant frequency of this switch. At the resonant frequency the power division in the Tee (S_{21} and S_{31}) is a corresponding -3.9 dB which is close to the ideal value (-3 dB). On the other hand, the reflections (S_{11}, S_{22}, and S_{33}) are around -10 dB. To reiterate, it is impossible to create a matched power divider. Overall, these reflections are acceptable, given the difficulties associated with alternative designs, as mentioned earlier. On the other hand, when the switch is closed (Figure 3.20b), the isolation (S_{21} and S_{31}) is at the level of 20 dB, while ports 2 and 3 show small reflections (i.e. matched). Moreover, the signal traveling through the collector waveguide experiences a very small amount of loss ($S_{23} < -0.1$ dB). This test setup of a single iris in a waveguide Tee (shown in Figure 3.19) was not manufactured and therefore the results were not verified experimentally.

For the final application of designing a combiner for the imaging system, 24 irises were manufactured on a single 0.020″ thick 2-layered PCB with Rogers4350 laminate. This board was sandwiched between the combiner waveguide and the array of collector waveguides, as shown in Figure 3.21.

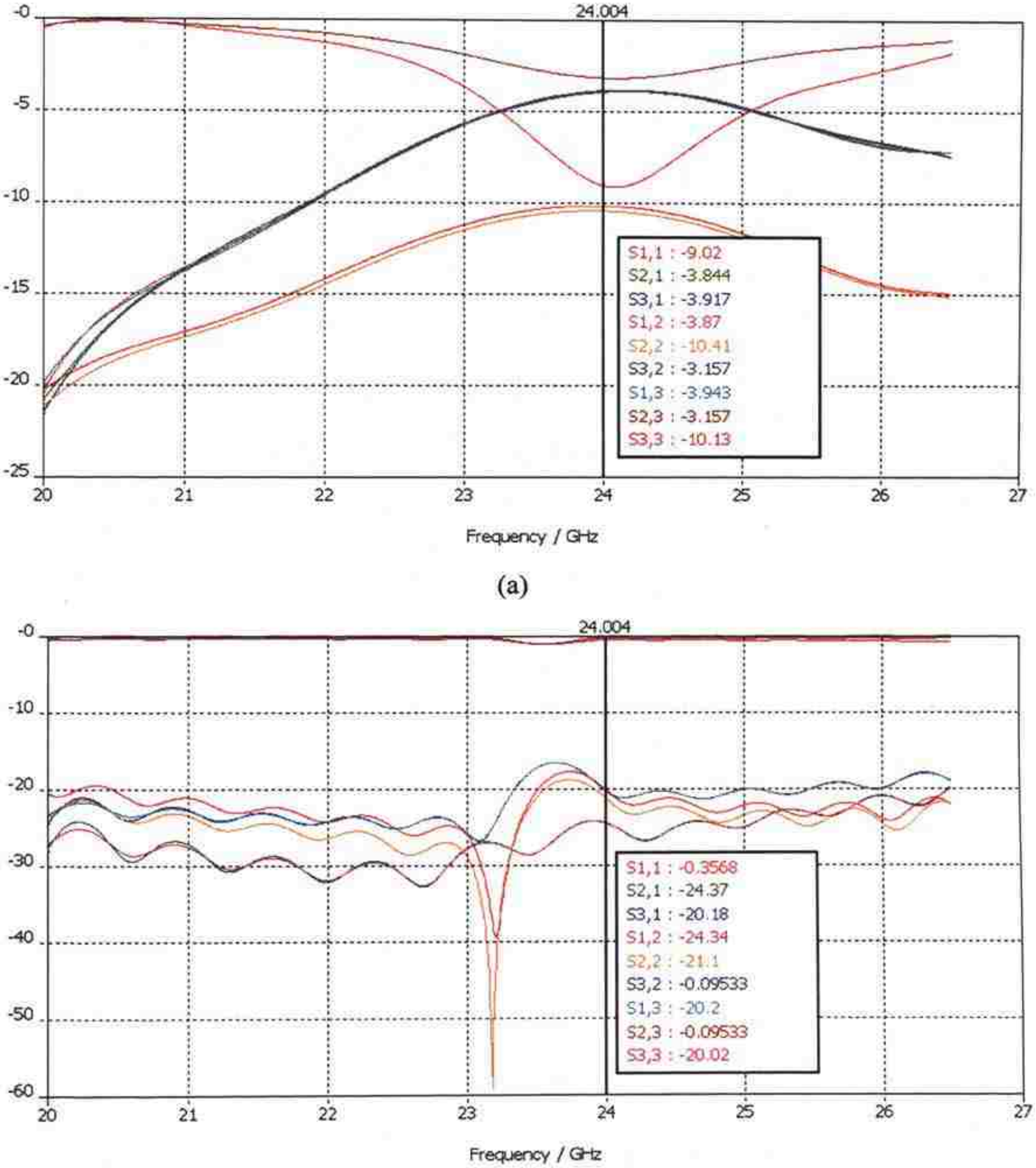

(a)

(b)

Figure 3.20. Simulation results of the switched waveguide tee: (a) switch is open, and (b) switch is closed.

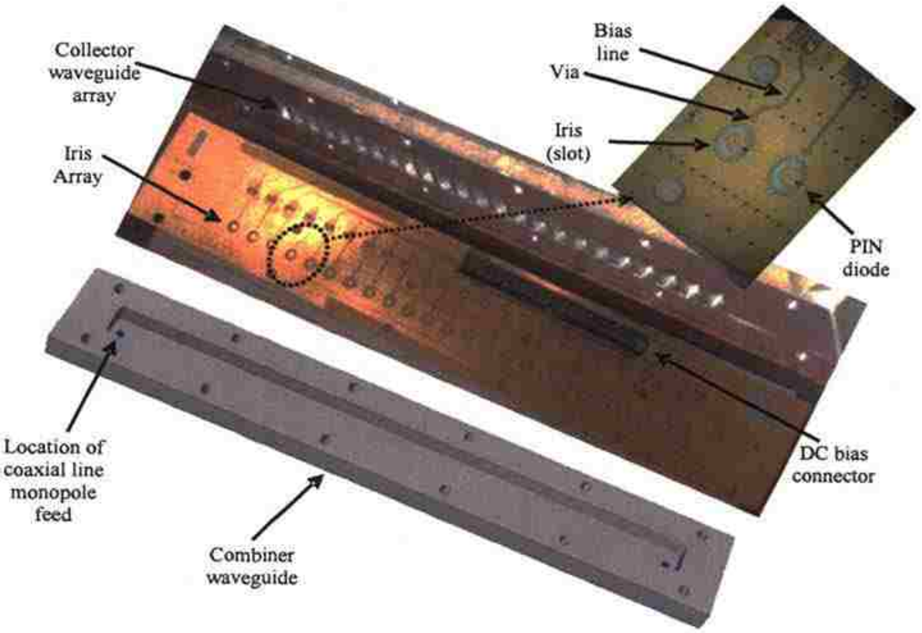

Figure 3.21. Combiner waveguide assembly.

Figure 3.22 gives an indication on the switching capabilities of the combiners and the loss signals face while traveling though the waveguide collector network. The measurements were performed using the HP8510C VNA. The transmitted coefficient (S_{12}) between each two ports of the camera for opening the irises of the combiners, one at a time is shown. For this experiment, all the slots on the retina were closed. The transmission coefficient between ports 1 and 3 shows a semi-linear loss as the signal travels a larger distance through the combiner waveguides. The difference between the first row of the collector waveguides and the last row is approximately 25 dB. Similar response is noticed between the other two ports of the retina (i.e., ports 2 and 4). If it is assumed that the loss is equal in each combiner, the result is a loss of 12.5 dB per combiner waveguide which corresponds to approximately 0.5 dB loss per iris much larger than the simulated value (0.1 dB). The 0.5 dB loss per slot was also measured using a single slot on a waveguide aperture, and is mainly attributed to the imperfect contact between the waveguide walls and the slot PCB.

The transmission coefficient between ports 1 and 4 shows an average of –25 dB. If it is assumed that the combiners switches –4 dB of the signal into the collector waveguide (–3.9 dB in simulation), subtracting the –4 dB once for each combiner results in –17 dB of the signal lost in the combiner and collector waveguides (–25 – 2×(–4) = –17 dB). Consequently, if we assume that 12 dB of that loss is due to the combiners, the result is a 10 dB loss in the collector waveguide which is 3 dB more than the theoretical value. On the other hand, if it is assumed that the collector waveguide have a loss of 7 dB then the combiners must have switched –5.5 dB of the power only. In reality, this extra loss in the system may be distributed loss, not accounted for such as leakage through the gaps at points of mechanical interconnects such as flanges. Furthermore, reflections will also contribute to the loss seen in the transmission coefficient.

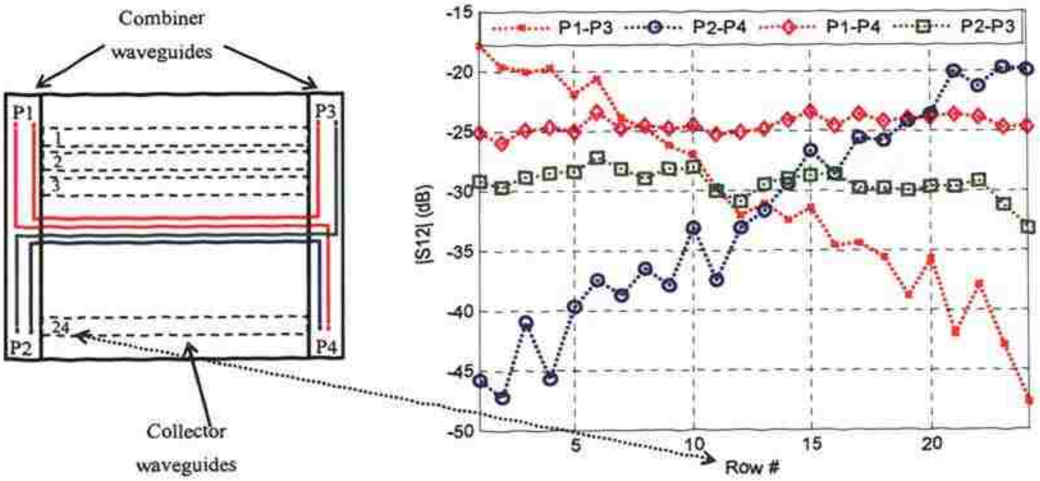

Figure 3.22. Measured signal loss through the waveguide collection network and the combiners.

Measuring the transmission coefficient through the other two opposite corners (ports 2 and 3) show an average of 5 dB more loss compared to the first case. This extra loss is attributed to the mismatch in port 2. This mismatch was cause by manufacturing errors which caused the monopole coax feed of port 2 to be slightly bent. This fact was verified by visual inspection. It may be also noticed in the transmission coefficient between ports 2 and 3 when the combiners were switched to collector waveguides at rows 23 and 24. This design as manufactured did not show ideal or even close to ideal performance in reflections and loss. However, it was desirable since it provided lowest overall signal loss compared to other alternative designs, as explained earlier. Furthermore, it has a compact form factor, since it adds less than 0.5″ to the width of the camera on each side.

3.5. SIGNAL SOURCE AND RECEIVER

The transceiver design was based on a heterodyne scheme; where as the first harmonic of a single side-band of the modulated signal is demodulated. This scheme was first introduced by [51] in order to improve measurement accuracies by eliminating the quadrature error associated with high frequency components. In that design the mixing was performed down to baseband, such that the IF stage frequency is the fundamental frequency of the modulating signal. In the design presented here the mixing is performed in a way to make the IF stage frequency a fixed 10.7 MHz irrespective of the modulation frequency. This design has several advantages over the design introduced by [51]. First, the fixed IF frequency provides the flexibility of changing the modulation frequency without changing the IF stage hardware. Second, the higher IF frequency of 10.7 MHz used here compared to the low IF frequency which is the modulation frequency of less than 1 MHz used in [51] translates to lower flicker ($1/f$) noise. Third, the higher IF frequency translates to larger frequency difference between the RF sources reducing the design complexity associated with the sources. Finally, utilizing a standard IF frequency such as 10.7 MHz, allows for a greater selection pool of commercially available components. This scheme is illustrated in Figure 3.23. The main RF source generates a signal which is sent through the transmitter to illuminate the target. The received modulated signal (through the retina) is down-mixed to the IF stage where is it filtered and amplified. Subsequently, the demodulator provides the estimate of the signal at the retina aperture. This imaging system requires four receiver channels. This section provides the design of the individual components of this system. A detailed description of the operation characteristics of this receiver and an analysis on its performance is provided in the next section.

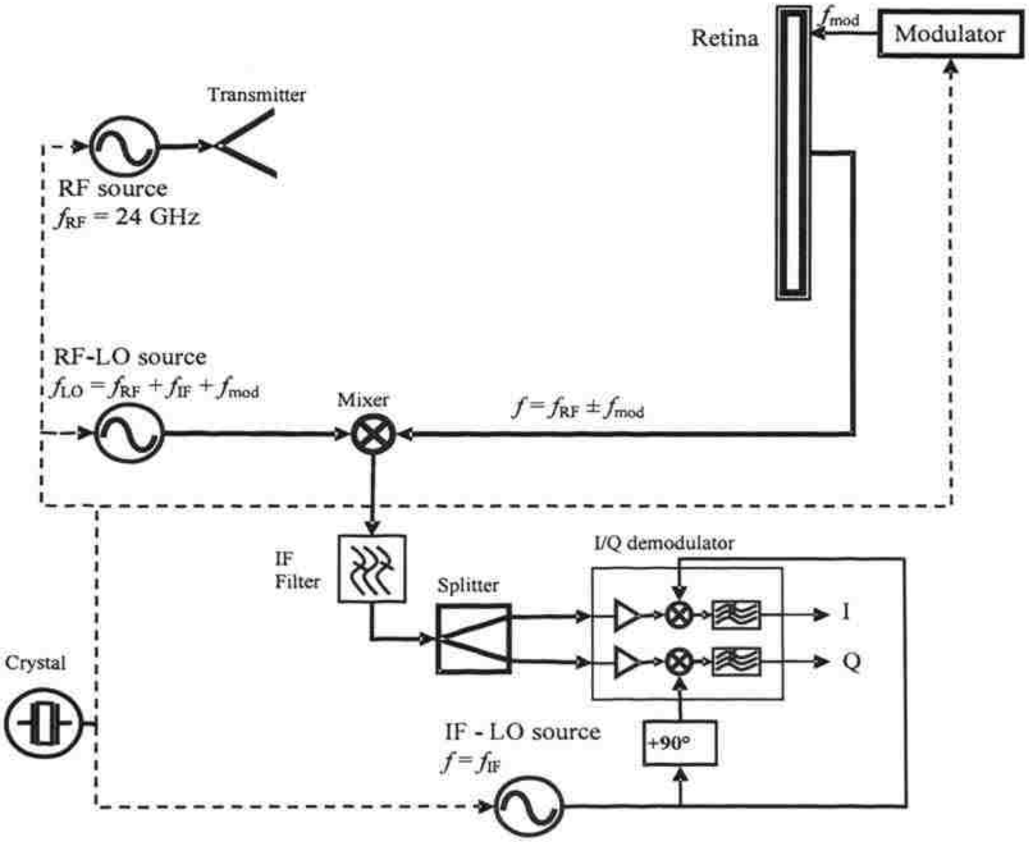

Figure 3.23. Schematic of the sources and one channel of the receiver.

There is one fundamental difference between this design and the more traditional MST receivers [34]; namely, the lock-in amplifiers. In this scheme the IQ demodulator serves as a quadrature lock-in amplifier which performs the match-filtering on the first harmonic of the square-wave modulated signal. The disadvantage of this scheme is that, capturing the first harmonic results in approximately 4.8 dB power loss, 3 dB of which is for ignoring one side-band and another 1.8 dB for ignoring the harmonics of the square-wave signal. To summarize, this design is selected for its high-accuracy and dynamic-range provided by a heterodyning scheme, a flexible frequency control provided by a fixed IF frequency, and finally an accurate IQ demodulator that also act as a matched filter. Overall, the signal power loss is compensated for by the high dynamic-range and sensitivity of the receiver and ability to filter and amplify the IF signal.

3.5.1. RF Sources. Figure 3.24 shows the schematic of the RF sources. A fractional synthesizer is used to control the frequency of each RF source. Using fractional synthesizers allows for the small and precise difference (10.7 MHz + f_{mod}) in frequency between the two RF sources using a high phase detector frequency (PFD) in the PLL [52]. This high PFD frequency of 20 MHz used in the fractional synthesizer in this design – compared to a maximum of ~60.79 KHz that would have been used with an

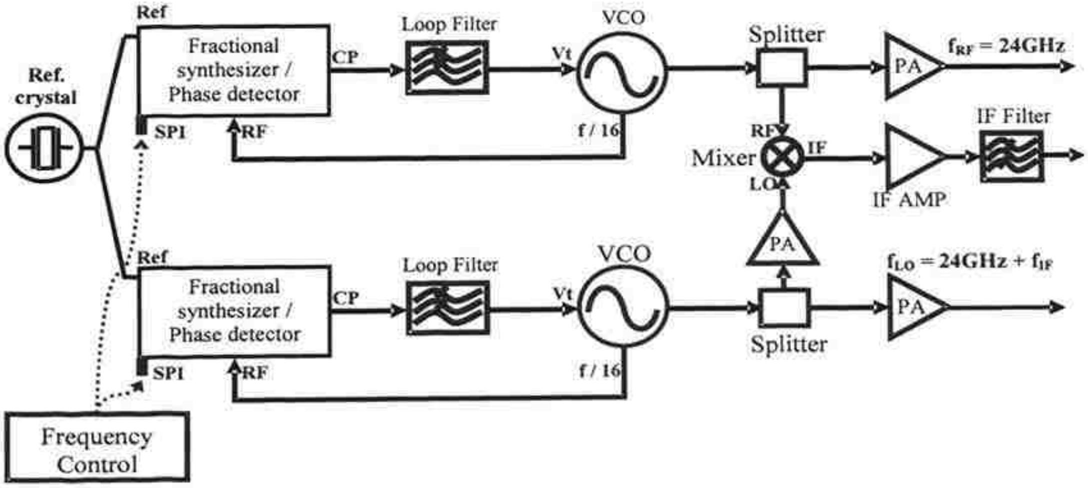

Figure 3.24. Schematic of the synthesizer controlled RF-source board.

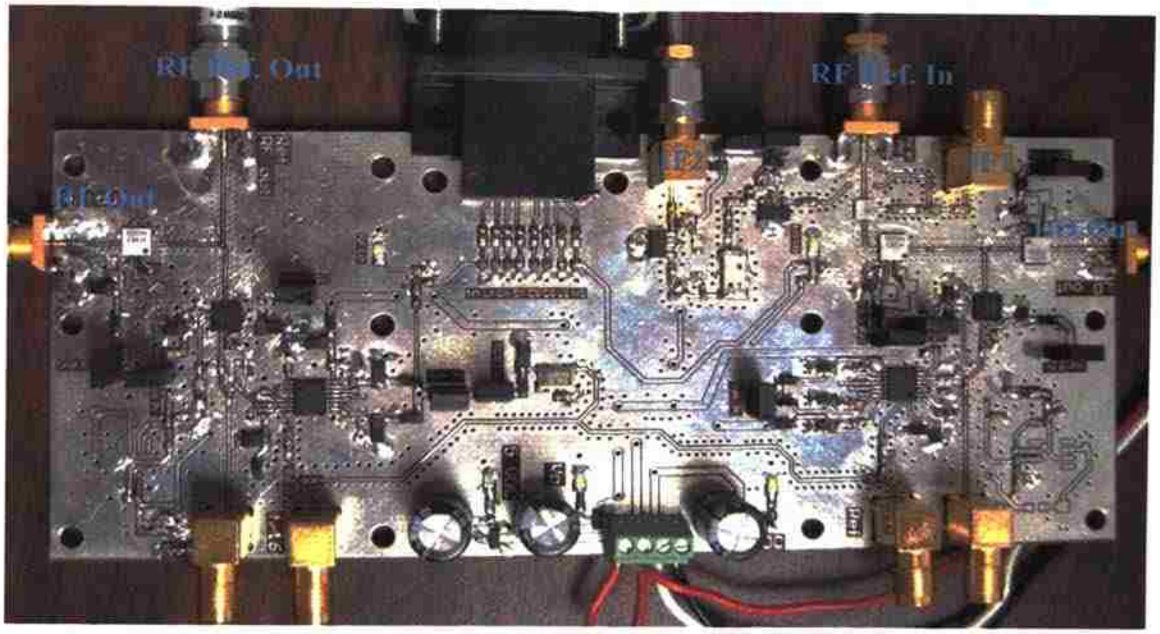

Figure 3.25. Picture of the RF-source board.

Figure 3.27 shows the RF and LO sources which are shifted from each other by 10.7 MHz. It also shows that when both the RF and the LO sources are ON, due to radiation cross-talk and the nonlinearity of the power amplifiers, the signal spectrum has spurs at their difference frequency. The radiation cross-talk is greatly reduced by shielding at least one of the sources. Eventually, due to the fact that the received signal through the camera will be modulated, the majority of these spurs and any other unwanted signal are not expected to pass through the IF filters. Finally, Figure 3.28 shows the spectrum of the difference (IF signal) which is set to 10.7 MHz. Using this figure, an estimate of the phase noise in both sources combined is obtained to be approximately -60 dBc at 10 KHz and -90 dBc at 100 KHz offset. These figures are close to the specification of the VCO which is -70 dBc at 10 KHz -95 dBc at 100 KHz.

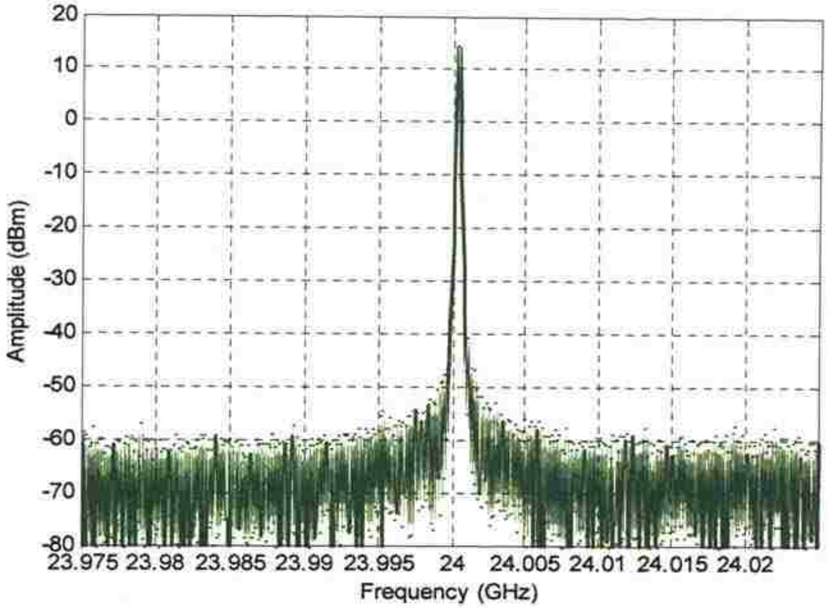

Figure 3.26. Signal at RF out port, RBW=100 KHz, VBW=100 KHz.

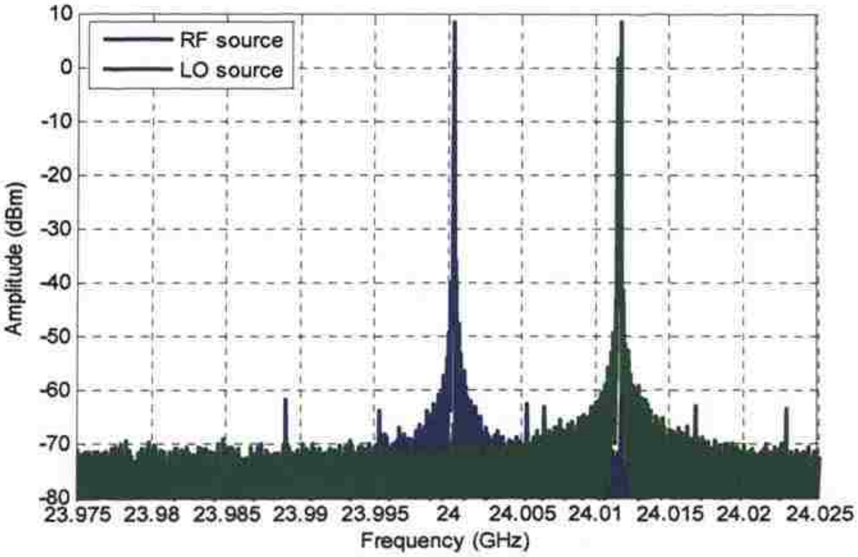

Figure 3.27. Signals spectrum at RF out port and LO out ports, RBW=10 KHz, VBW=10 KHz.

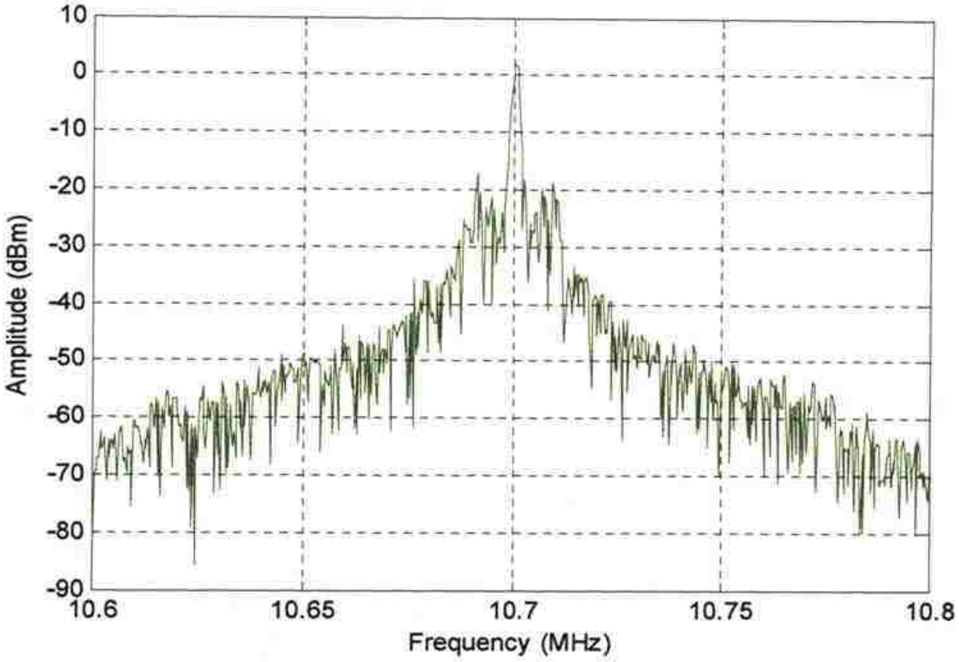

Figure 3.28. Signals spectrum at IF2 out port, RBW=1 KHz, VBW=1 KHz.

3.5.2. Receiver Front-End. The RF receiver has four identical down conversion channels. Figure 3.29 shows the schematic of one of these channels. Each channel includes a down conversion mixer, a power amplifier to drive the mixer, and an RF low noise amplifier (LNA). The power amplifier and the mixers were similar to the ones used in the sources board. The LNA (HMC517LC4 from Hittite) has a noise figure (NF) of 2.5 dB and a gain of 20 dB. The LNA is most critical part of the receiver which dictates the overall NF of the system. The effect of the various components' NF on the overall noise floor of the system will be analyzed in section 4. The IF signal produced by the mixer goes through an IF amplifier with a 20 dB gain, a ceramic band-pass filter centered at 10.7 MHz and with a bandwidth of 100KHz, and then another IF amplifier with a gain of 20 dB.

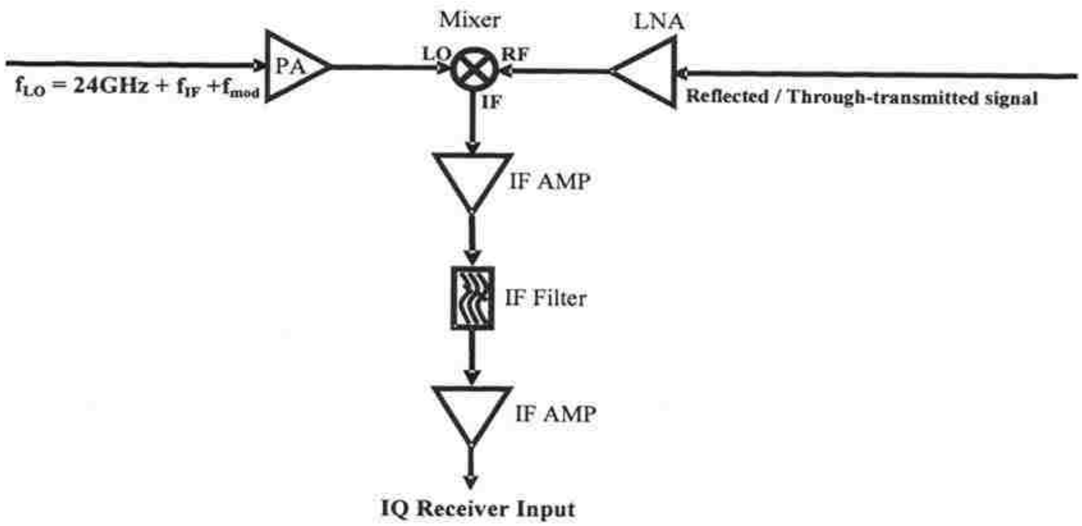

Figure 3.29. Schematic of the receiver front-end.

As shown in Figure 3.30, each two channels are placed on a single board. Various test points are provided at the IF stage. First test point is at the output of the mixer, the second is at the output of the filter, and the third test point is at the receiver output. The noise power reaching the demodulator is directly proportional to the filter bandwidth. It is desirable to have a narrow filter bandwidth. On the other hand, the group delay in the filter is inversely proportional to the filter bandwidth. Therefore, speed associated with electronically scanning the retina puts a lower limit on the filter bandwidth. Furthermore, slight shift in the frequency must be anticipated and allowed for in the selection of filter bandwidth. Since this design is a prototype, the filter bandwidth was selected to be larger than the optimum value. Moreover, the system will have other filters at the output of the demodulator and as averaging in the acquisition stage. The response of all these filters must be cascaded to determine the overall system bandwidth. Section 4 will show the cascade of the filter and provide and analysis on the selection of an optimum filter bandwidth.

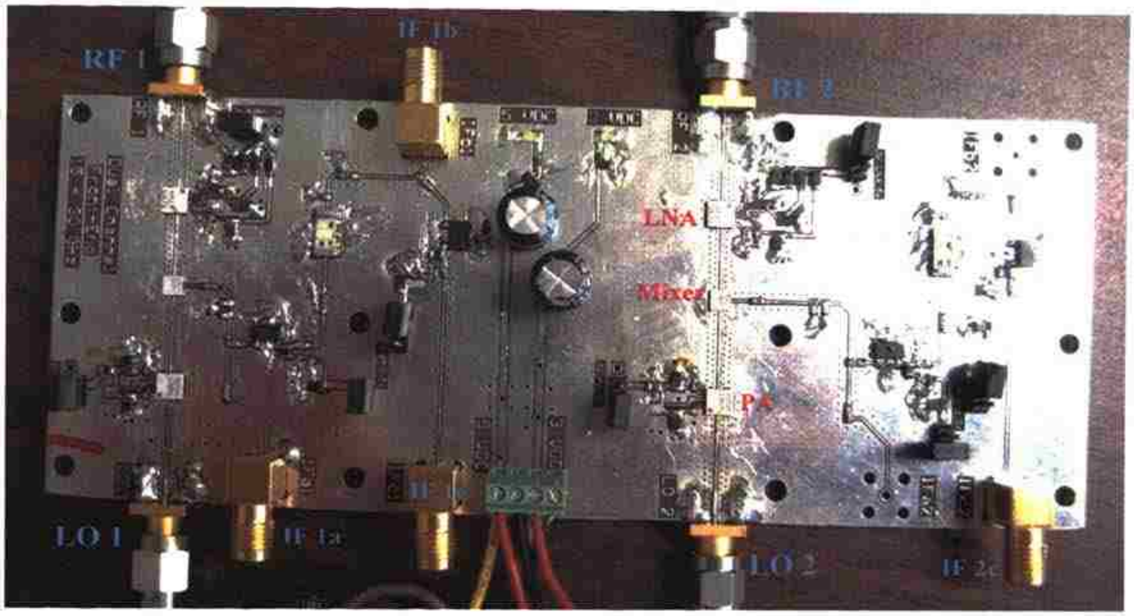

Figure 3.30. Picture of a two channel RF front-end.

In order to test the dynamic range of these channels, a measurement setup as shown in Figure 3.31 was used. Two physically separate sources for the RF and LO were used to eliminate any possible cross-talk between them. A very stable RF source from an 8510C VNA was used as the source. This source output power was then attenuated using a precision variable attenuator (HP8495D) along with few fixed attenuators to extend the measurement range. A spectrum analyzer was then used to measure the output power. The result of this test is shown in Figure 3.32, which indicates that these receivers had a dynamic range of more than 100 dB. The linear dynamic range of this front-end has have a direct impact on the dynamic range, and sensitivity of the overall system since it represents the first stage (beyond the sources). The final system is not expected to a have a dynamic range of more than 70 dB, although a large dynamic range in individual stages of the system contributes to a larger overall system dynamic range, which is desirable.

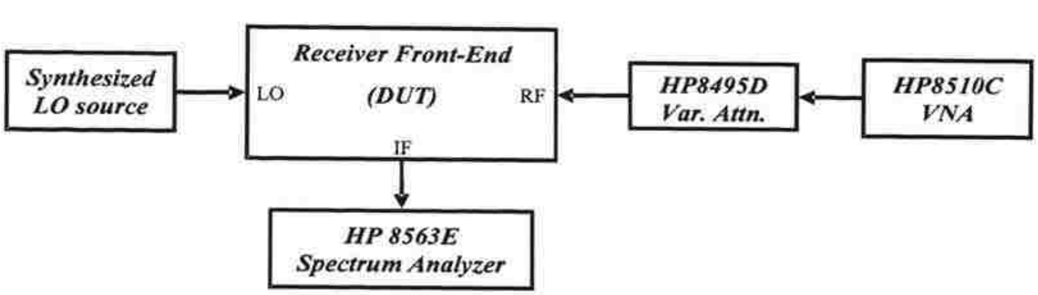

Figure 3.31. Test setup for measuring the dynamic range of the receiver.

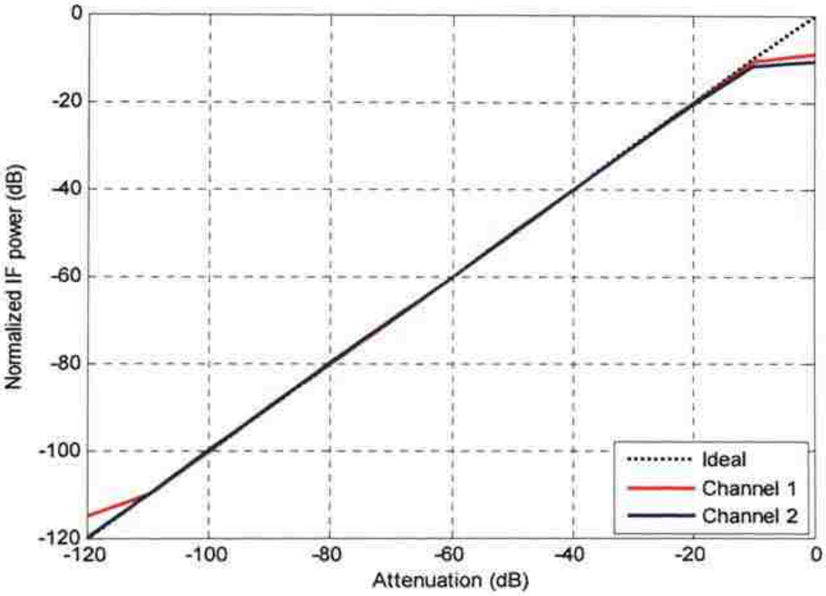

Figure 3.32. Dynamic range for the first two receiver front-end channels.

3.5.3. LO Divider. The LO signal is divided into 4 equal parts to drive the mixers in the four receiver channels. The front-end mixers require an LO power of +13 dBm. Taking the gain of the power amplifier and the loss of the board into account, the signal power at the input of the power amplifier should be larger than 0 dBm. A 1 to 4 power divider (Figure 3.33), utilizing a modified design of Wilkinson dividers [54] suitable for high microwave frequencies, were used to build the LO divider. This particular Wilkinson design was found to be suitable for high frequencies since it provides room for placing the required and very small (0201) surface mount 100 Ω resistor without sacrificing isolation. This divider was designed to operate at 24 GHz and its functionality was simulated using CST-MWS. The simulation results showed an insertion loss of -3.5 dB (0.5 dB beyond the ideal response) and a return loss better than 15 dB. Figure 3.34 shows the measured return loss and insertion loss of this particular 1 to 4 divider design. The best performance was obtained around 23.5 GHz with acceptable performance at 24 GHz. At 24 GHz the insertion loss is better than 10 dB at the input and 15 dB or better at the output ports. The insertion loss of this divider is between 9 to 10 dB (maximum of 3 dB beyond the simulated response). This additional loss is attributed to the dielectric losses and radiation losses which were found to be substantial at the connector microstrip point of contact. This divider is used for the LO port where frequency, amplitude, and phase of the signal are fixed. In other words, slight reflections at the ports are acceptable and do not affect the overall performance of the system. Furthermore, the output power of the LO source is also sufficient so that these additional losses do not adversely affect the overall system characteristics.

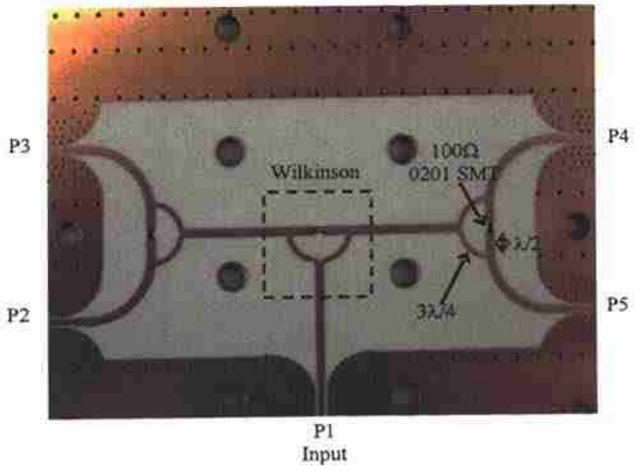

Figure 3.33. LO divider board.

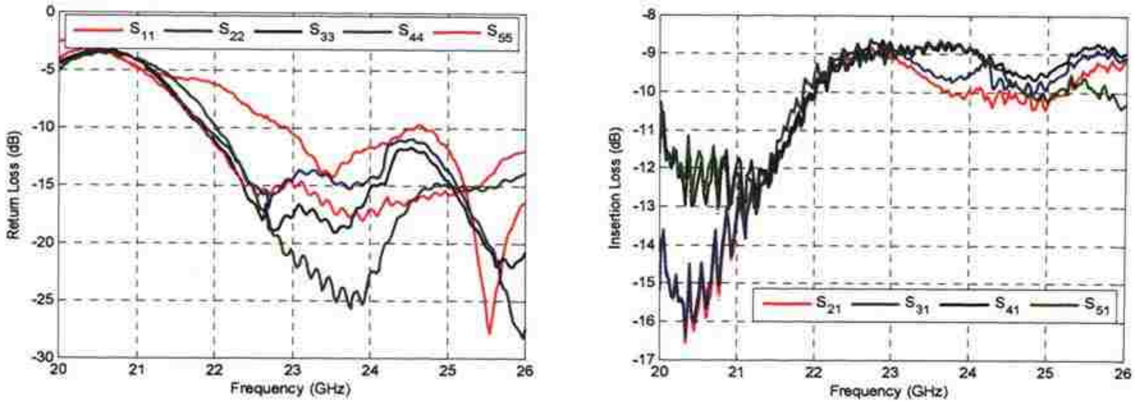

(a) (b)

Figure 3.34. LO divider test results: (a) Return loss, and (b) insertion loss.

3.5.4. IQ Demodulator. The final stage of the receiver is the IQ demodulator. Since the camera has four measurement ports, and there are four receivers, logically four IQ demodulators are required. The IQ demodulator board was based on Analog Devices' AD8339 chip which is a quad IQ demodulator. Since this chip is configured to be driven by a low noise preamplifier with differential outputs, a quad LNA (AD8334) was used. Furthermore, mixer outputs are current-based, and thus current-to-voltage transimpedance amplifiers (AD8021) were used for each I or Q output before applying them to the analog to digital convertors. These transimpedance amplifiers were also fitted with RC low-pass filters with a cutoff frequency of ~30 KHz. Figure 3.35 shows a picture of the assembled 4-channel IQ demodulator.

One drawback of using this chip is the requirement of 4LO, i.e. the LO input frequency of the chip must be 4 times the frequency of the IF signal. Consequently, for the 10.7 MHz signal input to the IQ demodulator, the 4LO input will require a signal at 42.8 MHz. To generate the 4LO, a synthesizer is locked to the system reference clock. The 4LO generator was built using an integer synthesizer and a VCO. Figure 3.36 shows a picture of the 4LO generator board, and its output spectrum. The 4LO is phase-locked to the RF sources ensuring coherent detection. The output spectrum of the 4LO source shows a phase-noise of approximately −100 dBc at 10 KHz offset.

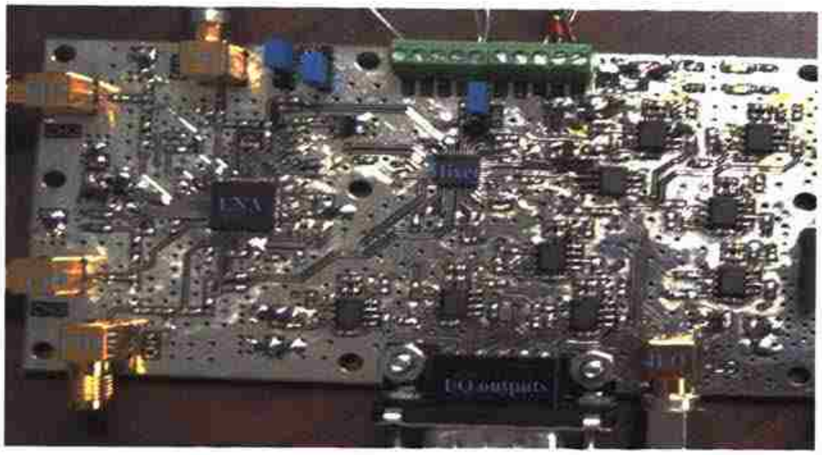

Figure 3.35. Picture of the 4-channel IQ demodulator.

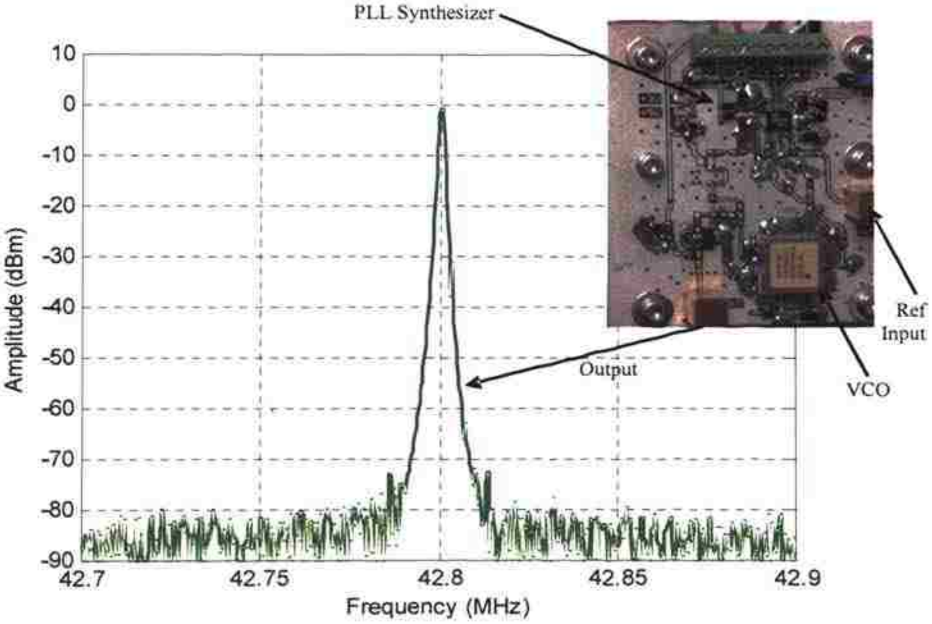

Figure 3.36. 4LO generator and the spectrum of its output (RBW = VBW = 1 KHz).

Figure 3.37 shows the setup used to test the performance of the 4-channel IQ demodulator. The IQ demodulator was tested at 10.7 MHz, which is the system IF frequency. Two Stanford Research generators were phase-locked, the first was set at a frequency of 10.7 MHz and its phase was swept from 0 to 360 degrees using the GPIB control command. The second generator was set to the 4LO frequency of 42.8 MHz. Using a variable attenuator, the signal power level was changed from -10 dBm (just below the saturation level) to -120 dBm. Figure 3.38 shows the dynamic range of the IQ demodulator, which shows a fairly linear response for a range of 90 dB. Figure 3.39 shows the phase estimation error for this IQ demodulator at various power levels. The average error in the detected phase of the signal was less than 0.3 degrees for signal power as low as -60 dBm. Overall, the performance of this IQ demodulator chip is unsurpassed by any commercial analog IQ demodulator in market today.

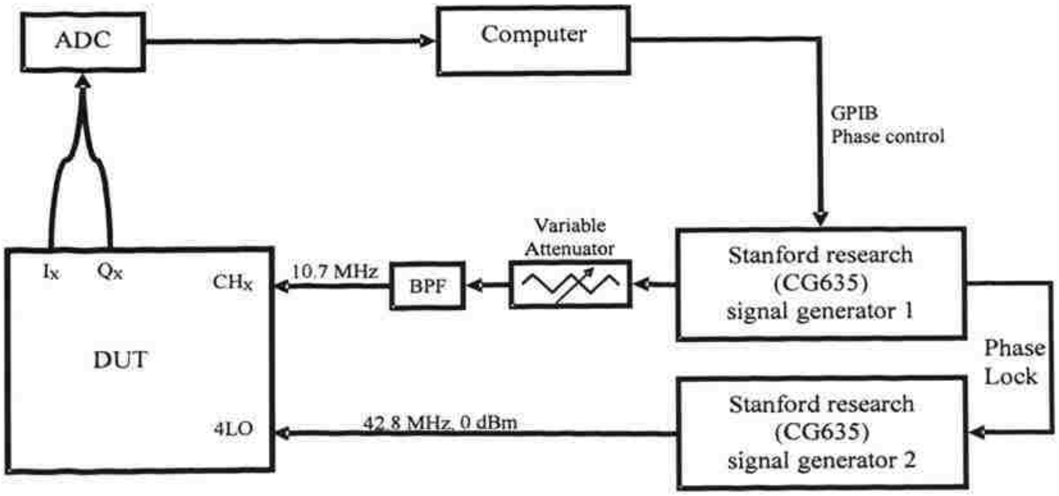

Figure 3.37. Setup for testing the 4-channel IQ demodulator.

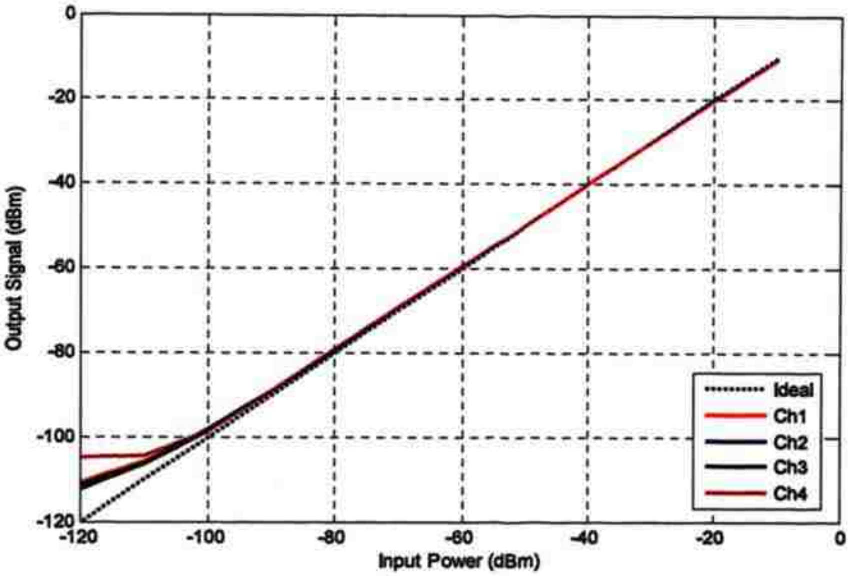

Figure 3.38. Dynamic range of the 4-channel IQ demodulator.

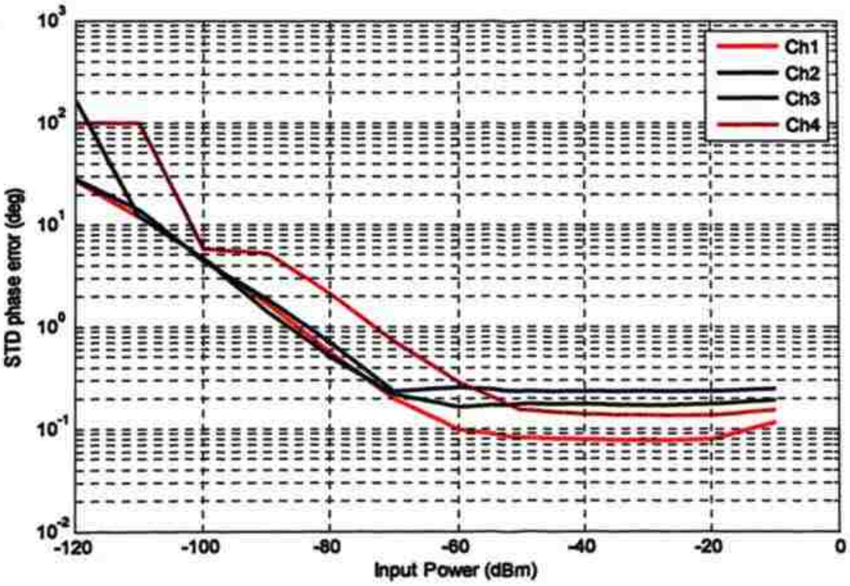

Figure 3.39. Phase error in the 4-channel IQ demodulator.

3.6. RETINA CONTROL & MODULATION CIRCUITRY

An off the shelf solution was used to control, or electronically scan, and modulate the retina. The off the shelf unit is the *Quicgate* controller from Dallas Logic™ based on Altera™ *Cyclone-II* FPGA shown in Figure 3.40. An FPGA solution gives the flexibility of easily changing the operation mode of the camera. Moreover, it is compact and cost-effective. This controller provides for 110 digital input/output lines, sufficient to address the retina's row and columns and the two switched combiners, while leaving few spare lines. The controller electronically scans the retina, while providing the modulation signal from its crystal oscillator. Furthermore, the reference signal needed to lock the RF sources and the 4LO source are provided from this controller. The controller also provides a synchronization signal to the ADCs that provides the clocks the data acquisition.

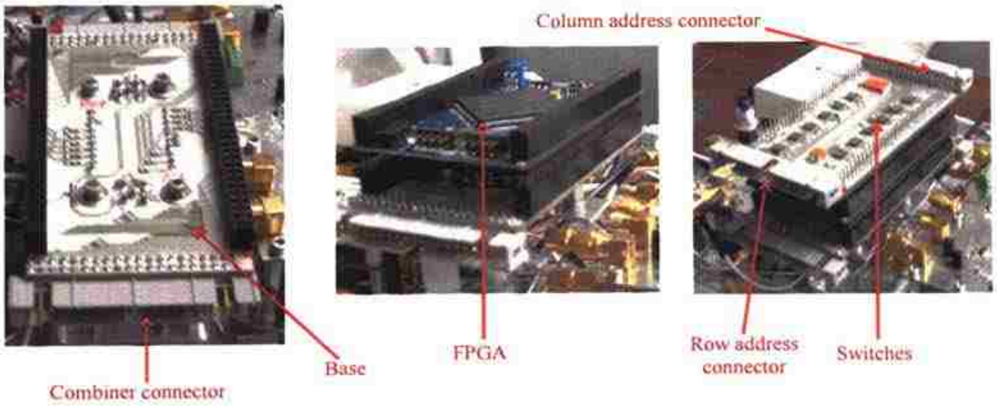

Figure 3.40. FPGA controller stack-up.

The combiner PIN diodes were driven directly by the controller, since each PIN diode draws maximum of 8 mA which is can be provided by the FPGA. On the other hand, the row and column lines of the retina can draw as much as 200 mA each. Therefore, a switching circuit was built to provide this high current directly from a power

4. SYSTEM TEST & CHARACTERISTICS

In the previous section, detailed design of various components of the camera were presented. Each component of this system was individually optimized to meet or exceed the design specifications. Figure 4.1 shows pictures of the front and back of the assembled camera. This system is compact, lightweight, and possibly handheld. This section provides a thorough investigation and analyses of the electrical characteristics of this system, sources of errors and their impact on the overall system performance and characteristics, and finally signal correction and characterization methods. Investigations are performed and the results are analyzed on: system noise level, isolation among the array elements, system range (i.e., distance of operation), slot mutual coupling, and array response.

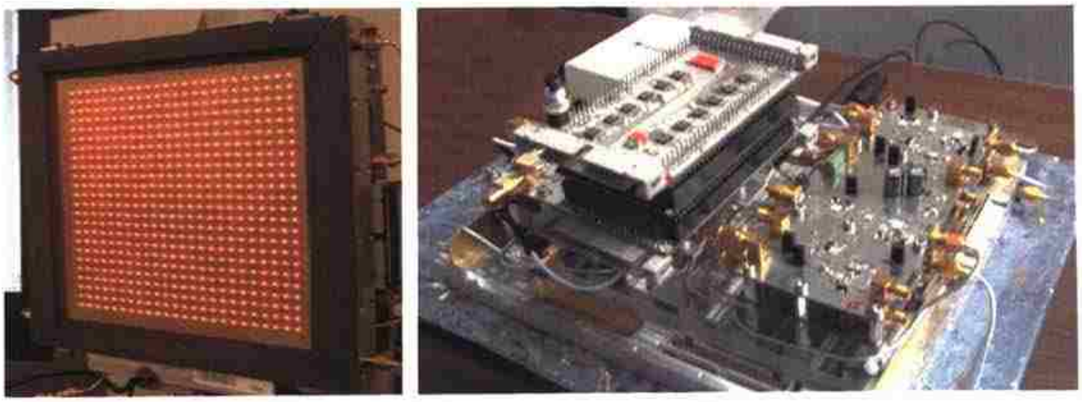

Figure 4.1. Pictures of the front and back of the camera showing the array at the front and the various RF and control components at the back.

4.1. RECEIVER PERFORMANCE

The receiver design presented in the previous section is based on a heterodyne scheme, in which the first harmonic of a single sideband of the modulated signal is demodulated and analyzed. Figure 4.2 shows the received spectrum, at port 4 (bottom left corner) of the retina, due the modulating slot located at row 12 and column 12, respectively. The irradiating source was an open-ended rectangular waveguide radiating towards the retina from a distance of 150 mm. The modulation frequency was 500 KHz. The spectrum shows the upper and lower sidebands (USB and LSB) of the modulated signal, respectively along with the carrier signal. This modulated signal contains even harmonics representative of a distorted square wave modulation. The distortion may be due to the limited bandwidth of the switching network, effect of switching high currents, or as a result of the non-linearity of the LEDs. Overall, the system only captures one of the first harmonics and all the other even and odd harmonics are filtered out. The carrier is more than 10 dB above the modulated signal rather than the 6 dB expected for a single slot. This extra power in the carrier is attributed to the leakage from the remaining slots in the retina. This leakage from various array slots can add-up constructively or destructively. Experiments showed that the power in the leakage depends on the electric field distribution on the retina and not the electric field on the specific slot being measured. However, the modulated part of the signal depends only on the field at the location of the slot being modulated.

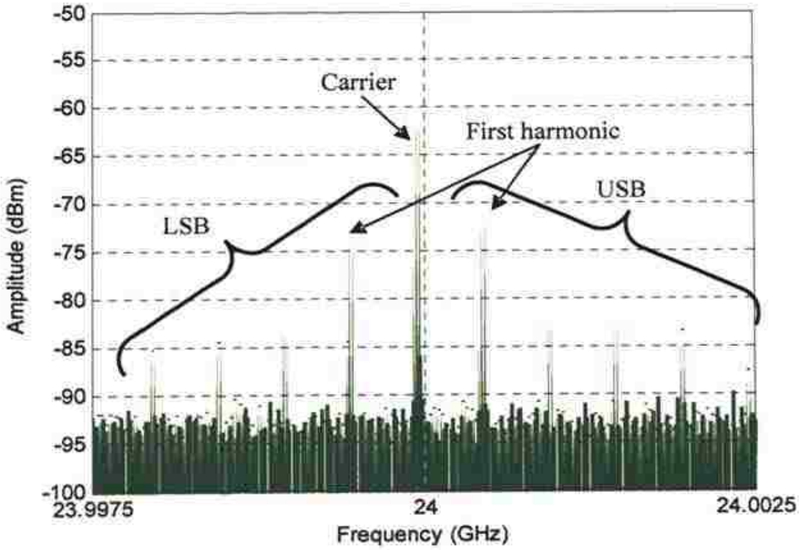

Figure 4.2. Measured signal at port 4 of the retina from to the modulating slot at row and column 12, respectively (RBW=1 KHz).

The receiver front-end down converts the signal from 24 GHz to the IF frequency range by mixing the signal with another signal at a frequency of (24 GHz + $f_{IF} \pm f_{mod}$) depending on which sideband is sought. Figure 4.3 shows the spectrum of the down-converted signal at the output of the mixer. In this figure, the LSB is mixed to the IF frequency of 10.7 MHz. The attenuation of the carrier and the USB is due to the effect of the IF filter, since the test port was not matched to 50 Ω and only used to verify the presence and the frequency spectrum of the signal. Figure 4.4 shows the spectrum of the signal at the output of the IF stage (e.g., the input to the IQ demodulator). At this stage, the sought sideband is passed through the filter and amplified. Subsequently, the carrier and the other sidebands and harmonics are attenuated by the filter. The stopband rejection for this IF filter is approximately 45 dB, which is clearly evident by the measured results shown in Figure 4.4. The contribution of these unwanted signals will be further reduced by match filtering at the IQ demodulator.

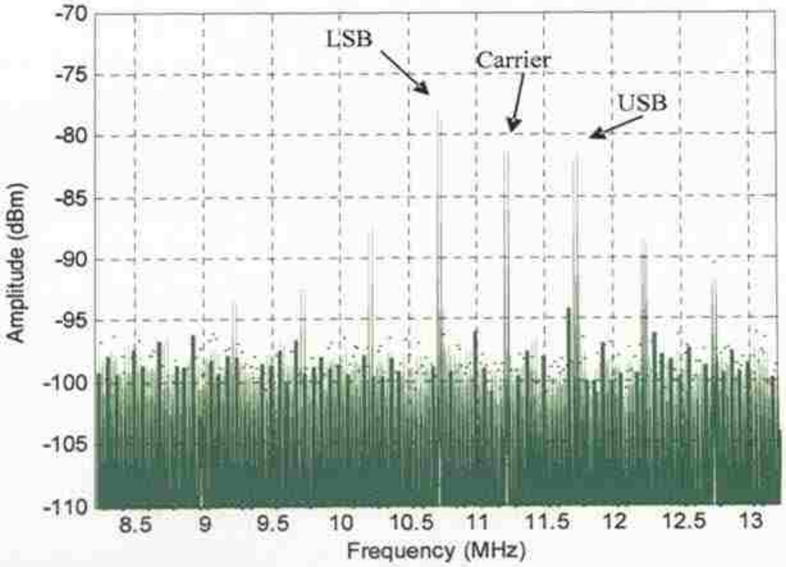

Figure 4.3. Signal at the mixer output of channel 4 due to middle slot modulating (RBW = 3 KHz).

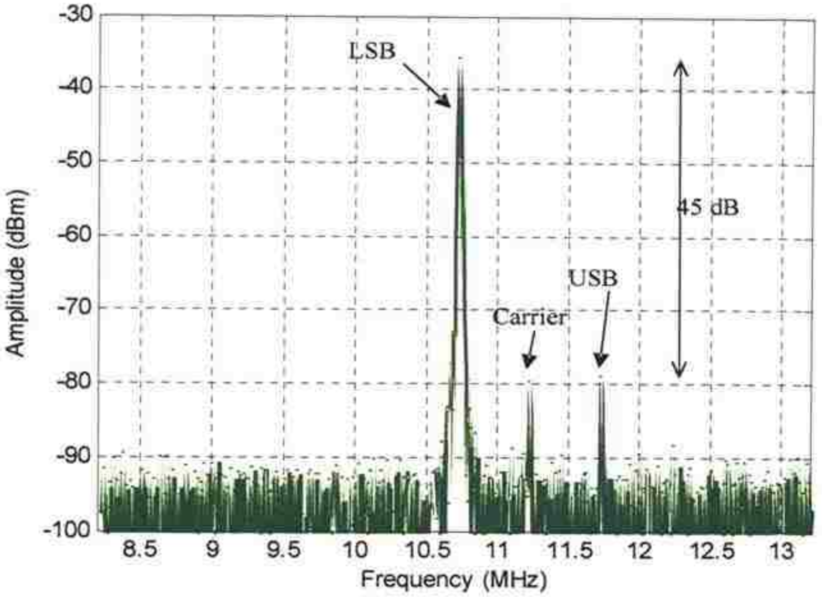

Figure 4.4. Signal at the IF output of channel 4 due to middle slot modulating (RBW=10 KHz).

4.2. MODULATION FREQUENCY

While there are constraints on the modulation frequency, there are also several optimization opportunities. Traditionally, the lock-in amplifiers are operated at the modulation frequency, which produces a direct correlation between the modulation frequency and the flicker (1/*f*) noise [34],[51]. In this design the lock-in amplifiers (i.e., the IQ demodulator) operate at the fixed IF frequency of 10.7 MHz. Therefore from the receiver point-of-view, the modulation frequency does not contribute to the performance of the receiver in the presence of flicker noise. On the other hand, the modulation frequency should be higher than the bandwidth of the IF filter such that the source leakage and other harmonics are filtered out. Furthermore, as shown in Figure 4.4 the IF filter attenuates the harmonics and leaked carrier in its stop-band. Subsequently, increasing the modulation frequency even higher gives the IQ demodulator (i.e., the matched filter) a better chance of rejecting these unwanted signals.

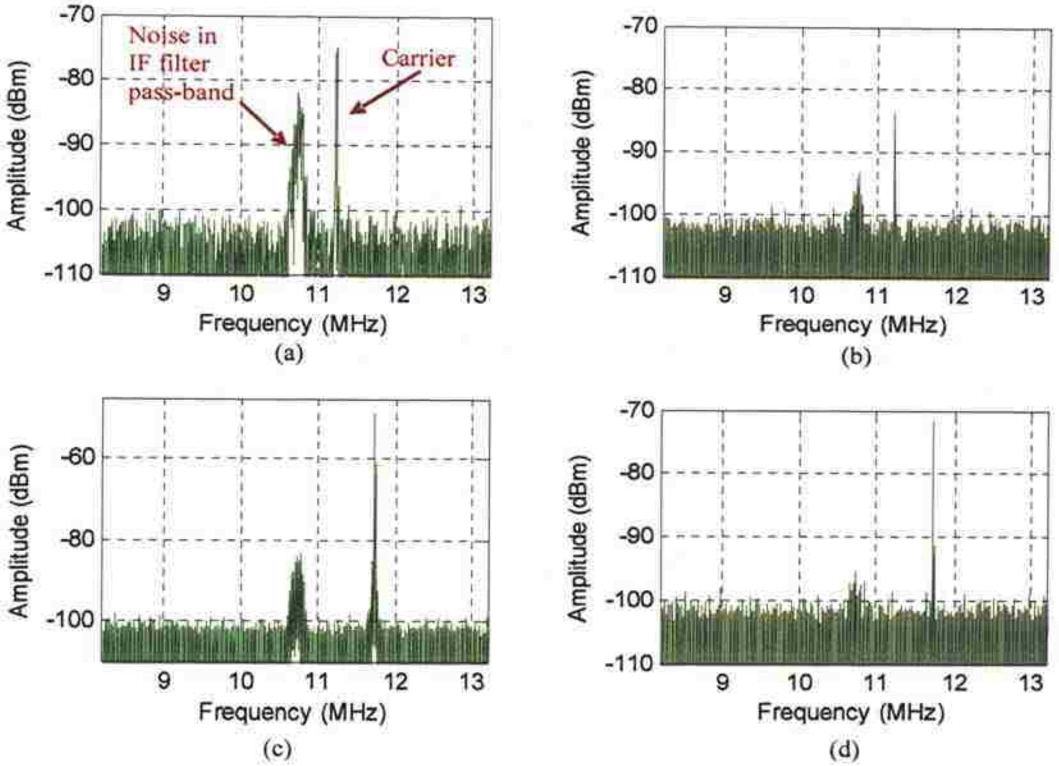

Figure 4.5. Effect of leaked carrier on the IF filter pass-band noise level (RBW= 1 KHz): (a) strong carrier f_{mod} = 500 KHz, (b) week carrier f_{mod} = 500 KHz, (c) strong carrier f_{mod} = 1 MHz, and (d) week carrier f_{mod} = 1 MHz.

is shown in Figure 4.6 where a modulated slot was used to modulate and pick up the signal transmitted by an irradiating open-ended rectangular waveguide. A precision variable attenuator was used to change the incident RF power on the slot. On the other hand precisely controlling the phase of the RF signal without affecting its magnitude is not an easy task. To change the phase of the RF signal the following property of modulated scattering was used. It is established that changing the phase of the modulating waveform changes the phase of the modulated RF signal [34]. With traditional receivers, this phase change may be lost if the signal is not decoded to extract a single sideband of the modulated waveform only. Typically, both sidebands are measured and to extract a single sideband from those measurements, extra processing steps are required [34]. As explained earlier, with the current design of the receiver only a single sideband is measured. Therefore the measured phase is directly correlated to the phases of the RF and modulated signals combined. Since in this experiment the phase of the incident RF signal is constant, the receiver phase sensitivity may be measured directly by changing the phase of the modulating waveform. In this experiment two phase locked signal generators were used. One signal generator provides the 20 MHz reference clock for the sources on the camera (replacing the reference crystal) and the other is used to modulate the receiving slot at 1 MHz. The phase of this modulating signal is changed over one cycle for each incident power setting. The computer controls phase setting and the data acquisition.

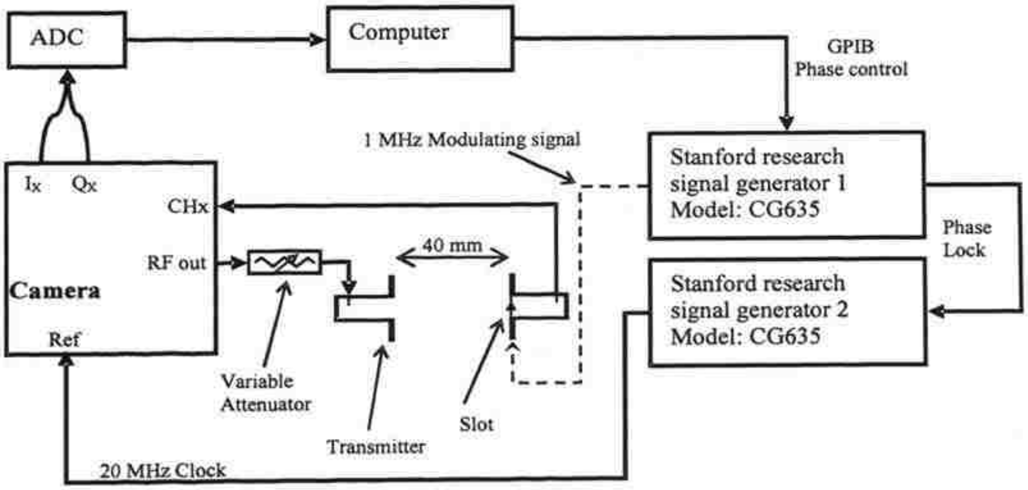

Figure 4.6. Experimental setup for testing receiver dynamic range.

The test results for this experiment are shown in Figure 4.7 and Figure 4.8 illustrating the receiver dynamic range and the accuracy by which phase is measured, respectively. Figure 4.7 shows the dynamic range of the receiver, indicating a linear response in a range of approximately 70 dB. The receiver saturates on an input power level of -35 dBm. The saturation is due to the high IF stage gain, which saturates the IQ demodulator. Figure 4.7 shows the corrected signal output power after compensating for this IF gain and ADC gain. When analyzing this dynamic range these corrections must be taken into account. For example looking at the noise in Figure 4.5, a maximum noise level of -80 dBm in the IF is translated (i.e., subtracting a 35 dB front-end and IF gain) to -115 dBm RF signal level which is the floor of the receiver dynamic range.

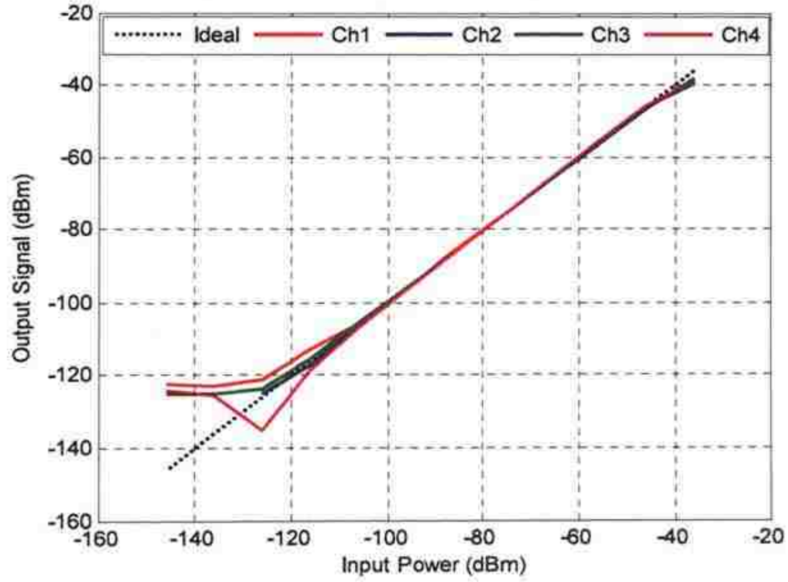

Figure 4.7. Dynamic range of the receiver.

Figure 4.8 shows that the accuracy associated with measuring phase for this receiver is below 10 degrees error at the low end of its dynamic range and it is approximately 1 degree at the high end (i.e., ~50 dB) of the receiver dynamic range. This phase error seems large compared to the test performed on the IQ demodulator separately which yielded phase errors on the order of 0.1 degree. This large phase error may be due to the low phase accuracy provided by the Stanford CG635 sources. These sources guarantee a phase error of less than one degree for frequencies higher than 200 MHz and it degrades by a factor of ten each decade below 200 MHz [55]. When testing the IQ demodulator, the Stanford sources were producing a 10.7 MHz signal, while in this test the modulation frequency was set to 1 MHz. Therefore, it was not expected that the Stanford test sources will maintain accurate phase setting. Overall, this receiver was optimized for when the retina captures scattered signals with corresponding relatively low powers. The saturation level of -35 dBm is acceptable since the retina is expected to measure small signals from far transmitters or scattering from week objects.

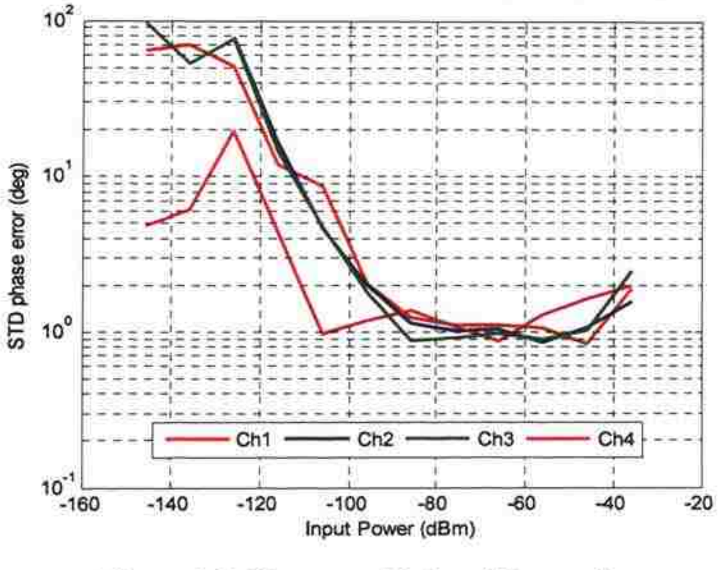

Figure 4.8. Phase sensitivity of the receiver.

4.4. ADDRESSING NETWORK PERFORMANCE

An issue of great importance in the design of the modulation addressing network is the ability to modulate one slot in a row/column while keeping the rest of the slots in

isolation problem. As shown in Figure 4.10 if the role of the red and green LEDs is reversed, the modulation isolation is improved. In this case, the modulation signal is passed through the row address lines (green LEDs) and the control signal is passed through the column address lines (red LEDs). Since the red LED presents lower impedance to the DC current, it takes priority in saturating the PIN diode especially at lower bias voltages where the retina is expected to be normally operating.

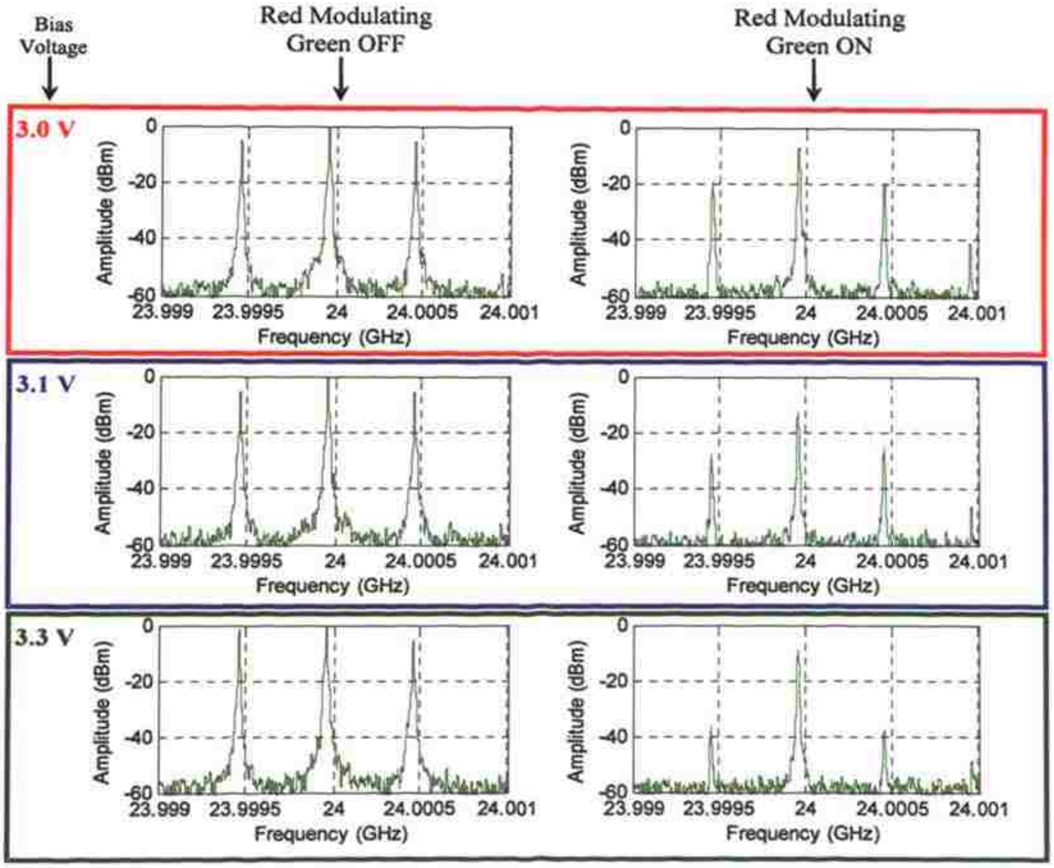

Figure 4.9. Modulation isolation for various bias voltage: modulating signal through the Red LED and control signal through Green LED.

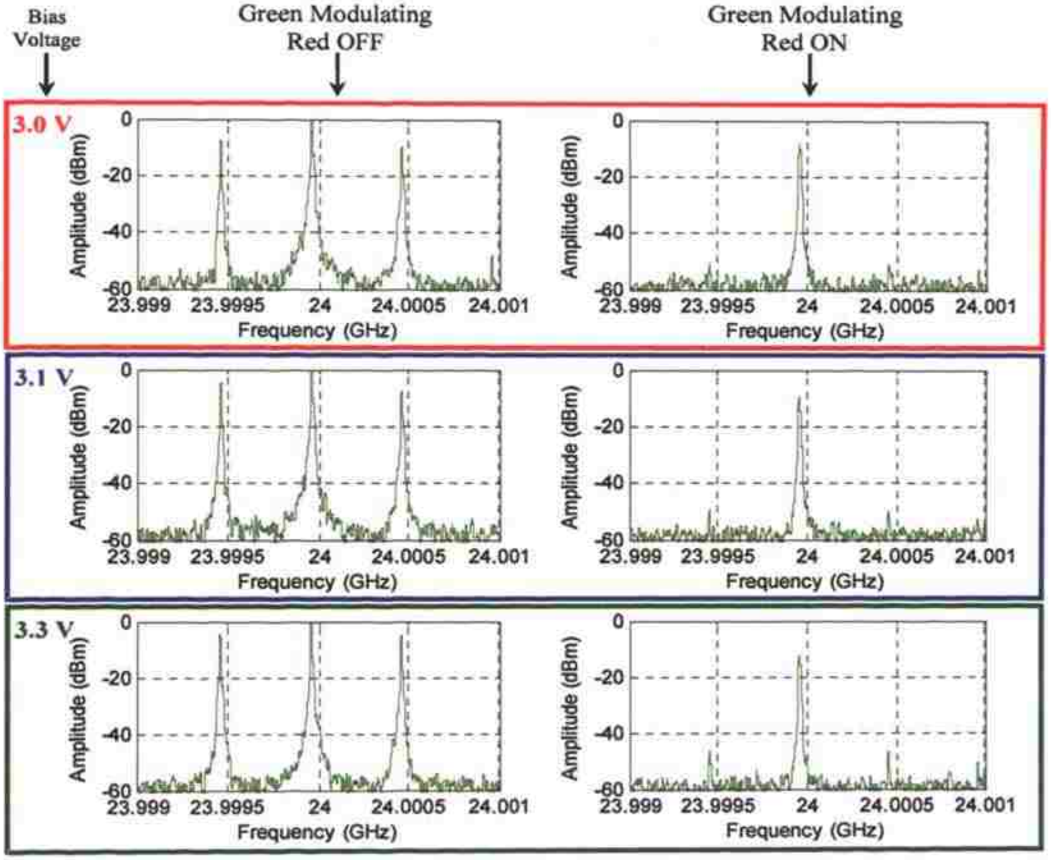

Figure 4.10. Modulation isolation for various bias voltage: modulating signal through the Green LED and control signal through Red LED.

Figure 4.11 shows the effect of this leakage on the measurements performed with the retina. A K-band open-ended rectangular waveguide antenna was used to illuminate the retina with a quasi-plane wave. When modulating the middle slot on the retina either through column (Figure 4.11a) or row (Figure 4.11c) address lines, the measured power at the IF output is approximately -35 dBm. When that middle slot is closed, only the cumulative leaked modulated signal is measured. In the case of column modulation (Figure 4.11b) the leakage was only 15 dB lower than the intended signal, while in the case of row modulation (Figure 4.11d) this leakage was 50 dB lower. Overall, the switching network and modulation creates a spatial multiplexing technique and the leakage represents isolation in this multiplexing scheme. It is desirable to have as high of isolation as possible. On the other hand, it is difficult to design a compact array with very high isolation. Consequently a correction technique may be applied to correct for these unwanted contribution from untagged slots.

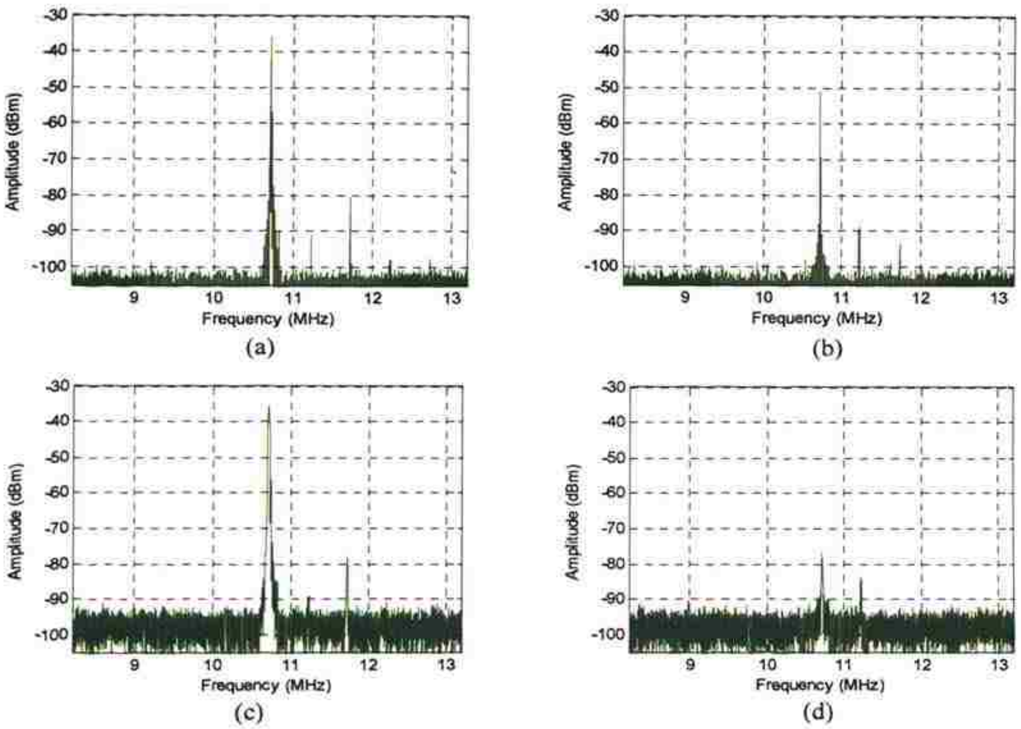

(a)

(b)

(c)

(d)

Figure 4.11. Signal and leakage measured at the output of IF when modulating a single slot in presence of plane-wave: (a) modulation on column; signal from middle slot, (b) modulation on column; cumulative leakage, (c) modulation on row; signal from middle slot, and (d) modulation on row; cumulative leakage.

4.5. RECEIVER DETECTION BANDWIDTH

The amount of noise affecting the measurement depends on the receiver detection bandwidth. As designed, the receiver has three filters. The first filter is the physical IF

digital convertors (ADC). For example using a sampling frequency of 2.5 MHz enables taking up to 125 samples per slot for averaging purposes.

Figure 4.12 shows the response of the three aforementioned filters, represented using Matlab filter visualization tool [56]. The IF filter is simulated using an order 3 Butterworth filter and the IQ filter is a first order (RC) Butterworth filter with a bandwidth of 30 KHz. The sampling frequency was assumed to be 2.5 MHz and an averaging length of 100 samples is used. The sampling frequency and number of samples satisfy a frame rate of 30 retina scans per second. This analysis helps in selecting the optimum filter. The effective cascaded filter shows a bandwidth of 10 KHz. Figure 4.13 shows the simulated group delay in these filters. The group delay in the cascaded filter is 30 μs.

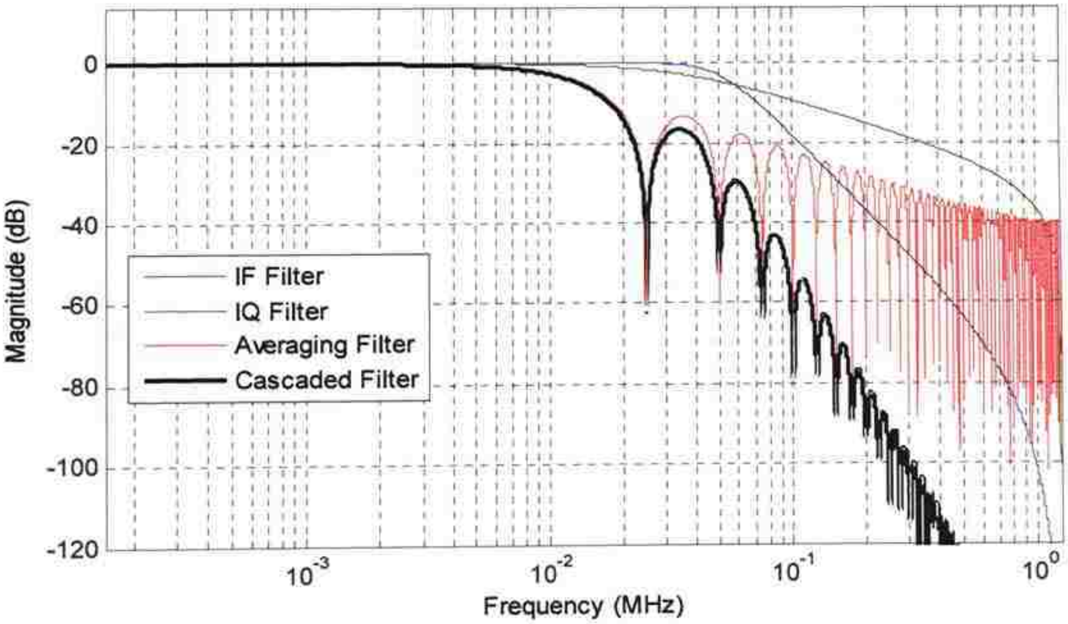

Figure 4.12. Magnitude response of the various detection filters in the system and their cascaded response.

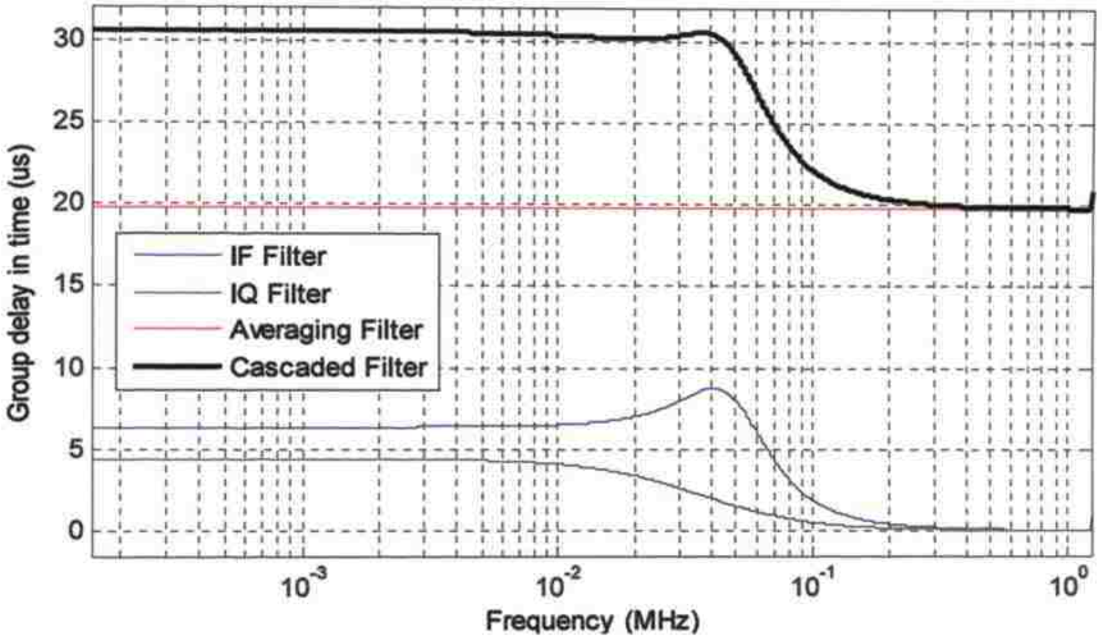

Figure 4.13. Group delay of the various detection filters in the system and their cascaded results.

4.6. CAMERA RANGE

The maximum range, R_{max}, of this camera can be obtained using the radar range equation,

$$R_{\max} \cong \left[\frac{P_t G_t G_r \lambda^2 \sigma}{(4\pi)^3 S_{\min}} \right]^{\frac{1}{4}} \tag{4.4}$$

where P_t is the transmitted power, G_t is the gain of the transmitter antenna, G_r is the gain of the receiver antenna (retina), λ is the wavelength, σ is the radar cross section of the target, and S_{min} is the minimum detectable signal [57]. The minimum signal detectable (S_{min}) can be written as,

$$S_{\min} = (SNR)_{\min} (NF) kT_0 B \tag{4.5}$$

Furthermore, this maximum range was found assuming an ideal array with no mutual coupling, loss, etc.

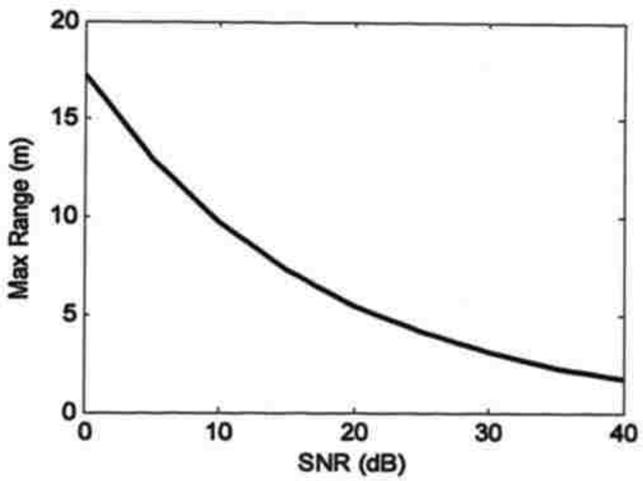

Figure 4.14. Camera maximum range in free space plotted vs. SNR.

4.7. SOURCES OF ERROR

4.7.1. Slot Mutual Coupling. One of the advantages of using these modulated resonant elliptical slots for imaging arrays is the low mutual coupling they introduce when placed in an array [38]. A study on similar slots [43] showed that the mutual coupling between each two slots was at the level of approximately -16 dB at a distance of $\lambda/2$. Figure 4.15 shows the configurations used for simulating the mutual effect for two adjacent slots in the retina. Coupling was considered in the E-plane, where the slots are placed in the collinear configuration and in the H-plane where the slots are placed side-by-side. The slots were considered on a two layer PCB with Rogers4350 substrate as explained earlier. For the simulations, each slot was fed by the modified rectangular waveguide (a = 7.7 mm and b = 4.3 mm), as described in the previous section. The aperture of slots (top layer of PCB) was at z = 0, and the structure was extended to infinity in the x- and y-directions. Various factors were anticipated to affect the coupling between two slots such as the dielectric substrate, the state of the slots (open or closed), and the distance between the slots.

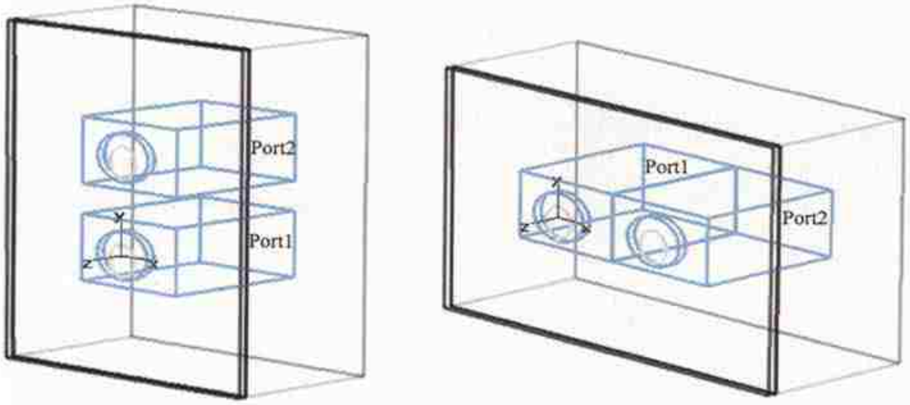

(a) (b)

Figure 4.15. Configuration for simulating mutual coupling between two slots; (a) E-plane (collinear), and (b) H-plane (side-by-side).

When the slots are isolated through the dielectric substrate – by placing a solid conducting ring around them, the surface current on the top conductor becomes the only mechanism of coupling between them. This source of coupling was investigated on similar slots in [43] for the case when both "aggressor" and "victim" slots were open. As mentioned previously, when a slot is idle it is considered to be in the closed state. Figure 4.16 shows the tangential magnetic field – which is proportional to the surface current density [60], at the aperture of the slots at $z = 0^+$ when port 1 is active. A First glance shows that the surface current extends more in the y-direction (E-plane) than the x-direction (H-plane) which will result in a stronger coupling in the E-plane than the H-plane. When both slots are open (i.e., the PIN diode is OFF), the active slots produce a current distribution in the victim slot as shown in Figure 4.16a and Figure 4.16b. Once again, this induced current is stronger in the E-plane than the H-plane. On the other hand when the victim slot is closed, the induced current on that slot becomes much smaller, as shown in Figure 4.16c and Figure 4.16d.

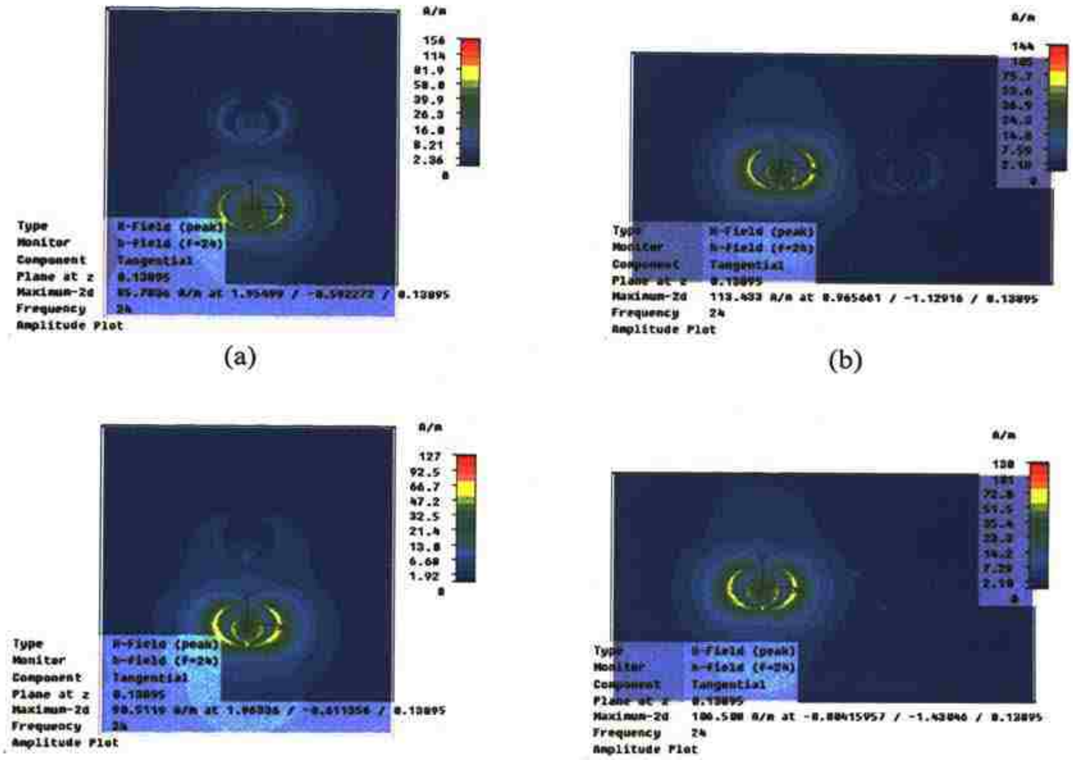

(a) (b)

(c) (d)

Figure 4.16. Tangential magnetic field ($\propto$ surface current density) at $z = 0^{+}$ for the case of only port 1 active, (a) E-plane – both slots open, (b) H-plane – both slots open, (c) E-plane – aggressor slots open and victim slot closed, and (d) H-plane – aggressor slots open and victim slot closed.

Another mechanism of possible coupling is propagation through the dielectric substrate of the PCB. The via-ring around the slot, introduced in the previous sections, confines the signal within the slot structure, which results in a better resonance when the slot is open, and better isolation (lower leakage) when the slot is closed. This via-ring also helps in lowering the mutual coupling between two slots. Figure 4.17 shows the tangential magnetic field on the back-side of the slot plane at $z = 0^-$ (inside the dielectric substrate). Without the via-ring to confine the fields in the slot area (Figure 4.17a and Figure 4.17b), the dielectric substrate acts as a low-loss propagation medium. These field mainly spread in the E-plane, with the field distribution stronger at the bottom of the slot (-*y*-direction) starting from the location of the PIN diode, unlike the field distribution at $z = 0^+$ where the distribution was symmetrical in the *y*-direction. By placing the via-ring, the coupling through the dielectric substrate is greatly reduced, as shown in Figure 4.17c and Figure 4.17d.

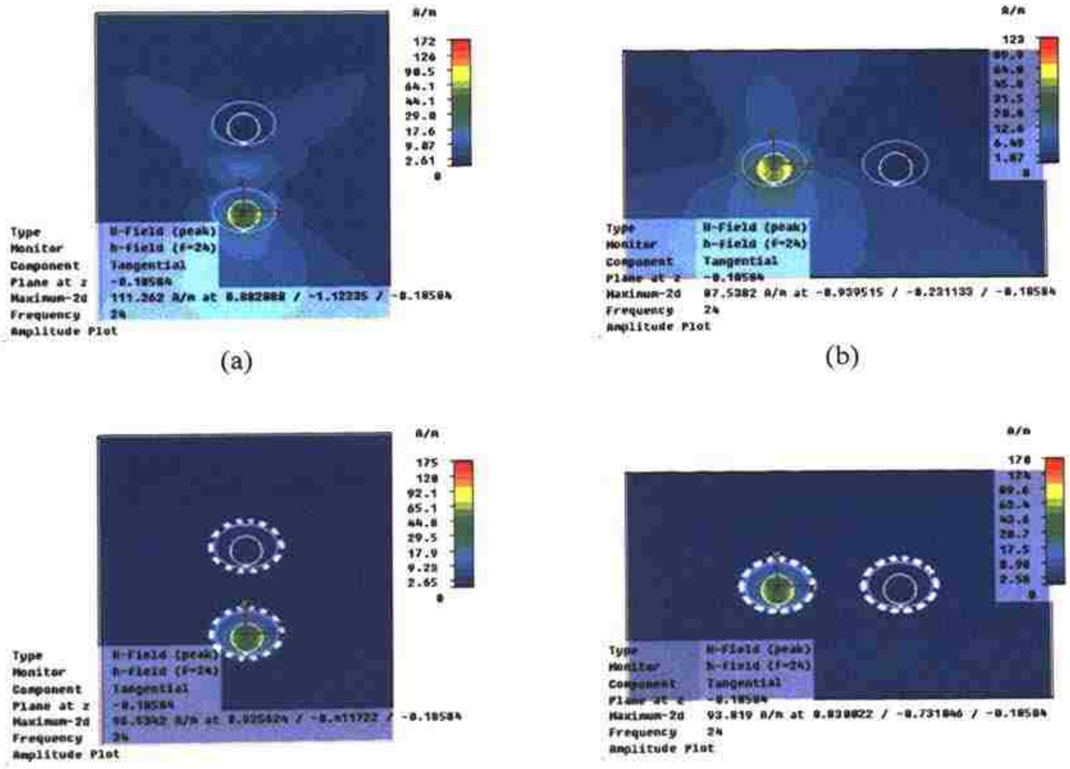

(a) (b)

(c) (d)

Figure 4.17. Tangential magnetic field (∝ surface current density) at $z = 0^-$ for the case of only port 1 active, aggressor slots open, and victim slot closed, (a) E-plane – without a via ring, (b) H-plane – without a via ring, (c) E-plane – with a via ring, and (d) H-plane – with a via ring.

phenomenon is attributed to the dielectric substrate acting as a low-loss bounded medium (transmission line) coupling two slots to each other efficiently. To summarize, mutual coupling between the slots in the retina as designed and operated, is smaller than -30 dB. This small level of mutual coupling is not expected to affect the electric field measurements using this type of slots.

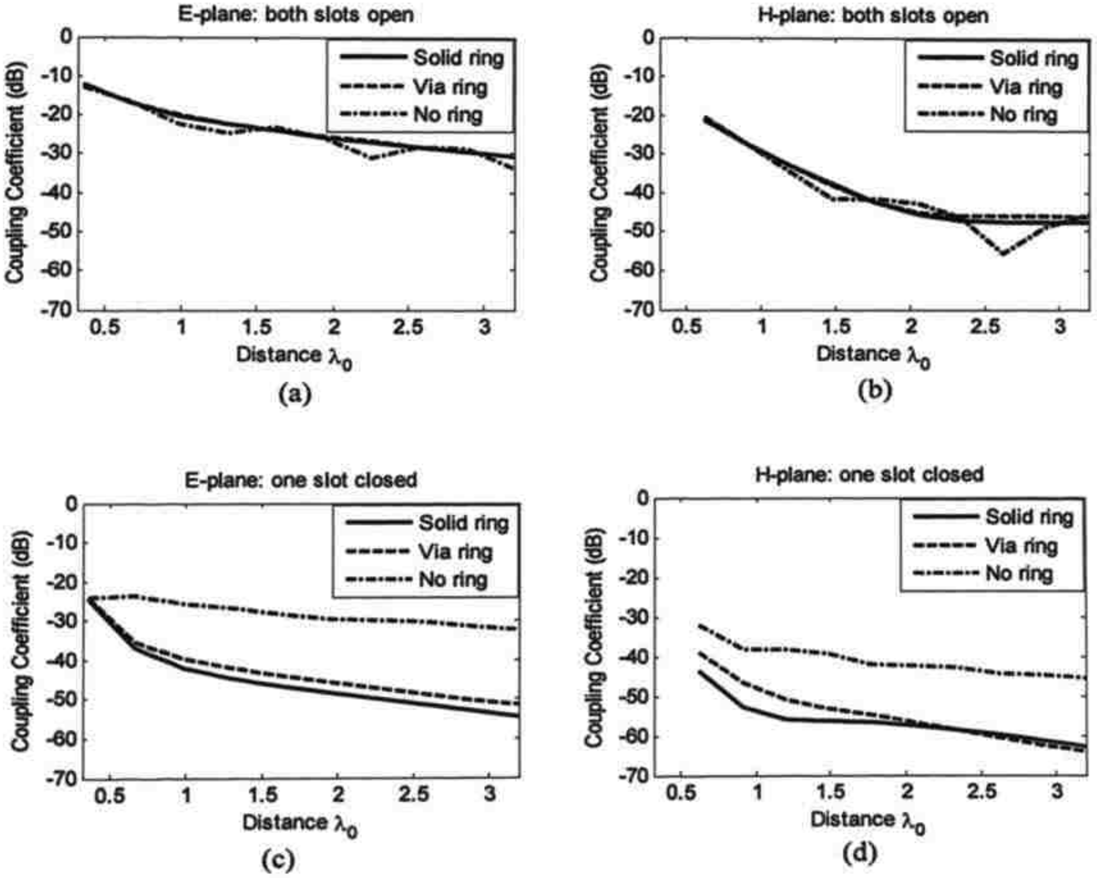

(a) (b) (c) (d)

Figure 4.18. E- and H-plane mutual coupling between two slots, (a) E-plane – both slots open, (b) H-plane – both slots open, (c) E-plane – aggressor slots open and victim slot closed, and (d) H-plane – aggressor slots open and victim slot closed.

4.7.2. Isolation in the Switching Scheme. As it was shown earlier, the slots exhibit a small leakage when closed. The premise of modulation is that these leakages will be non-modulated and will be filtered out. However, when a slot is modulating, any signal passing through that waveguide, including the leaked signal will be partially modulated. This effect is more prominent between the slots in the same collector waveguide. The following simulated experiment shows the effect of modulation on this leakage. The simulated setup is shown in Figure 4.19. Two slots are considered on the narrow wall of a waveguide. The slots are fed with a waveguide in order to provide for an isolated port on each slot (ports 1 and 2). Two other ports (ports 3 and 4) were placed on each end of the collector waveguide. For this simulation, the slot at port 2 was closed and the slot on port 1 was active (open or modulated). The *S*-parameters between the various ports were obtained and the isolation is computed. Isolation is defined as the ratio in power between the leaked signal through port 2 and the actual signal through port 1. Since there are two measurement ports (port 3 and port 4), two isolation coefficients are obtained. For the non-modulated case, the isolation is defined as

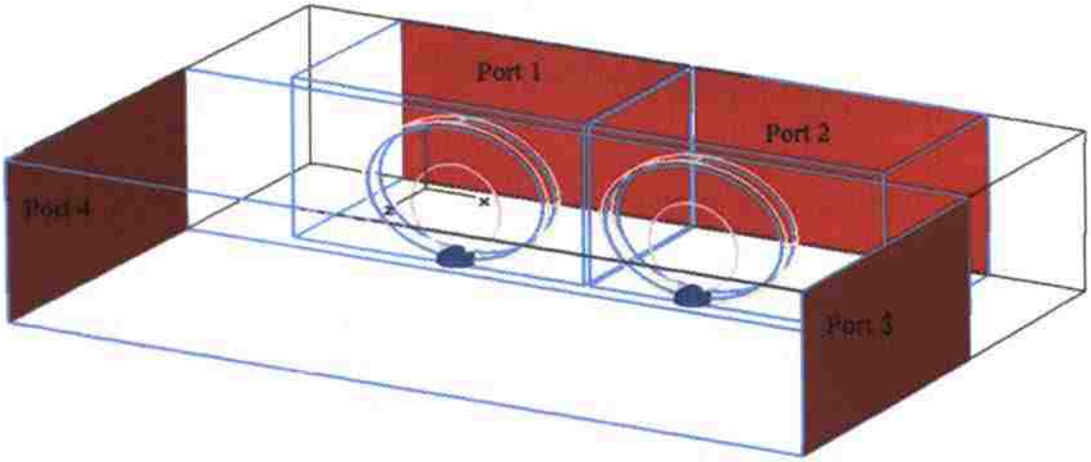

Figure 4.19. Simulation setup for obtaining the isolation in the multiplexing network.

$$I_j = 10\log\left(\frac{\left|S_{j2}\right|^2}{\left|S_{j1}\right|^2}\right) \tag{4.7}$$

where j =3,4 indicates the measurement port. For the modulated case, the isolation is redefined as

$$I_j = 10\log\left(\frac{\left|\Delta S_{j2}\right|^2}{\left|\Delta S_{j1}\right|^2}\right) \tag{4.8}$$

where $\left|\Delta S_{ji}\right|^2$ is the power in the modulated signal received at ports j = 3 or 4, due to a signal at ports i = 1 or 2.

The simulation is performed for various distances between the two slots. The results are shown in Figure 4.20. As shown in Figure 4.20, the un-modulated isolation in

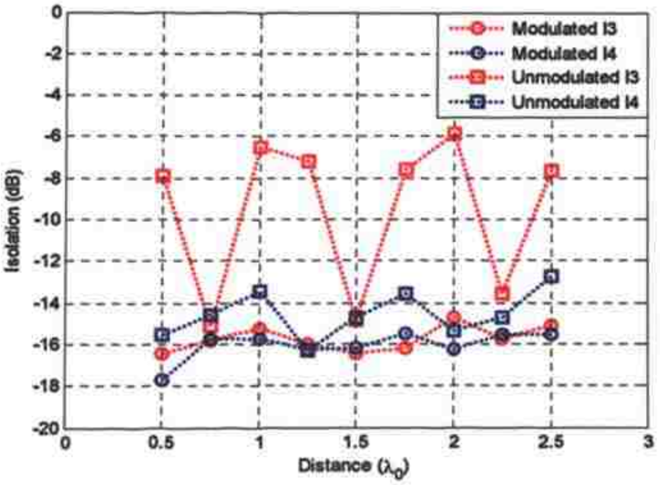

Figure 4.20. Un-modulated and modulated isolation in the multiplexing scheme.

a mechanical scanner over the array element, the response for all elements was obtained. Since the transmitted signal for each slot does not change, the variations in the measurements are due to characteristics of the retina only. By applying equation (4.9), the correction coefficients may be found, as shown in Figure 4.21. The transmitter was a resonant elliptical slot antenna. The sides of the slot antenna were covered by absorbing film to reduce multiple reflections between the retina and the transmitter. Furthermore, the characterization was made with several distances (one wavelength range) between the transmitter and the retina to average out the effect of any residual multiple reflections.

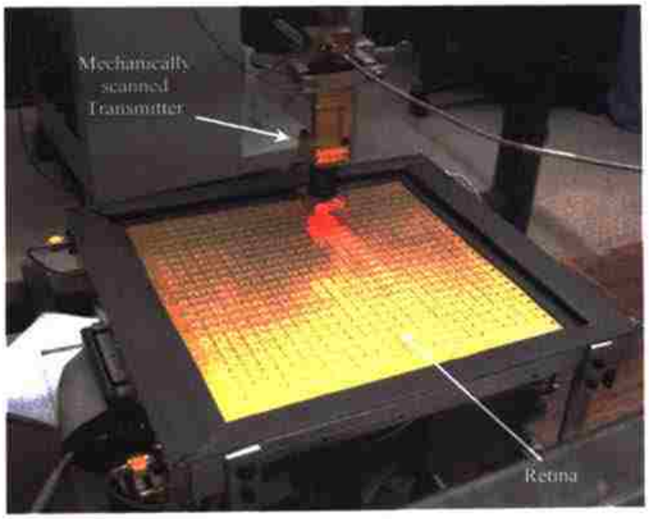

Figure 4.21. Picture showing the setup for characterizing the array using a mechanically scanned probe to provided localized excitation.

Figure 4.22 shows 2D maps of the normalized signal power measured at the four output ports of the retina. The process of mechanical scanning mimics a plan-wave excitation. These maps show the attenuation of the signal as it travels through the waveguide collectors and combiners towards the four output ports. They also show that when a port receives a highly attenuated version of a signal, there will be at least one other port that receives a strong version of that same signal.

Equation (4.10) can be rewritten as an optimum maximum ratio combiner (MRC) [62] where the weights are the complex conjugate of the array response coefficients γ^{p}_{ij} shown in Figure 4.22:

$$E^{m}_{ij} = \chi_{ij} E^{a}_{ij} = \sum_{p=1}^{4} \left(\gamma^{p}_{ij}\right)^{*} S^{p}_{ij} \tag{4.11}$$

where E^{m}_{ij} are the combined signals from all four measurement ports, and χ_{ij} are the

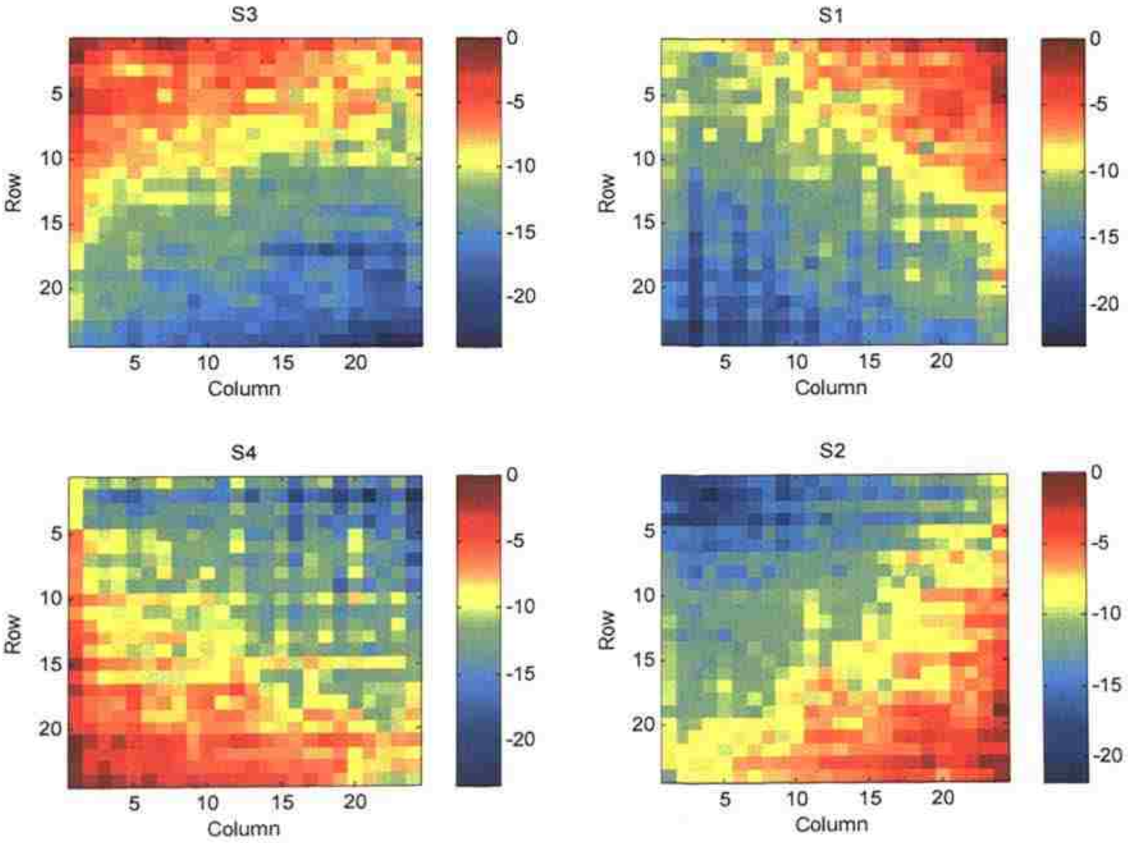

Figure 4.22. Normalized measured signal power (dB) for uniform localized excitation, measured at the four ports of the retina.

array correction coefficients. Furthermore, the array coefficients may all be phase referenced to a single port (e.g., port 1) yielding;

$$E_{ij}^{m} = \sum_{p=1}^{4} \alpha_{ij}^{p} S_{ij}^{p} e^{-j\left(\phi_{ij}^{p} - \phi_{ij}^{1}\right)}. \tag{4.12}$$

Equation (4.12) describes the signal combination as a weighted average after phase aligning all signals with port 1. When performing the characterization, multiple measurements are performed to average out the effect of multiple reflections. When changing the height of the transmitter, the amplitude changes slightly, however the phase can go through a full cycle. By referencing the phases to the phase at port 1, the difference becomes independent of the phase of the transmitted signal and only as a function of the array properties as shown in Figure 4.23 for element (i = 12, j = 12). A slight variation with a standard deviation of less than one degree is observed in these phase differences. These subtle variations may as well be due to multiple reflections between the transmitter and the retina.

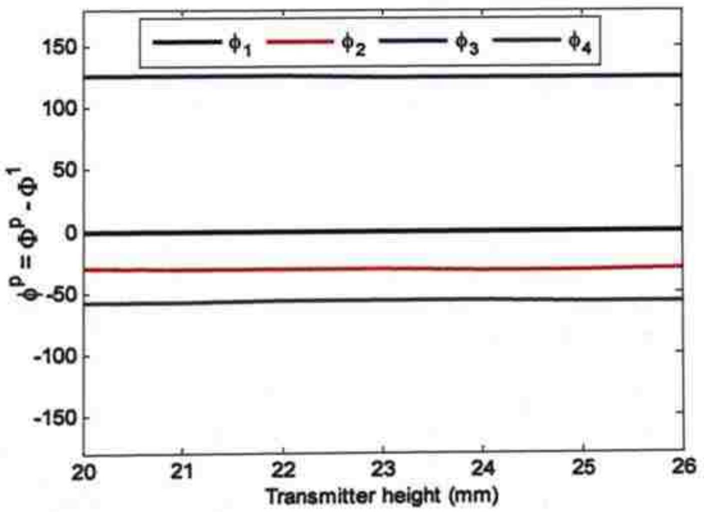

Figure 4.23. Referenced phases of the MRC coefficients for array element (i = 12, j = 12) as a function of the transmitter height.

After performing the MRC, the combined measurements E_{ij}^{m} are divided by χ_{ij} to correct for the residual array dispersion and find the actual incident electric field E_{ij}^{a}. The coefficients χ_{ij} are found using

$$\chi_{ij} = \frac{E_{ij}^{m}}{E_{ij}^{a}} \tag{4.13}$$

for a known incident electric field E_{ij}^{a}. The known electric field in the case of plane wave excitation or in the case of scanned localized excitation is $E_{ij}^{a} = 1$. Figure 4.24 shows the magnitude and phase distribution of χ. After combining the four measured signals, the residual array correction coefficients shows a smaller variation in amplitude, except for the elements on the array edges which are stronger in response than the majority in the middle of the array as expected since they go through the least amount of loss before reaching the nearest output port. The phase of correction coefficients shows a trend moving towards port 1, since all measurements were phase referenced to that port. The large variation in phase is expected because of the array interspacing and the large guide wavelength.

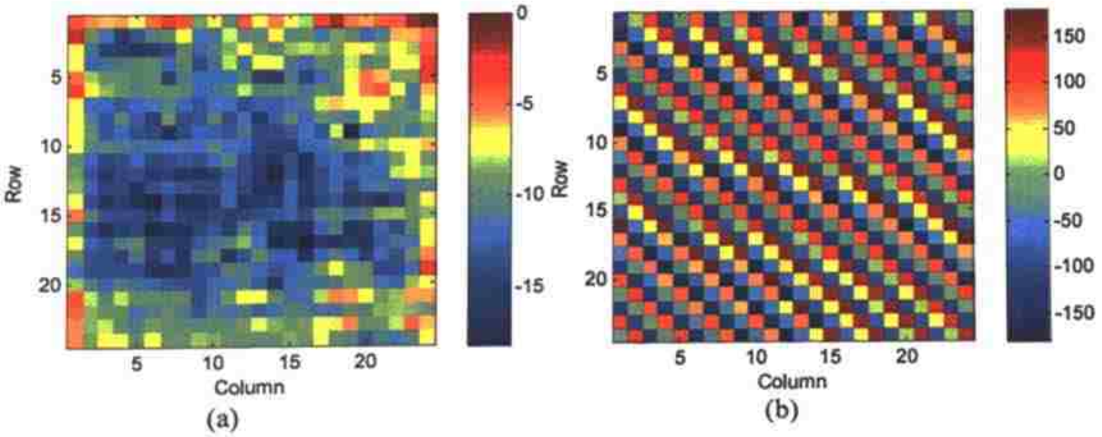

(a) (b)

Figure 4.24. (a) Magnitude and (b) phase distribution of the array correction coefficients χ obtained using the scanned localized excitation method.

Using a scanned transmitter to obtain the correction parameters is simple, yet upon testing the imaging system on known electric field distributions, errors as large as 3 dB in magnitude and up to 20 degrees in phase were noticed. These large errors were due to the inaccuracies in positioning the transmitter on top of the array elements while scanning. The scanner that was used to position and scan the transmitter was introducing a progressive positional error that resulted in as much as 3 mm position error towards the end of the array. This resulted in a skew in the phase of the array correction coefficients.

4.8.1.2 Plane wave excitation. Another viable method to characterize the imaging array is to illuminate it with a known electric field distribution. Typically a plane wave excitation is used since a plane wave has a constant magnitude and phase [61]. For this imaging array the far-field distance is more than 7 meters. In other words in order to produce a plane wave at its aperture, any simple and small transmitting antenna should be at least that far from the retina in an antenna test range. Not having this possibility, the second best solution was to use any other known electric field distribution. The schematic of the test setup is shown in Figure 4.25. The retina is placed in an anechoic chamber, with the transmitting antenna at a distance *h* providing the known illumination. The transmitter was an open-ended waveguide antenna. The radiated electric field by the waveguide can be found using equation (2.13) and the expressions in [2].

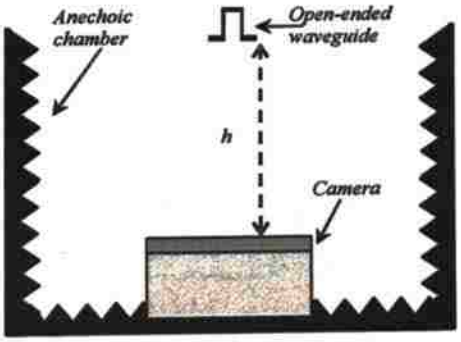

Figure 4.25. Schematic of the setup used for characterizing the imaging array.

The measurements were performed at various distances, h, covering a range of two wavelengths from 387 to 411 millimeters with steps of 2 mm. At these distances the magnitude variations over the aperture of the retina does not exceed 1 dB. On the other hand the phase variations go through a full cycle. Figure 4.26 shows an example of the incident electric field on the retina aperture from a distance of 410 mm obtained using the theoretical formulation.

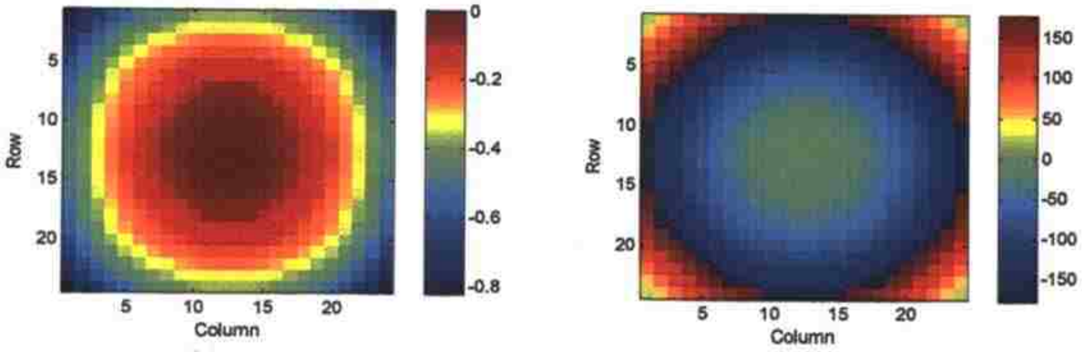

(a) (b)

Figure 4.26. Incident electric field (E^a) on the retina aperture at $h = 410$ mm, (a) magnitude (dB), and (b) phase (deg).

The combining coefficients, γ_{ij}^{p}, are obtained in a similar fashion as in the previous case of the scanned illuminator. The array dispersion correction coefficients, χ_{ij} (Figure 4.27), are obtained by dividing the combined measurements by the actual electrical field distribution. In the case of the scanned localized excitation, the actual electric field was considered to be unity since it does not change from one array element to the next similar to a true plane wave excitation. In this case the illumination is not a true plane wave. The illuminator pattern (E^a) similar to that of Figure 4.26 at various distances was found using the theoretical formulation for an open-ended waveguide [2]. The array correction coefficients, χ, shown here look similar to the previous case. The differences are subtle and the ultimate effect is noticed when measuring an electric field distribution.

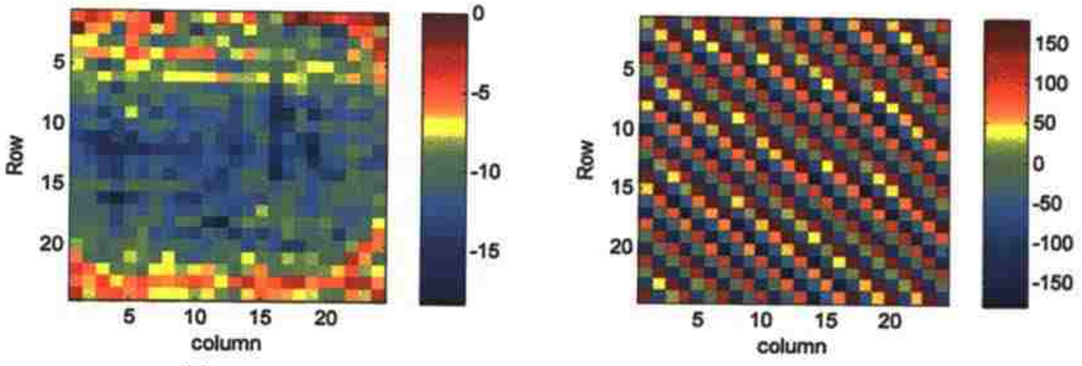

(a) (b)

Figure 4.27. (a) Magnitude and (b) phase distribution of the array correction coefficients χ obtained using a semi-plane wave illumination.

Figure 4.28 shows the corrected measurement vs. theoretical electric field distribution produced by an open-ended waveguide from a distance of 390 mm. This measurement was not part of the calibration set. The magnitude plot shows slight distortion. This distortion is very small and it is only noticed due to the small range in the actual field. The average absolute magnitude error in this measurement is ~0.025. The phase plot on the other hand shows a strong resemblance to the theoretical phase pattern. The absolute phase error was ~3.5 degrees. Overall, these accuracies are considered very high for such a high frequency system. Furthermore, for imaging applications and array processing techniques such as synthetic aperture techniques, the overall phase pattern is much more important than the absolute error. Section 5 of this dissertation provides other examples of measuring electric field distribution along with some imaging application.

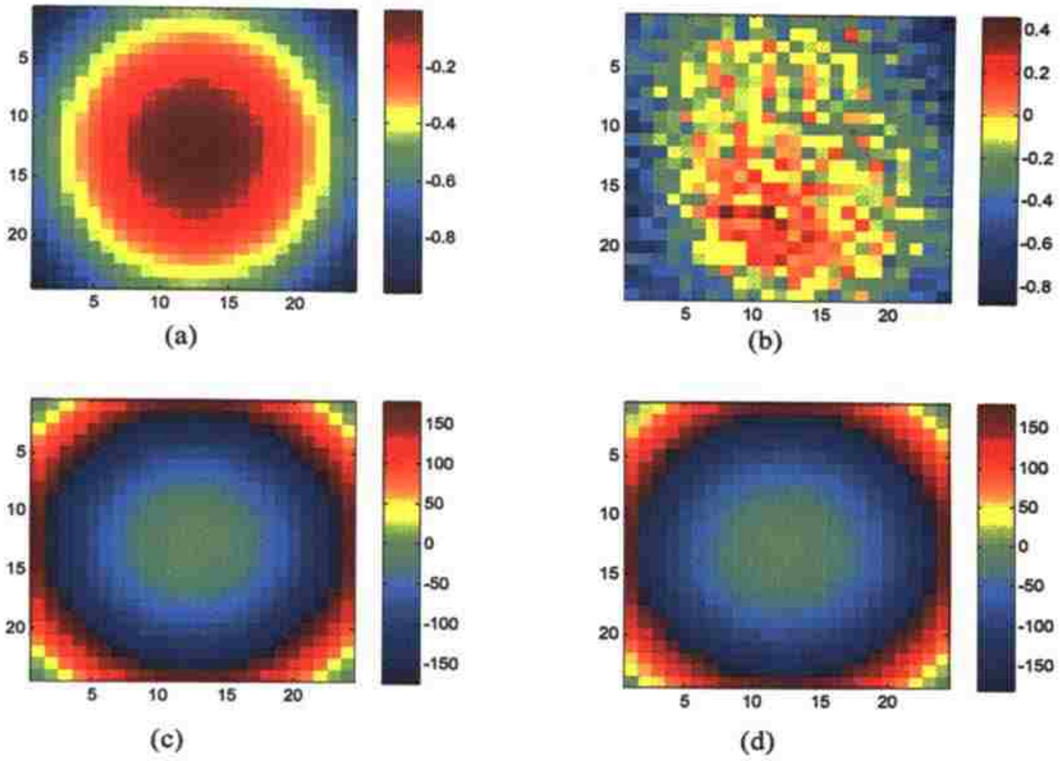

(a) (b) (c) (d)

Figure 4.28. Measured vs. theoretical electric field distribution produced by an open ended waveguide from a height of 390 mm, (a) theoretical magnitude (dB), (b) measured magnitude (dB), (c) theoretical phase (deg), (b) measured phase (deg).

4.8.2. Full Correction. A Complete error correction assumes that a signal received when tagging (modulating) a certain slot is a combination of the incident electric field on all slots. This assumption combines the effect of mutual coupling, isolation, and array dispersion into a set of error coefficients. The measured signal at each slot location is defined as,

$$S_i^p = \sum_{j=1}^{576} h_{ij}^p E_j \qquad (4.14)$$

5. APPLICATIONS

There are numerous potential applications for this microwave imaging system. Any application that requires 2D electric field mapping is a potential candidate. For example this imaging system can be used to rapidly map the electric field pattern of an antenna in its far-field. Figure 4.1 shows the system displaying the far-field pattern of a K-band open-ended rectangular waveguide (the two images on the left side). Another application is localizing a scatterer in a 2D space. This is achieved by utilizing the system as a 2D synthetic array producing a narrow scanning beam. Furthermore, by increasing the frequency bandwidth of the system it is possible to obtain some range resolution making this system a true 3D target localization device.

This system is more suitable for imaging applications, where the overall distribution of electric field (or pattern) is critical for forming an image of a scattering object. This system can be readily used in through transmission mode, where the object

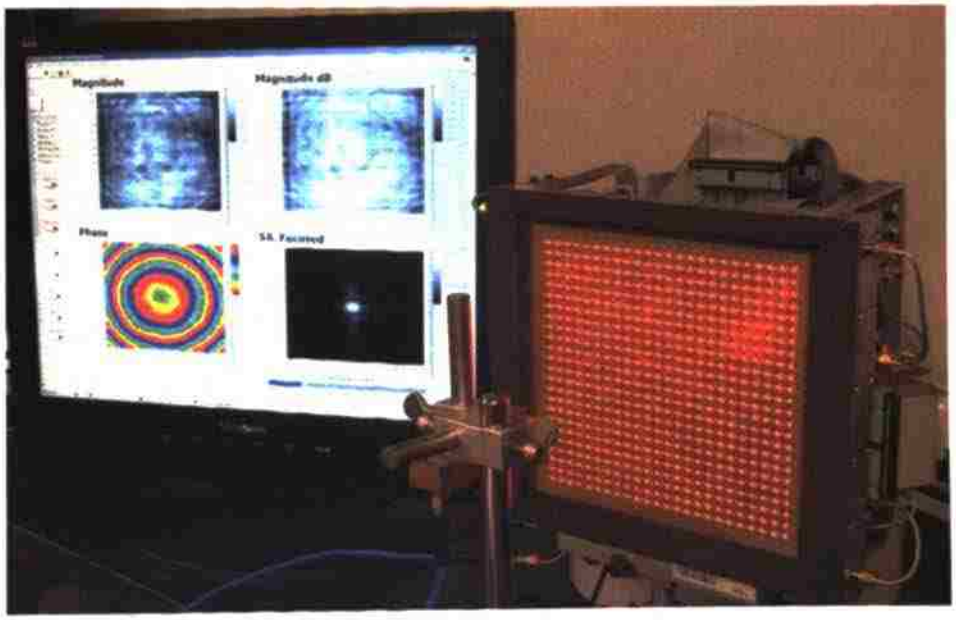

Figure 5.1. The Imaging system displaying electric field distribution of an open-ended waveguide.

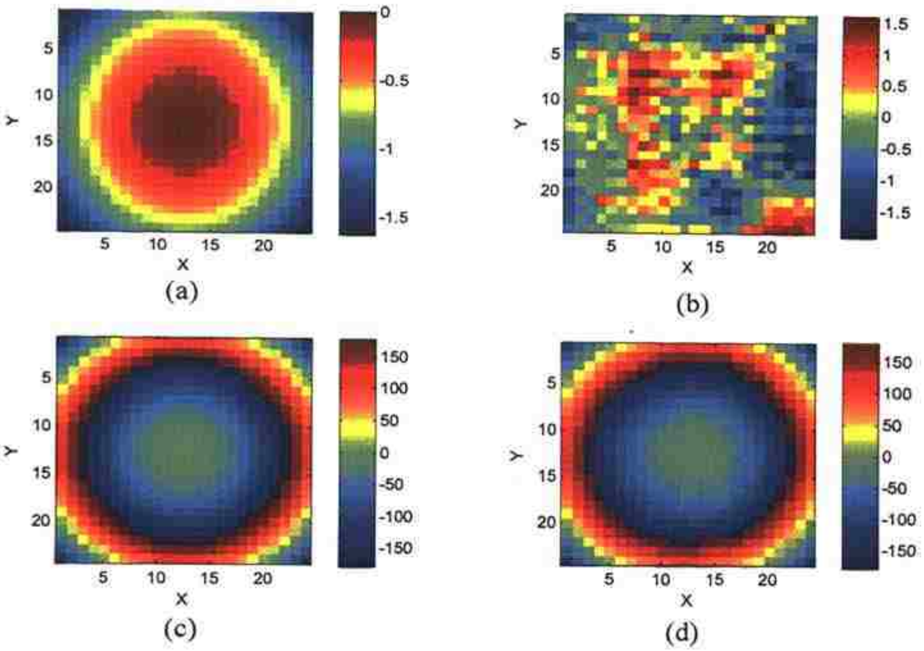

(a) (b)

(c) (d)

Figure 5.2. Measured vs. theoretical field pattern at 300 mm distance of a K-band open-ended waveguide aperture, (a) theoretical magnitude (dB), (b) measured magnitude (dB), (c) theoretical phase (deg), and (d) measured phase (deg).

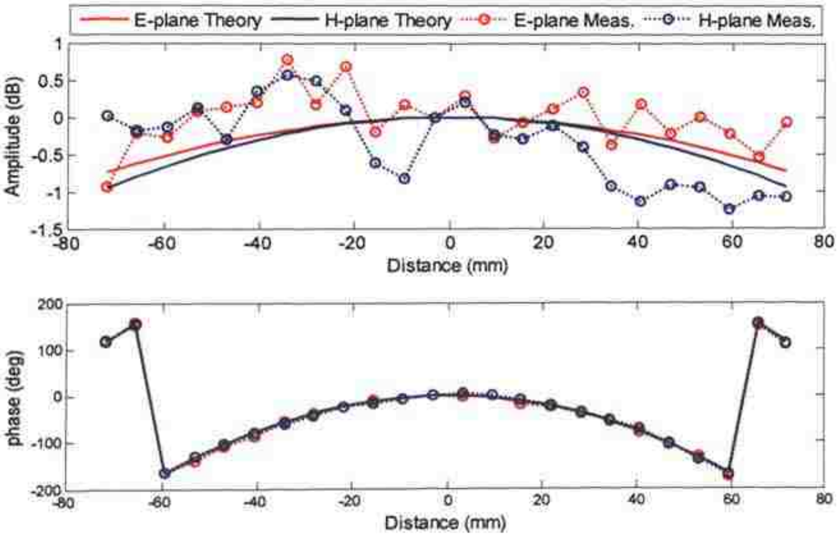

Figure 5.3. Measured vs. theoretical amplitude and phase of the E- and H-plane cuts of the field pattern at 300 mm distance from the K-band open-ended waveguide aperture.

Figure 5.4 shows the average amplitude and phase of the four middle slots vs. the distance between the waveguide and retina for the aforementioned set of measurement. The average magnitude and phase values from the four middle slots were taken due to the absence of a central slot (even number of rows and column), and the fact that from these distances the field pattern resembles that of a plane-wave in the relatively small area of these four slots. The magnitude measurement shows an RMSE of ~0.03 compared to the theoretical results, while phase shows a RMSE of ~13 degrees. These errors are quit acceptable for this experiment since the open-ended waveguide was positioned manually and the 13 degrees corresponds to less than 0.5 mm in position error at 24 GHz. For all practical purposes, this retina measures the electric field pattern accurately. Further improvements would require a better calibration of the retina that takes into account and corrects for the limited isolation in the waveguide network and the mutual coupling among the slots.

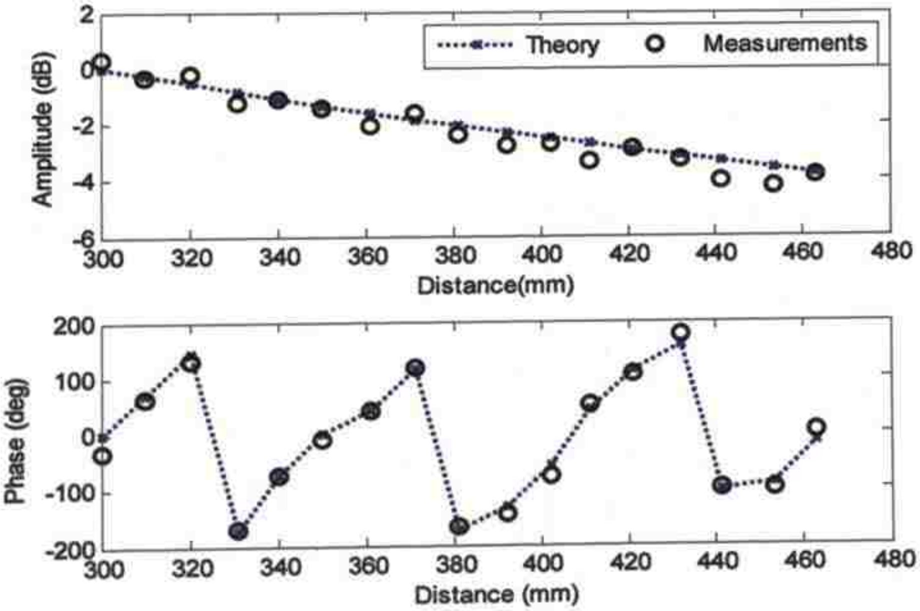

Figure 5.4. Measured and theoretical amplitude and phase of vs. distance from the K-band open-ended waveguide aperture.

5.2. TARGET LOCALIZATION

This imaging system with its relatively large array size of 12λ × 12λ can provide a sharp beam (~5 degrees beamwidth) which can be used to localize a radiating source or sctterring target within a 2D angular space. Furthermore, utilizing techniques such as synthetic aperture focusing (SAF) [5],[32] allows for localization of the target within the near-field of the array. For this array, the far-field distance ($\frac{2D^2}{\lambda}$) where D is the largest linear dimension of the array, corresponds to more than 7 meters. SAF, a technique derived from Fourier optics allows for lens-like focusing abilities. Figure 5.5 shows the 3D spot size (3-dB level) simulated for the retina array placed in the XY-plane at $Z = 0$ for a point source target placed at $Z = 100$ mm. The height of this spot is called the depth of field, which is the range at which the target appears within 3-dB value and is considered to be an indication of range resolution. The diameter of this spot in the XY plane at the focus distance (location of target), is an indication of cross-range resolution. The 3D spot size will depend on the distance of the target to the array.

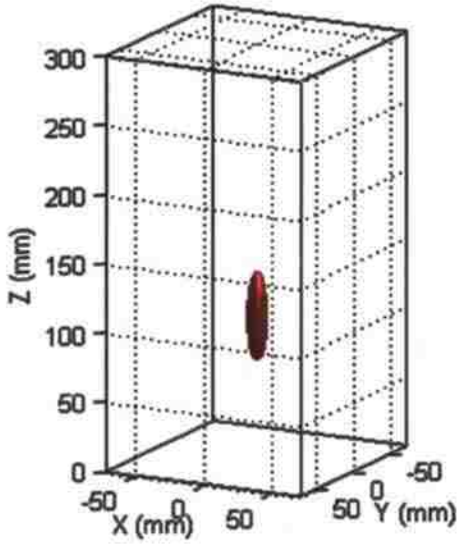

Figure 5.5. Simulated focused 3D spot size using the synthetic aperture focusing technique for the retina array.

Figure 5.6 shows the simulated depth of field and the spot size diameter for a point target in the array's broadside direction as a function of target distance to the array. The depth of field starts at approximately 12 mm for distances very close to the array, and exponentially increased with distance as shown in Figure 5.6(a). This is expected since the array operates at a single frequency and has no far-field range resolution. The depth of field in the array far-field will be infinity since a single frequency operation does not allow for any range resolution. The cross-range resolution starts at $\lambda/2$ [32], and then linearly increases with the focus distance (range). In the far-field of the array, this spot size will correspond to the angular beamwidth of the array. Overall, the SAF technique allows for limited 3D focusing capability, even at a single frequency operation. However, this capability is limited by the number of the scatterers and their scattering cross section. Strong scatterers near the array will not be easily defocused and will mask weak scatterers at larger distances. Utilizing larger frequency bandwidth allows for higher range resolution irrespective of the range.

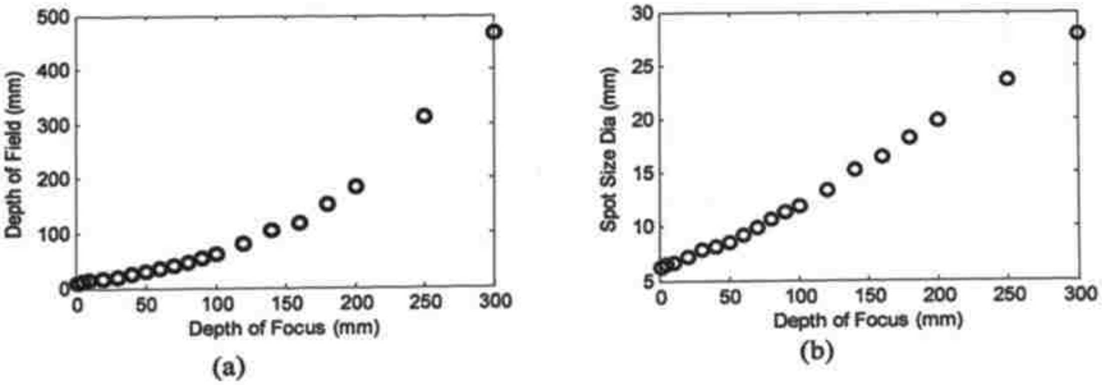

(a)

(b)

Figure 5.6. Simulated (a) depth of field, and (b) spot size; using the synthetic aperture focusing technique for the retina array.

The experiment shown in Figure 5.7 demonstrates the ability of this imaging system in localizing scatterers in a 3D space. Two metallic balls where hung in front of the retina using thin nylon strings. A 4 mm-diameter ball was placed at a distance of 150 mm away from the retina, and a larger 12 mm-diameter ball was placed at a distance of 260 mm from the retina. A small horn antenna was used to illuminate the scene from the side of the retina.

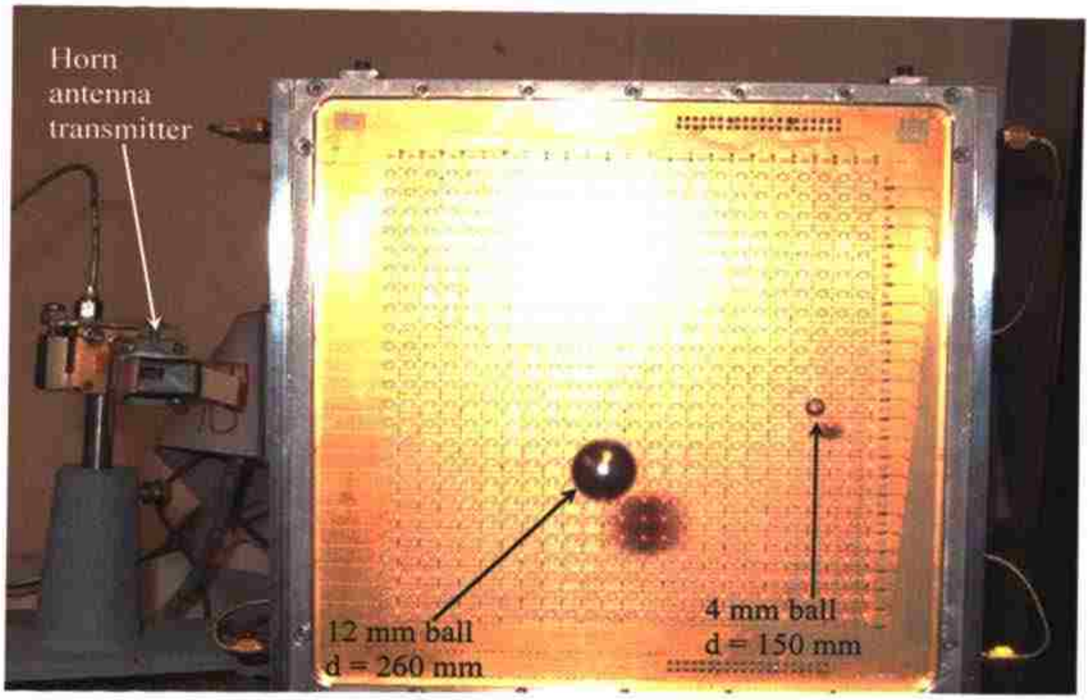

Figure 5.7. Picture of the setup for target localization experiment.

Screen shots of the camera output are shown in Figure 5.8. This screen shot shows the raw magnitude and phase and a SAF image of the scene obtained in real-time. Figure 5.8(a) is the screen shot where the SAF image is focused at the distance of 150 mm corresponding to the location of the small ball. It is apparent that the small ball is in focus and the larger ball is blurred. On the other hand, if the SAF image is focused at 260 mm for the same raw data as shown in Figure 5.8(b), the large ball comes in focus and the smaller one is blurred. These two images also show the capability of the camera to localize the target in the 2D space relative to the retina spatial domain.

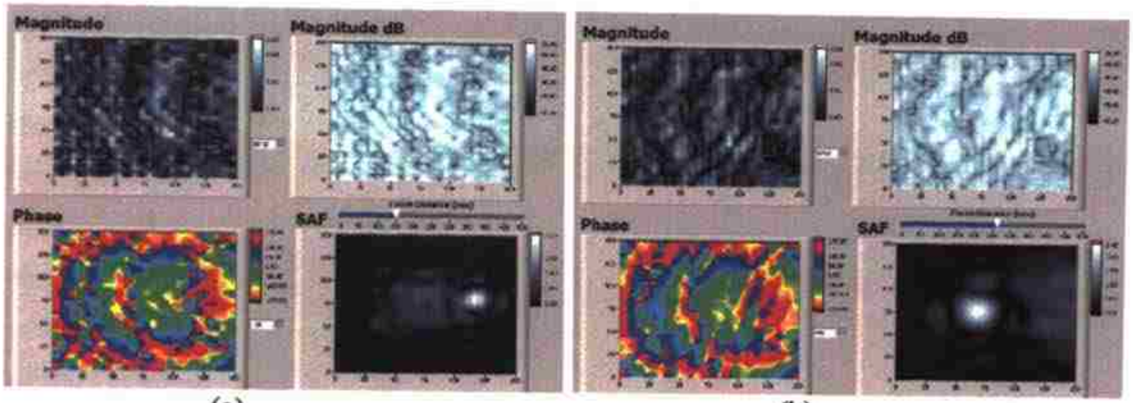

(a) (b)

Figure 5.8. Screen shot of camera output, (a) SAF at 150 mm, and (b) SAF at 260 mm.

5.3. IMAGING

As it was demonstrated above, the camera has the capability to measure electric field with the accuracy that allows for back propagation techniques such as SAF to be implemented and reconstruct the scattering source. Using this process it is possible to create images of targets that interact with the electric field in many applications. One such application is in nondestructive testing where the image of an object under examination, in particular its inner structure, is of interest. Imaging may be performed in through transmission mode, where the microwave signal is passed through the object and recorded on the other side. Imaging may also be performed in the more desirable reflection mode, where the transmitter and receiver are on the same side of the object being imaged. The reflection mode is more desirable for nondestructive testing applications. As explained earlier, the current state of the camera does not readily allows only for one-sided measurement. This section gives examples of using the camera for this type of imaging applications, mainly in transmission mode. Furthermore, utilizing simple transmitters on the camera sides for reflection mode imaging is also demonstrated.

5.3.1. Through-Transmission Mode. In through transmission mode, the camera is placed in front of a transmitting antenna and the object is placed in between the transmitter receiver. Usually a small transmitter antenna is used to create a fairly broad pattern, such that the object and the retina will be somewhat uniformly illuminated. A reference shot without the target is needed to correct for the variation in the pattern of the transmitter antenna [37]. Figure 5.9 shows the camera operation in the through transmission mode. In this case, the transmitter is a K-band open-ended rectangular waveguide antenna, and the target is a two-layer balsa wood composite with a small rubber inclusion. The images on the PC monitor show the raw magnitude, the raw phase and the SAF images obtained in real-time. In this configuration, the target either attenuates, or re-scatters the microwave energy towards the retina, and for this reason the rubber inclusion and the edges of the sample are clearly seen in the focused image while the majority of the balsa wood is seen transparent to microwave energy.

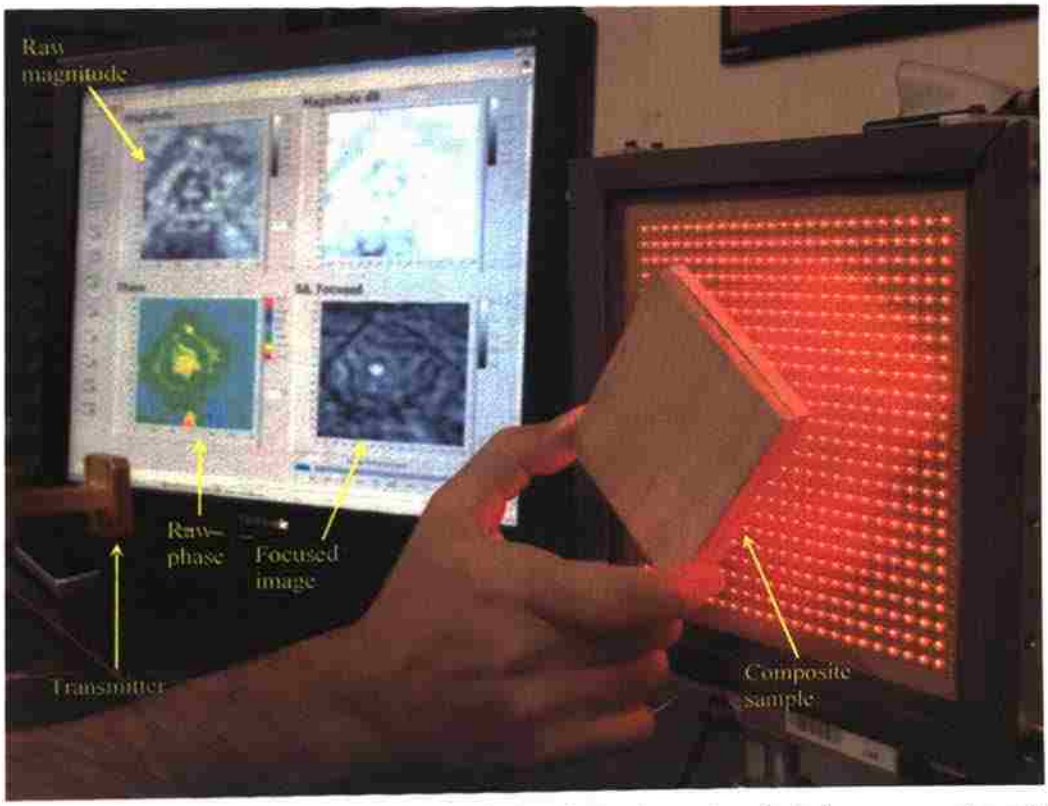

Figure 5.9. Real-time imaging in transmission through mode of a balsa composite with a small rubber inclusion.

5.3.2. External Illuminator Reflection Mode. Using the current camera, reflection mode is only possible utilizing an external transmitter to illuminate the target. However, the pattern of this external illuminator will play a role in the image of the scattering target. Figure 5.10(a) shows the phase pattern of scattered field off a long metallic rod with a diameter of 8 mm recorded at the retina aperture. The experimental setup is similar to that shown in Figure 5.7. The phase pattern shows elongated concentric circles instead of vertical strips expected of a long rod. This phase map is due to the effect of the transmitter pattern on the field scattering from the long rod. Applying SAF to obtain the image of the rod produces a rod indication which varies in intensity inline with the pattern of the transmitting antenna which is more concentrated in the middle as shown in Figure 5.10(b). For simple structures such as rod, it is possible to correct for the pattern effect, as long as there is sufficient power incident on the entire rod

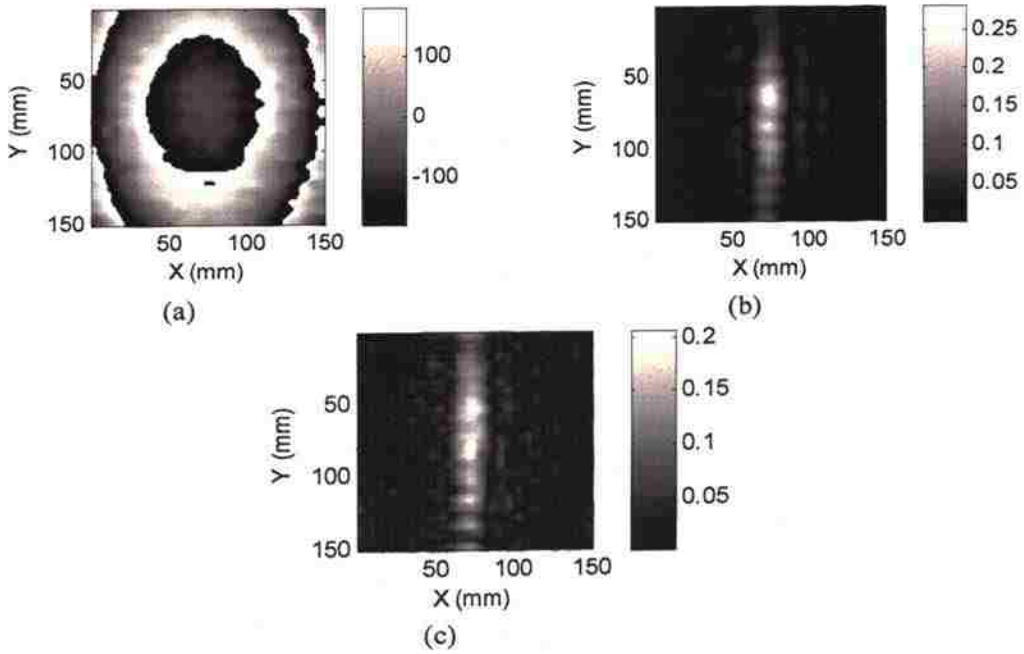

(a)

(b)

(c)

Figure 5.10. Reflection mode imaging of long 8 mm-diameter rod; (a) phase map of the scattered field at the retina aperture when the illuminator is in the middle, (b) SAF image when the illuminator is in the middle, and (c) combined SAF images of three separate illumination images.

(i.e. no nulls in the transmitter pattern). On the other hand, for complex structures the correction will be difficult due to the effect of the target on the pattern of the transmitter. Another solution is to illuminate the target from different angles and then combine the focused images. Figure 5.10(c) shows an image of the same rod obtained by illuminating the rod from middle left side, top left corner, and bottom left corner of the retina. The three focused images were averaged - as a first order approximation, to produce a complete image of the rod. It is not possible to combine the raw phase and magnitude data, or to have multiple transmitters working at the same time, since that will produce peaks and nulls which will degrade the image. Increasing the number of the transmitters will allow for illuminating the targets from various angles. Subsequently, switching between them and then properly combining the images may results in better images if the retina is intended to be used in reflection mode.

In another experiment a 4″ × 2″ × 0.5″ balsa wood sample with a thin 0.25″ × 0.25″ copper tape inclusion was imaged in reflection mode, as shown in Figure 5.11. The

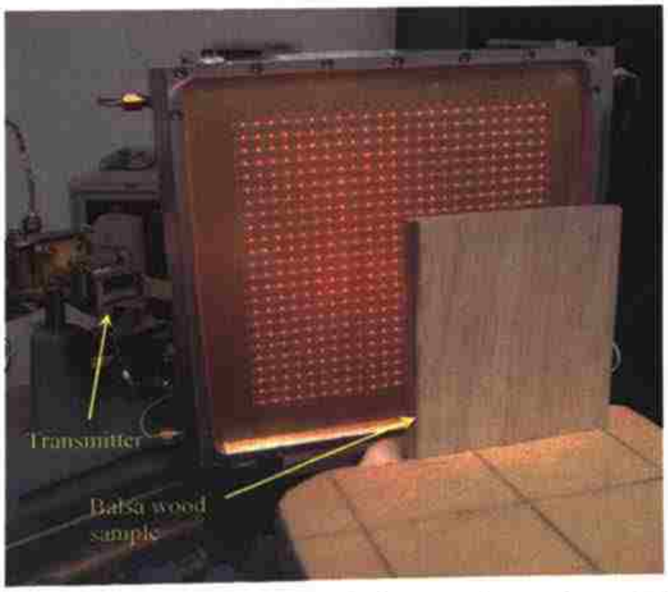

Figure 5.11. Experimental setup for NDI of a balsa wood sample containing a thin copper tape inclusion in reflection mode.

sample was placed at 150 mm distance from the retina. Figure 5.12(a) shows the SAF image when the sample was placed vertically in front of the retina. An indication of the copper inclusion can be seen in the middle of the image. The dashed line indicates the boundary of the sample. The image also shows a strong specular reflection from the left edge which is closer to the transmitter. Placing the sample horizontally and tilting it slightly towards the illuminator reduces the effect of this specular reflection as can be seen in Figure 5.12(b).

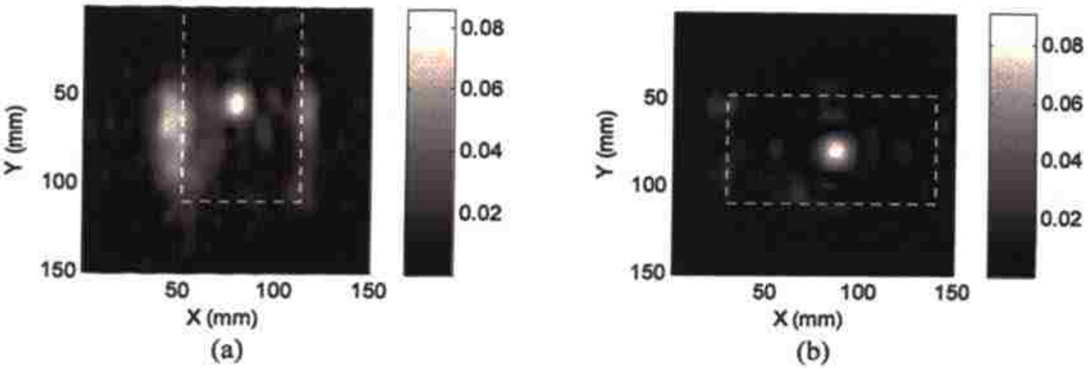

(a) (b)

Figure 5.12. SAF images of the balsa wood sample with copper inclusion in reflection mode; (a) sample is vertical, and (b) sample is horizontal.

As it was shown in these two reflection mode experiments, the choice of transmitting antenna and the illuminator pattern on the target affects the fidelity of the obtained image. Non-uniform illuminations and specular reflections may cause some areas of the target not to be illuminated properly. When image reconstruction techniques such as SAF is used, the ultimate solution is to have as many transmitters as the number of receivers, which in the limit converges to the array elements being used in mono-static mode whereas each element is used as a transmitter and receiver. Mono-static mode produce high quality images since the target is illuminated from various angles which greatly reduced distortions due to specular reflections [5].

5.4. APERTURE REPETITION

An important property of using arrays for imaging is that, the signal strength and the resolution is proportional to the array gain and beamwidth, which in terms is proportional to the array size. Building very large arrays may not be practical or cost effective. However, when a handheld and fast array, such as this camera is available, one can take snapshot images of various side-by-side locations, and then synthetically combine the images to produce larger, high resolution, and high fidelity images. Figure 5.13 shows the results of such experiment, whereas the scattering off an 8 mm-diameter metallic ball is measured at a distance of 170 mm. The measurements were performed by using the camera to take a snapshot of the scattered field. Then four measurements were taken on adjacent areas around the axis of the ball to synthesize a larger aperture. Only the phase of the scattered field is shown, since at these distances, the magnitude does not show any substantial variations. However, when SAF was applied, both the magnitude and phase of the measurements were used. As shown in Figure 5.13, a larger aperture provides for a better focused image, and a stronger indication of the target. Intuitively, a larger array (synthetic in this case) provide for higher gain and smaller beam width as explained earlier. Furthermore, from image reconstruction point of view, this experiment shows that capturing more of the scattered field (i.e., using larger aperture) will result in a better indication of the target.

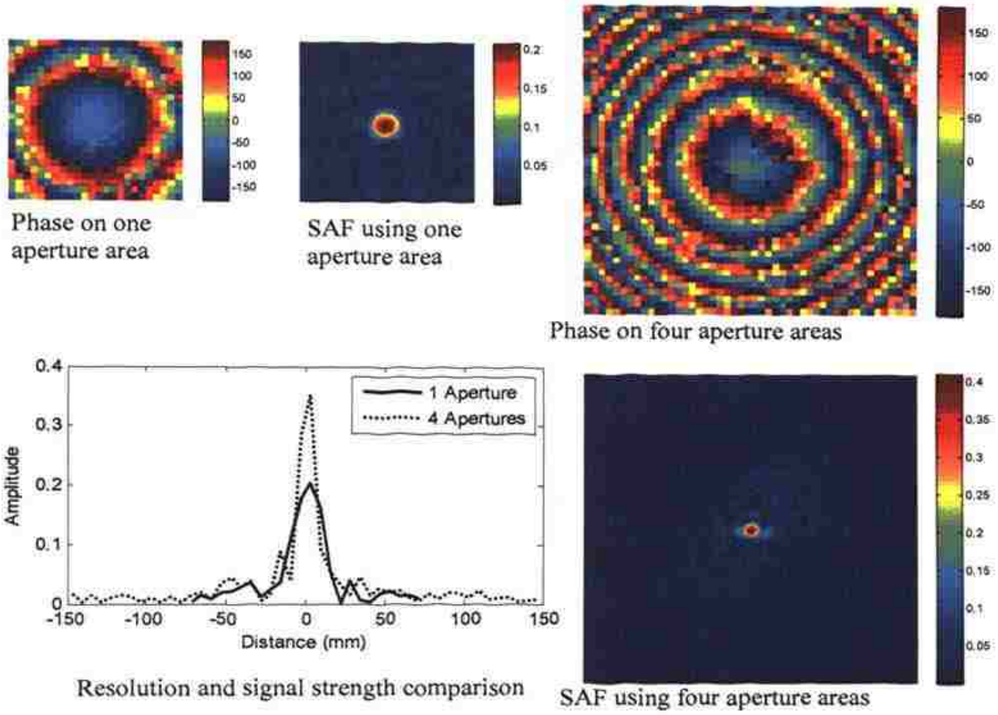

Phase on one aperture area

SAF using one aperture area

Phase on four aperture areas

Resolution and signal strength comparison

SAF using four aperture areas

Figure 5.13. Effect of synthetically increasing the aperture area of the retina.

[40] R. Justice, V. Rumsey, "Measurement of electric field distributions," *IRE Trans. on Antennas and Propagation*, vol.3, no.4, pp.177-180, October 1955.

[41] M-K. Hu, "On Measurement of Microwave E and H Field Distributions by Using Modulated Scattering Methods," *IRE Trans. on Microwave Theory and Techniques*, vol.8, no.3, pp.295-300, May 1960.

[42] J.C. Bolomey, B.J. Cown, G. Fine, L. Jofre, M. Mostafavi, D. Picard, J.P. Estrada, P.G. Friederich, F.L. Cain, "Rapid near-field antenna testing via arrays of modulated scattering probes," *IEEE Trans. on Antennas and Propagation*, vol.36, no.6, pp.804-814, Jun 1988.

[43] M. A. Abou-Khousa, S. Kharkovsky, and R. Zoughi, "On the mutual coupling between circular resonant slots", *Proc. 3nd Intern. Conf. on Electromagnetic Near-Field Characterization & Imaging (ICONIC 2007)*, St. Louis, USA, , pp. 117 – 122, 2007,

[44] CST-Computer Simulation Technology, http://www.cst.com.

[45] Rogers Corp., *RO4000 Laminates Datasheet*, Available: http://www.rogerscorp.com/documents/726/acm/RO4000-Laminates-data-sheet-and-fabrication-guidelines-RO4003C-RO4350B.aspx

[46] Tyco Electronics, M/A-COM Wireless Components; Available: http://www.macom.com/DataSheets/MA4AGP907_FCP910.pdf.

[47] M.A. Abou-Khousa, M.T. Ghasr, S. Kharkovsky, D.L. Simms, R. Zoughi and D. Pommerenke, "K-band Microwave Imaging System," *Final Report, NASA Marshall Space Flight Center (MSFC), Huntsville, AL*, p. 42, March 2008.

[48] D. M. Pozar, *Microwave Engineering*, 2nd Ed, Wiley, NY, 1998.

[49] V.S. Mottonen, "Wideband coplanar waveguide-to-rectangular waveguide transition using fin-line taper," *IEEE Microwave and Wireless Components Letters*, vol.15, no.2, pp. 119-121, Feb. 2005.

[50] J.G.M. Yip, A.K. Jastrzebski, R.J. Collier, L. Daiqing, "The design of waveguide-to-finline taper transitions at millimetre wave frequencies," *14th International Conference on Microwaves, Radar and Wireless Communications, MIKON-2002*, vol.1, no., pp. 282-285 vol.1, 2002.

[51] J-H. Choi, J-I. Moon, S-O. Park, "Measurement of the modulated scattering microwave fields using dual-phase lock-in amplifier," *IEEE Antennas and Wireless Propagation Letters*, vol.3, no., pp. 340-343, 2004.

[52] Analog Devices, App. Note, *Ask the Application Engineer -30: PLL Synthesizers*, Available: http://www.analog.com/static/imported-files/application_notes/494973545190600605APP_NOTE_FOX.pdf

[53] Hittite Corp., App. Note, *Layout Guidelines for MMIC Components*, Available: http://www.hittite.com/content/documents/layout_guidelines_for_mmic_components.pdf

[54] D. Antsos, R. Crist, L. Sukamto, "A novel Wilkinson power divider with predictable performance at K and Ka-band," *IEEE MTT-S International Microwave Symposium Digest*, , vol., no., pp.907-910 vol.2, 23-27 May 1994.

[55] Stanford Research Systems, *CG635 Data Sheet*, Available : http://www.thinksrs.com/downloads/PDFs/Catalog/CG635c.pdf

[56] The MathWorks, Signal Processing Toolbox, Available: http://www.mathworks.com/access/helpdesk/help/toolbox/signal/signal_product_page.html

[57] M. L. Skolnik, *Introduction to RADAR Systems*, 3rd Ed, McGraw Hill, NY, 2001.

[58] H.T. Friis, "Noise Figures of Radio Receivers," *Proceedings of the IRE*, vol.32, no.7, pp. 419-422, July 1944.

[59] J. D. Kraus, *Antennas*, 2nd Ed., McGraw Hill, NY, 1988.

[60] C. A. Balanis, *Advanced Engineering Electromagnetics*, New York: Wiley, 1989.